PHYSICS-BASED COMPACT MODELING OF ORGANIC ELECTRONIC DEVICES

Chang Hyun Kim

THÈSE

présentée pour obtenir le grade de

DOCTEUR DE l'ÉCOLE POLYTECHNIQUE

Spécialité : Physique

par

Chang Hyun Kim

APPROCHE PHYSIQUE DE LA MODÉLISATION COMPACTE POUR LES COMPOSANTS ÉLECTRONIQUES ORGANIQUES

Soutenue le 1er juillet 2013 devant le jury composé de :

Bertram Batlogg	ETH Zurich	Rapporteur
George Malliaras	Ecole Nationale Supérieure des Mines de Saint-Etienne	Rapporteur
Benjamin Iñiguez	Universitat Rovira i Virgili	Examinateur
Raphaël Clerc	Institut d'Optique	Examinateur
Lionel Hirsch	Université de Bordeaux/CNRS	Président du jury/ Examinateur
Yvan Bonnassieux	Ecole Polytechnique	Examinateur
Gilles Horowitz	Ecole Polytechnique/CNRS	Directeur de thèse

PHYSICS-BASED COMPACT MODELING OF ORGANIC ELECTRONIC DEVICES

Chang Hyun Kim

chang-hyun.kim@polytechnique.edu

Thesis advisor: Prof. Gilles Horowitz

A thesis for the degree of

Ph.D. in Physics

2013

Acknowledgements

Abstract

Despite impressive progresses in organic electronic devices, a full theoretical understanding of the device operation is still lacking. The thesis is dedicated to establishing applicable theoretical descriptions of organic electronic devices, and in particular physics-based compact models. Prototypical organic diodes and transistors with various architectures are investigated, with a consistent effort to view and present the effect of charge carrier transport and injection on the observable device phenomena. A particular effort is given to integrate these models in circuit simulators, thus connecting the device-level and system-level outlooks. The approaches used comprise equivalent circuit modeling by impedance spectroscopy, analytical development of physics equations, numerical finite-element-based 2-D simulations, and experimental validations. The results provide significant understanding on the effect of traps and injection barriers on the current-voltage characteristics. Original, fully analytical compact models for rectification diodes and organic field-effect transistors are proposed with reliable numerical and experimental proofs.

Keywords
Organic electronics, device physics, analytical modeling, diodes, field-effect transistors

Contents

Chapter 1

Introduction

1.1 Organic electronics

Organic electronics is a new technological field that makes use of the optoelectronic properties of organic semiconductors. Organic materials are carbon-containing materials, often classified into small-molecules or polymers according to the size of the basic chemical unit [1]. Such as a plastic drink bottle (a type of synthetic polymer), most general organic materials are believed not to pass an electrical current thorough them. However, the discovery of 'conducting polymers' in 1977 [2] defined a new class of materials, which is now called 'organic semiconductors', drawing significant attention of scientific communities to their properties and applications. This pioneering research was on the observation of increased electrical conductivity of halogen-doped polyacetylene, and for this work, Heeger, MacDiarmid, and Shirakawa were awarded the 2000 Nobel Prize in Chemistry. Growing research efforts led to the early demonstrations of application-oriented electronic devices using organic semiconductors. In 1986, Tang reported two-layer organic photovoltaic cells (OPVs) using copper phthalocyanine (CuPc) and a perylene tetracarboxylic derivative as organic semiconductors [3]. In the same year, an organic field-effect transistor (OFET) using polythiophene was first reported by Tsumura, Koezuka, and Ando [4]. In 1987, Tang and VanSlyke published on organic light-emitting diodes (OLEDs) using Alq_3/diamine junction [5]. These reports are considered as a milestone that ignited excitement about the electronic application of organic semiconductors, which lasts until present over two decades.

What makes organics so special is their molecular nature. At variance with inorganic crystals in which all consisting atoms are strongly bound by covalent bonds, organic molecules are 'weakly' linked to each other by van der Waals force [1]. It is this weak intermolecular interaction that gives mechanical flexibility to organic films
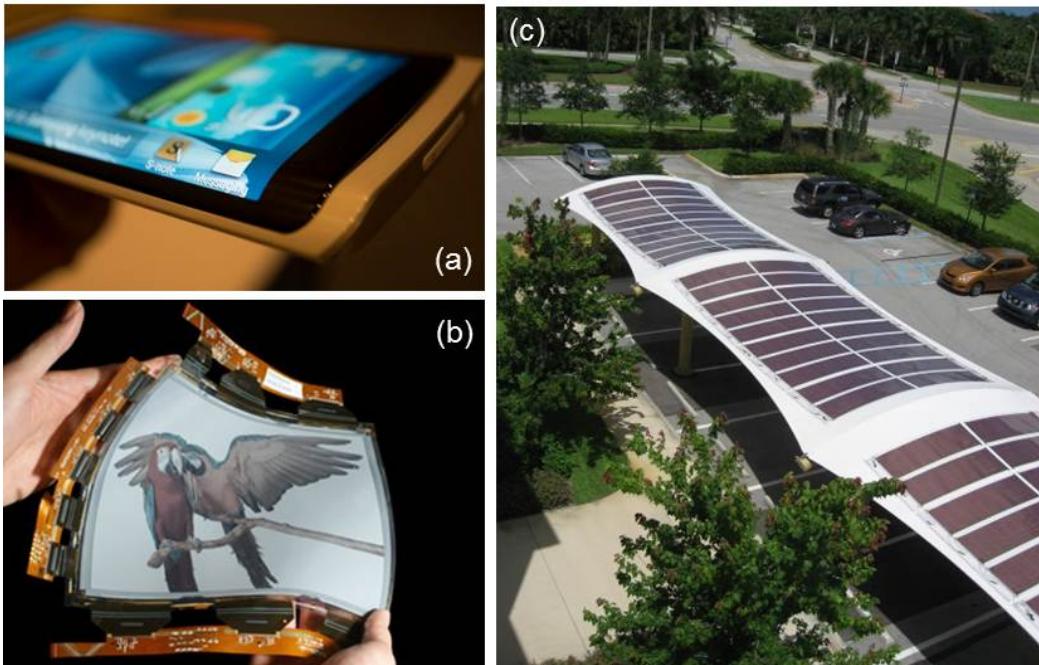
Figure 1.1: State of the art: (a) Bendable OLED mobile display, (b) ultra-flexible, lightweight E-paper color display with an OFET backplane, (c) OPV modules providing both power and natural cooling to a carport in Florida.

or crystals. Although a molecule itself consists of covalently (tightly) bound atoms, weak molecule-molecule bonds can be easily broken or reformed. Thus, molecules can be dispersed in solvents or evaporated at moderate temperature, allowing for various new process concepts for organic semiconductors. The possibility of making organic semiconducting inks enables deposition of functional layers only at desired positions on the substrate by ink-jet printing, thus eventually minimizing fabrication cost of large-area electronic circuits compared to the conventional vacuum-based deposition and lithographical patternings. The ultimate goal of organic electronics is therefore based on the fundamental properties of organic semiconductors. It is realization of 'flexible' and 'low-cost' electronic systems.

We have seen impressive progress in organic electronics over recent years. OLEDs are standing at the leading position in the market with diverse products available. OLED's display application showed particularly significant success. Owing to their inherently superior color expressiveness, moving-picture response, and low power-consumption, OLEDs are replacing conventional liquid-crystal displays (LCDs) especially in mobile devices. Figure 1.1(a) shows a picture of a bended OLED display mounted on the prototype mobile phone presented by Samsung Electronics at the International Consumer Electronics Show (CES) 2013 [6]. Another key application

of OLEDs in the future might be solid-state lighting by white OLEDs [7,8]. OFETs can be used as active-matrix pixel drivers in LCDs or OLEDs and OFET-based display backplanes are under consistent development [9,10]. Plastic Logic's ultra-flexible paper-like display in Figure 1.1(b) has a backplane circuitry composed of OFET arrays [11]. OFET-based large-area sensors for optical and mechanical read-out are also significant for advanced applications such as conformable image scanners, electronic skins [12–15]. OPVs for solar-to-electrical energy conversion have particularly important economic emphasis due to other competing technologies for alternative, sustainable energy [16]. Konarka has demonstrated various architecture-integrated OPVs by virtue of excellent flexibility and scalability of their plastic solar cell products [Figure 1.1(c)] [17].

In addition, novel applications are being suggested. Organic electronics' multidisciplinary character has continuously encouraged physicists, chemists, and engineers to explore a wide variety of new materials and device functionalities, which led to various new concepts of organic devices. Among others, biomedical application is regarded as one of the most attractive orientations that organic electronics community can proceed toward [18,19]. Today, organic electronics is at a crossroad of development. Researchers have overcome many serious challenges encountered at its infancy, such as performance and stability issues. However, the industrial acceptance seems still limited probably due to other emerging technologies or lack of killer application that takes the unique advantages of organic semiconductors. We expect to see further breakthroughs that will lead organic electronics to a more competitive position, which will fully realize the 'soft' potential that attractive organic semiconducting materials bear.

1.2 Motivation

First motivation of the thesis is the lack of theoretical understanding on organic semiconductors and devices. In spite of impressive progress in terms of device performance and stability, current knowledge on many fundamental phenomena is still incomplete. In a historical point of view, this problem might be due to the urgent need to prove that organic devices can compete with existing Si-based technologies. Tremendous research efforts have thus mainly been put into the experimental works, which could finally meet such requirements. However, many theoretical questions remain unsolved. To answer these questions, there has been a natural tendency to adopt classical semiconductor and device models, which were originally developed for

inorganic semiconductors. Because there is a fundamental difference in organics from inorganics, this choice cannot always be justified. The difference here comprises both the material aspect and the geometrical aspect (device architecture), many of which will be detailed in this thesis. The virtually unlimited range of chemical structures for organic semiconductors make establishing a universal model extremely difficult. Nonetheless, specific device models that distinguish the organic from inorganic ones are highly desirable because they will allow people to more deeply understand the behavior of organic devices. This understanding in turn can provide the ability to interpret the experimental results and even predict them based on proper physical insights. Such process can form a positive feedback for experimental design and fabrication.

Second motivation is the growing interest of the community in 'device-to-system integration'. Even though most academic groups still focus on the device level investigation (isolated diodes or transistors), recent reports on higher level systems such as displays, PV modules, RFID systems and matrix-based sensors show great potential of organic electronics for industrial applications. In this context, device models play a particularly important role. In circuit simulators such as SPICE, a device is in fact represented by an equation (or a set of equations), which is often called a compact model [20]. We can use a compact model to fit the measured current-voltage characteristics and extract the relevant parameters. Then, we can build more complex circuits in a simulator to see expected characteristics of those circuits before fabricating a real one. In other words, a compact model provides a bridge between the device-level and the circuit-level outlooks. Therefore, specific compact models based on the unique features of organic materials and devices are essential for reliable simulation of organic-based circuits and systems.

1.3   Thesis overview

This thesis is titled 'physics-based compact modeling of organic electronics devices'. Mathematical device modeling is developing a numerical or analytical model that mimics essential electrical characteristics. As the title implies, our foremost aim has been on development of specific models for organic devices that feature both theoretical backgrounds and practical applicability. These two aspects are based on the two major motivations described above. With this purpose, we have studied a wide range of device geometries by multiple theoretical and experimental methods. Here, a brief description of each chapter is given for overview.

In **Chapter 1 Introduction**, a brief introduction to organic electronics was given with the important motivations for the thesis and related aim and scope of the thesis.

Chapter 2 Fundamentals provides short summaries on the most basic physical backgrounds for understanding organic semiconductors and organic electronic devices. The origin of the semiconducting properties in organic materials is briefly described. Charge transport physics of organic semiconductors relies on the solid-state crystallinity and corresponding energetic structure. Different transport mechanisms are summarized for different classes of material. Charge carrier injection at a metal/organic interface is a basic ingredient for understanding contact behaviors of devices. Interface properties and barrier formation are described in this chapter.

We explain in **Chapter 3 Methods** main techniques or methods that have been applied to model various devices. Four main methods used in the thesis are impedance spectroscopy, analytical modeling, numerical simulation, and experimental investigation. As will be seen in the result chapters, all these methods have been complementarily used. An introduction and practical knowledge for each method is given here to help understand the results obtained by using each method.

Chapter 4 Modeling organic diodes is the first main chapter dedicated to the scientific results. Three different categories of organic diodes have been studied; vertical rectifying diodes, vertical symmetrical diodes, and gap-type diodes. For rectifying diodes, the concept of full depletion in unintentionally doped organic semiconductors, and following analytical development of electrostatic distribution and current-voltage characteristics are elaborated. Vertical symmetrical diodes are modeled by impedance spectroscopy. The time-dependent evolution of the equivalent circuit shows persistent photoexcitation effect on a polymeric film. For gap-type diodes, we revisited the space-charge-limited conduction in a two-dimensional geometry and suggest a compact model that links two different physical regimes by a single equation.

Chapter 5 Modeling organic transistors is the second chapter on the scientific results. Organic metal-semiconductor field-effect transistors (OMESFETs) and OFETs are analyzed. Experimental results on pentacene-based OMESFETs are presented with the simulation results for understanding their operation mechanism. For OFETs, we deal with the physical difference of the contact geometries and present an original model for the charge distribution and contact resistance in coplanar transistors. Finally, compact modeling approach for circuit simulation with improved output asymptotic behaviors is proposed.

In **Chapter 6 Conclusion and outlook**, major results that are found and analyzed in the thesis are summarized with concluding remarks. Limitation encountered

during the research and related suggestions for the future work will be also specified.

Chapter 2

Fundamentals

In this chapter, fundamental physics of organic semiconductors and charge transport and injection phenomena is summarized. We mainly focus on addressing distinct features of organic materials and devices compared to the inorganic counterparts. On that account, basic knowledge on solid-state physics and semiconductor device physics, which can be found in typical textbooks [21–23], is not detailed here. We first discuss the semiconducting properties of organic materials with generally accepted classification of the typical semiconductors. Then, the charge carrier transport is elaborated with an emphasis of the characteristic density of states (DOS) of organic materials and corresponding mobility behaviors. Finally, energetic alignment and formation of the carrier injection barrier upon forming a metal/semiconductor junction is described.

2.1 Organic semiconductors

2.1.1 π-conjugated molecules

Organic materials are characterized by various forms of hydrocarbon (C-H) units within the chemical structure of molecules [1]. Organic semiconductors can be defined as the organic materials that exhibit semiconducting properties, thus corresponding to a subset of a vast variety of organic materials. Therefore, it is important to understand in which condition an organic material can behave as a semiconductor.

Carbon is a group four material in the periodic table, so it contains four valence electrons. A special property of carbon is the ability to hybridize its atomic orbitals in a number of ways, which leads to a wide variety of bonding configurations [24]. More specifically, the four outermost atomic orbitals of a carbon atom are hybridized differently depending on the number of atoms with which the valence electrons are
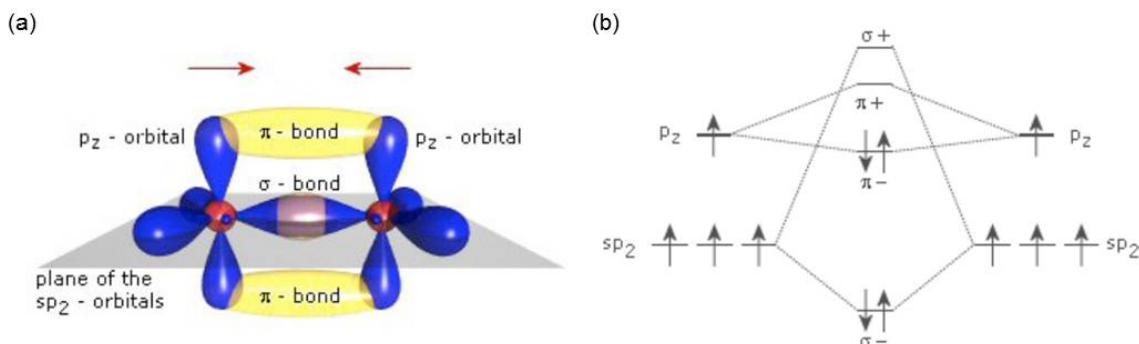
Figure 2.1: (a) Orbital and chemical bonding in an ethylene (C_2H_2) molecule. (b) Energy diagram of the carbon-carbon bonding by the sp_2 hybridization.

shared. When the valence electrons are shared with four neighboring atoms, four sp_3 hybrid orbitals of equal energy are created by the superposition of one $2s$ and three $2p$ orbitals. On the contrary, with only three atoms for which a carbon atom makes covalent bonds, three sp_2 hybrid orbitals are formed with one remaining p orbital.

The sp_2 hybridization and the formation of carbon-carbon double bonds are exemplified by ethylene (C_2H_2), the simplest alkene molecule. As illustrated in Figure 2.1(a), three electrons of a carbon atom in the sp_2 orbitals form three σ bonds with two hydrogen and one carbon atoms. Due to the large overlap between the orbitals, σ bonds are strong and difficult to be broken (high binding energy). In addition, for minimizing the repulsion force, three sp_2 orbitals are in a planar configuration, thus defining the molecular plane with triangular position. The remaining p_z orbitals point perpendicularly to the sp_2 plane, and the carbon atoms share their fourth electron, thus making a π bond. Even though a macroscopic representation of a 'double' bond does not imply any difference in two, the π bond has significantly lower binding energy than the σ bond because the distance between the two p_z orbitals is considerable, which means weak overlap or interaction between the orbitals. It is this weak π bond that accounts for the possible semiconducting property of organic molecules. The energy diagram in Figure 2.1(b) illustrates this aspect. Upon filling the molecular orbitals from the bottom, the highest occupied molecular orbital (HOMO) and the lowest unoccupied molecular orbital (LUMO) turn out to be the bonding π orbital and the antibonding π^* orbital, respectively. Due to the weak π binding energy, the HOMO-LUMO gap is relatively small. Therefore, in a global sense, organic materials that have frontier orbitals (HOMO and LUMO) formed by π-bonded electrons are considered as semiconductors due to the possibility of having a significant density of thermally-generated and/or photo-generated charge carriers.
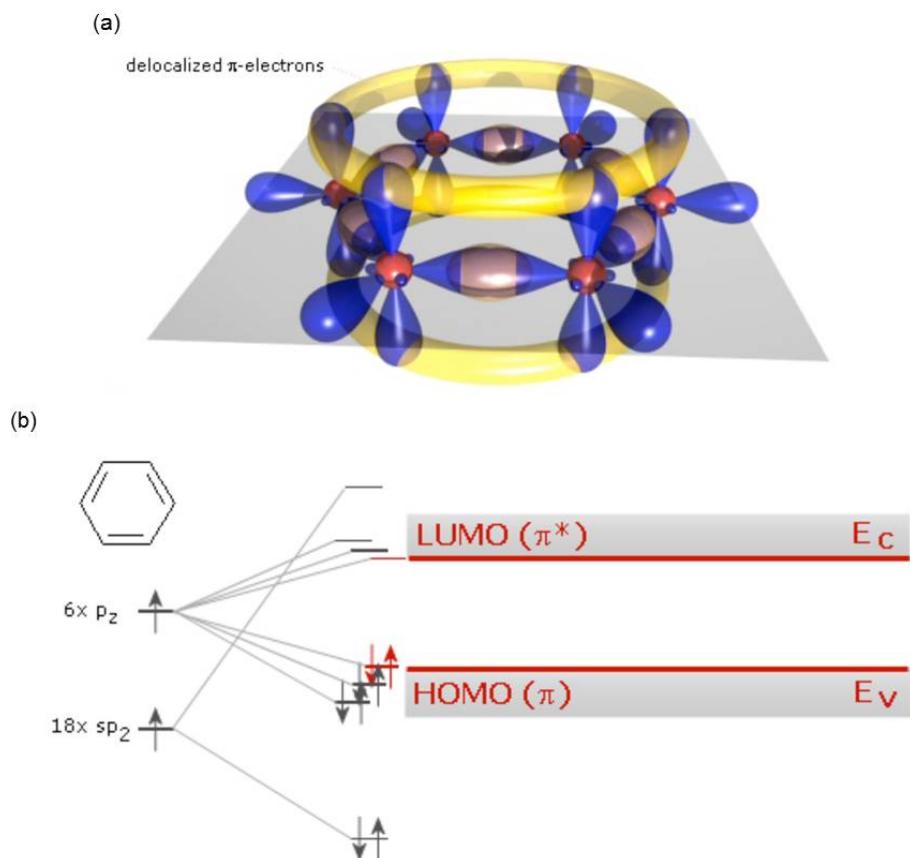
Figure 2.2: (a) Orbitals of a benzene (C_6H_6) molecule. (b) Chemical structure and energy diagram of benzene.

This foremost argument is extended to larger molecules. Figure 2.2(a) illustrates the orbital picture of benzene (C_6H_6). Even though six carbon-carbon bonds are usually drawn as alternating single and double bonds in the conventional chemical structure, all the six bonds have the same length and are thus equivalent in geometrical and energetic aspects. It is due to the fact that all the six electrons coming from the six carbon p_z orbitals are so weakly bound to the neighboring atoms that they are virtually delocalized though the whole cyclic chain of the molecule. As the number of p_z orbitals giving rise to the π-π* molecular orbitals increases, the HOMO and LUMO orbitals are split into the close but different energy levels shown in Figure 2.2(b). This is analogous to the formation of energy bands of inorganic semiconductors when the number of atoms increases to make a crystal network. Thus, it can be said that the HOMO and LUMO 'levels' widen into the HOMO and LUMO 'bands', which are often interchangeably used with the valence band and the conduction band, respectively.

Delocalization of the electrons in the p (or π) orbitals implies the possibility of
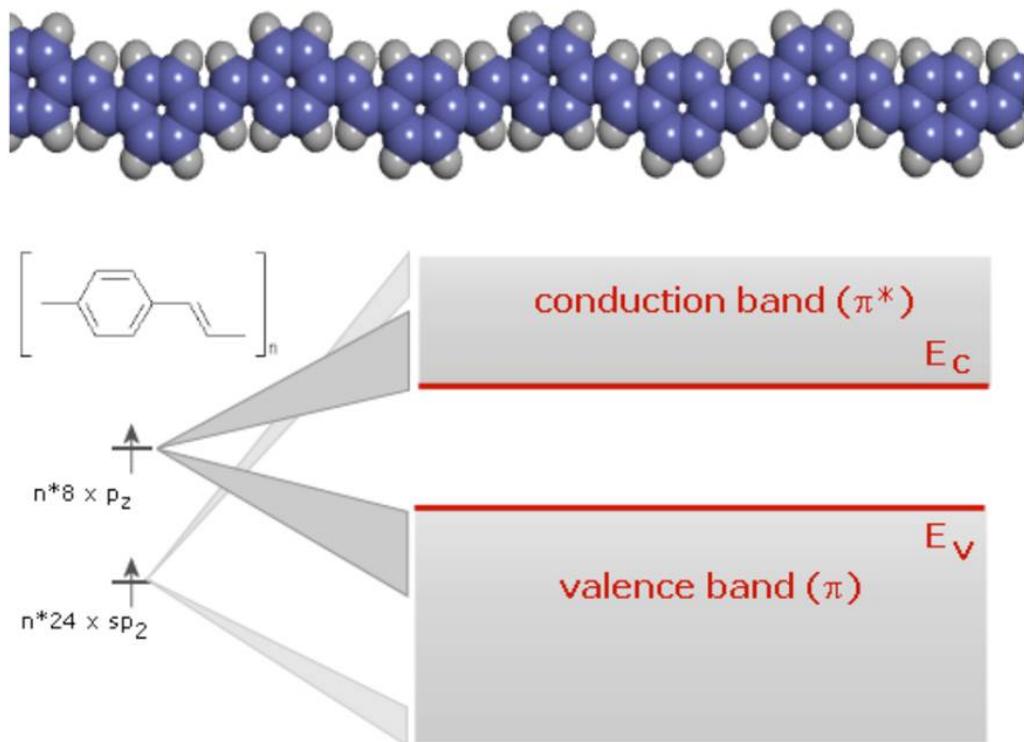
Figure 2.3: Chemical structure and energy diagram of poly-para-phenylene-vinylene (PPV).

movement of charge carriers inside a molecule, whereas the electrons forming σ bonds serve as a rigid frame that maintains the structure of the molecule. This type of chemical system where the π-electrons are delocalized through alternating single and double bonds is often called a π-conjugated system. Figure 2.3 shows a much larger example, the π-conjugated polymer poly-para-phenylene-vinylene (PPV). In general, as the conjugation length increases, the bandwidth increases and the bandgap decreases as a result of the splitting of the frontier molecular orbitals.

2.1.2 Organic molecular solids

It is now clear that π-conjugated units in the molecular structure allow for semiconducting properties at molecular level. In inorganic semiconductors, the covalent bonds between atoms are the only contribution to form a macroscopic crystal or solid. However, organic molecules are not covalently bound to each other but they only weakly interact via van der Waals force. Therefore, in organic solids, semiconducting properties at macroscopic level is only expected when the inter-molecular interaction is significant so that the π-conjugated electrons can have enough freedom

to be delocalized and moved from one molecule to another.

As mentioned in Section 1.1, the weakness of the interaction between molecules in solid state is the most distinctive feature of organic semiconductors, which brings both new opportunities and ultimate limitations to device applications. Mechanical softness and solution-process compatibility are the main advantages of weakly-bound molecules. Through simple evaporation or printing techniques, the process temperature of an electronic device can be significantly lowered, which allows for deposition of functional organic materials on a plastic or rubber-like substrate for flexible and even stretchable electronics [25–28]. On the other hand, due to the weak electronic coupling between molecules, there is a significant limitation to the charge-carrier transport, as discussed in more detail in Section 2.2.

In general, organic solids can exist either as free-standing and manipulatable single crystal pieces or as thin-films deposited and fixed on top of a substrate. Organic single crystals can be obtained from small-molecules by different types of controlled growth systems. Owing to the highest purity and molecular order, organic crystals show superior electrical characteristics and also allow access to the intrinsic and fundamental understanding on charge transport physics [29, 30]. On the other hand, organic thin-films deposited by evaporation or solution-based techniques benefit from better mechanical flexibility and processability, thus are more widely used for practical applications.

2.1.3 Material classification

Organic semiconductors are most often categorized as either small-molecules or polymers according to the size and molecular weight. Polymers consist of repeating units leading to generally very long chain structure, whereas small-molecules have a more compact and readily definable chemical structure. Figure 2.4 shows a few examples of organic semiconductors. It is seen that all of them contain various alternating single-double bond configurations accounting for the semiconducting properties by π-conjugation.

An additional way of classification is to consider the typical processability of a specific material. We can distinguish soluble and insoluble organic semiconductors. Semiconducting polymers have been preferably used for solution process such as spin coating and ink-jet printing due to good solubility in typical organic solvents [31–33]. On the other hand, it has been generally believed that vacuum-evaporation is more suitable for small-molecules. However, this statement is no longer strictly correct due to the recent development of high-performance soluble small-molecular

Polymers   **Small-molecules**

Poly-acetylene

Poly-phenylene

Poly-thiophene

Poly-phenylene-vinylene

Phtalocyanine (M=H or metal)

Oligo-thiophene (n=3 to 8)
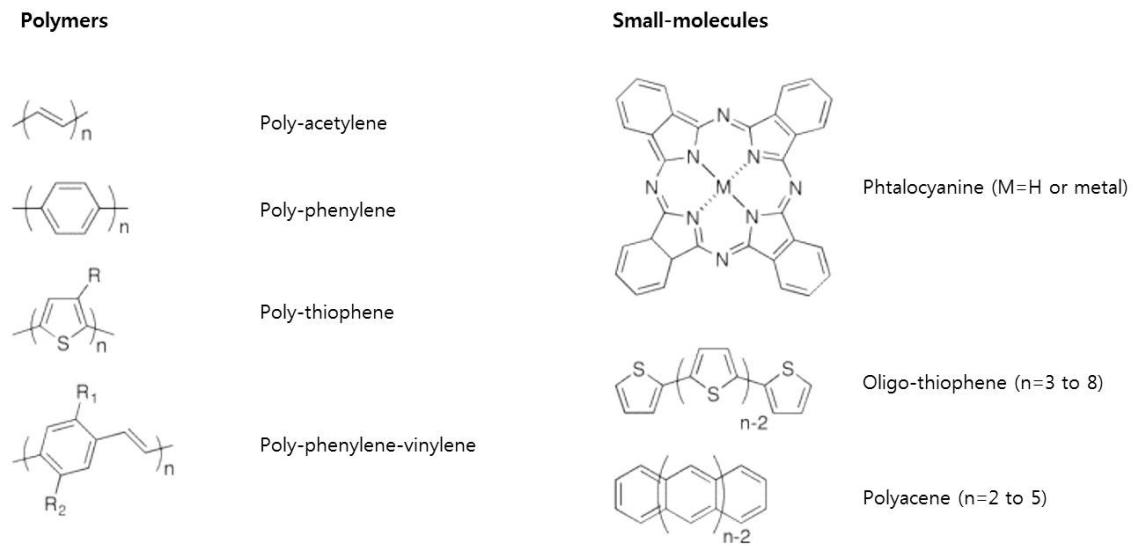
Polyacene (n=2 to 5)

Figure 2.4: Chemical structure of the typical class of π-conjugated organic semi-conductors. Oligo-thiophenes: terthiophene (n=3), quarterthiophene (n=4), quinquethiophene (n=5), sexithiophene (n=6), octithiophene (n=8). Polyacenes: naphthalene (n=2), anthracene (n=3), tetracene (n=4), pentacene (n=5).

semiconductors, realized by strategic synthesis of attaching substitution groups to enhance solubility [34–36].

There is also a tendency to specify an organic semiconductor as either p-type or n-type material, especially for transistor applications. We note that it may create confusion with the same denomination used for inorganic semiconductors. As inorganic semiconductors are generally used in a doped form, the appellation of p- or n-type is based on the type of doping impurities. P-type inorganic semiconductor are doped by acceptor impurities, and n-type by donors. However, organic semiconductors are used without an intentional doping step in most cases. The specification of p- or n-type is not determined by the type of dopant-induced charges, but rather by that of the 'injected' charges that govern the device current. Ideally, an organic semiconductor can be p-type when the contact electrode has a work function near its HOMO level, and the same material can also be n-type if the electrode work function better matches the LUMO level [37]. However, in reality, a given material tends to favor either hole or electron conduction, which is the reason that people can usually define a major carrier type for that material without consideration of the choice of electrode. Historically, p-type behaviors have been predominantly observed in early reports on OFETs. In 2005, Chua and co-workers revealed that the difficulty in observing n-type conduction is often related to the electron traps due to hydroxyl groups on the
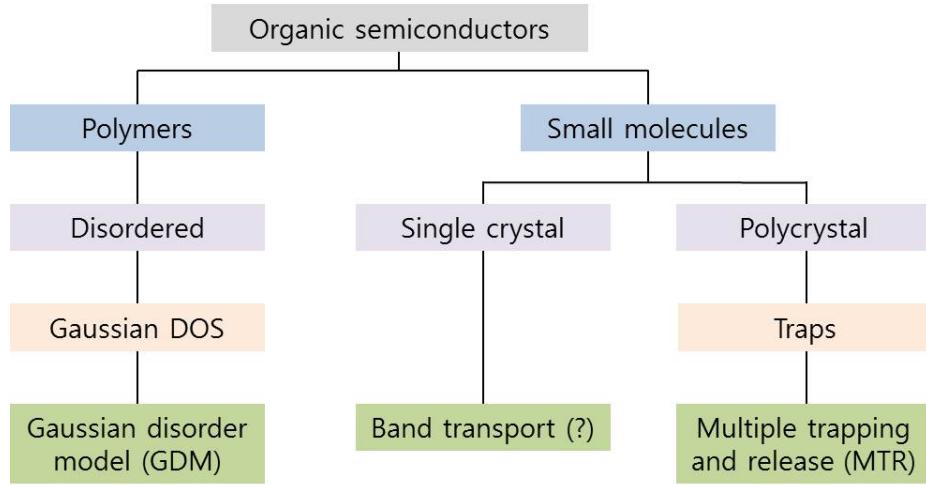
Figure 2.5: Categorization of the charge transport mechanisms of organic semiconductors according to the degree of disorder and the corresponding band structure.

insulator surface, and use of a hydroxyl-free dielectric can lead to general n-type behaviors in many polymeric semiconductors [38]. At present, there is a vast interest in the synthesis of new electron-transporting (or n-type) organic semiconductors and realization of high performance n-type transistors for complementary metal-oxide-semiconductor (CMOS) circuitry, where both p-type and n-type transistors have to be integrated [37, 39–41].

2.2   Charge-carrier transport

Complexity and inefficiency of charge transport in organic semiconductors stem from weak inter-molecular interaction in solid-state. A direct impact of weak van der Waals force is small orbital overlap between molecules and resulting narrow electronic bands. Typical bandwidth of (crystalline) inorganic semiconductors reaches several eV, whereas that of organic semiconductors is 0.1 to 0.5 eV. There are even cases where the bandwidth falls smaller than the thermal energy, which makes questionable the existence of bands extended through the entire solid. Moreover, a real challenge exists in understanding and developing charge-transport models covering a large number of material classes that have different energetic configurations related to the molecular structure itself and also the process-dependent film microstructure. Figure 2.5 shows a simplified categorization of charge transport mechanisms according to the material class and crystallinity, which will be supported by the following description.
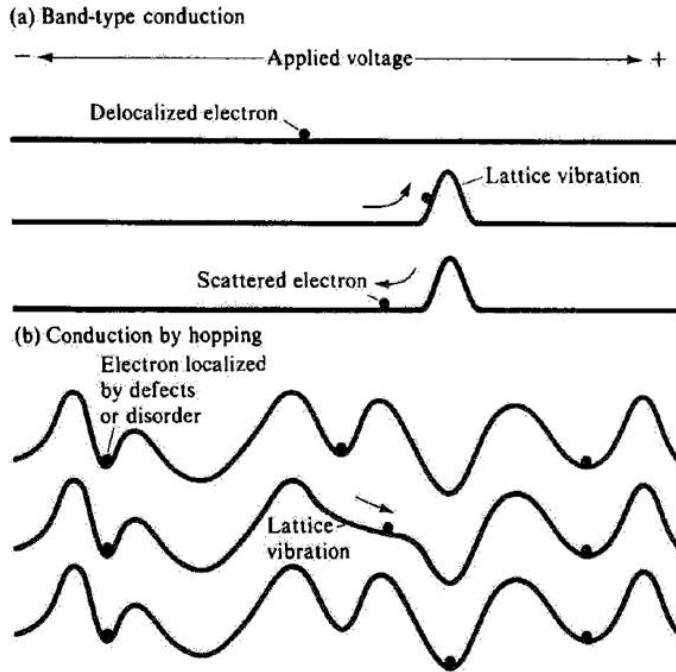
Figure 2.6: Illustration of the transport mechanisms in solids with applied electric field. (a) Band-type conduction; electrons are scattered by lattice vibration so that the mobility decreases with increasing temperature. (b) Hopping between localized states; lattice vibration can give electrons chance to overcome the potential barriers (thermally-activated transport).

2.2.1   Band transport

Drude's free electron model describes band-type conduction of delocalized electrons [21, 42]. The model assumes drift of charge carriers upon an applied electric field by repeated acceleration and collision with the lattice by which they totally lose their energy. This process results in an average drift velocity proportional to the electric field strength, from which the proportionality factor is defined as mobiltiy μ by

$$\mu = \frac{q\tau}{m} = \frac{q\lambda_m}{mv_{th}}. \tag{2.1}$$

Here, q is the elementary charge, m the effective mass, τ the mean time between lattice collisions, λ_m the mean free path, and v_{th} the thermal velocity. As illustrated in Figure 2.6(a), band transport is not thermally activated because increasing temperature reduces λ_m and μ. This behavior is usually modeled by $\mu \propto T^{-n}$ with $n > 0$ [21], where T is the absolute temperature.

However, for most organic semiconductors, band transport is unlikely because general parameters put into Equation (2.1) give μ of the order 100 cm^2/V·s or higher

[21]. In other words, the primary assumption of Drude's model fails for organics because $\mu < 1$ cm^2/V·s corresponds to a value λ_m smaller than the lattice spacing (intermolecular distance).

Therefore, we consider that real band transport is not relevant to organic semi-condutors, and it might restrict to highly-pure defect-free single crystals at extremely low-temperature [43]. It is the reason that occasional experimental observation of a negative temperature coefficient (dμ/d$T < 0$) in low-mobility organic crystals is generally described by the band-'like' transport, of which the mechanism is not fully understood yet [44–47].

2.2.2 Electronic polarization

When the charge localization effect is pronounced, the transport is described by the hopping between localized states. In this case, thermally activated transport (dμ/d$T > 0$) is expected because the lattice vibration helps localized charges to overcome potential barriers [Figure 2.6(b)]. Generally, we consider two origins of localization; polarization and disorder.

Electronic polarization is a local deformation of the electron density due to the additional charge staying at this location [48]. The consequence is an immediate relaxation of that particular state by the induced potential that in turn localizes the staying charge, which is sometimes called the self-trapping effect. Once this charge moves to another molecule (or a segment of molecule), this effect takes place again. Therefore, we can visualize this type of charge transport by the movement of charge with its accompanying polarization, and these two are together called a 'polaron'. Polaronic transport is a distinctive character of all organic semiconductors. It is again due to small transport bandwidth that results in residence time higher than polarization time, and also due to small dielectric constant in organic materials that intensifies the localizing potential.

2.2.3 Multiple trapping and release (MTR)

The second mechanism of localization is induced by energetic and geometrical disorder. When the degree of disorder is not significant (compared to the transport bandwidth), we consider 'weak localization', and the energy diagram is represented by extended states (band) plus a localized-state band tail that acts as charge trapping sites. This picture is widely-used in conventional model for amorphous silicon (a-Si) [49, 50]. For organic semiconductors, vacuum-evaporated small-molecules can
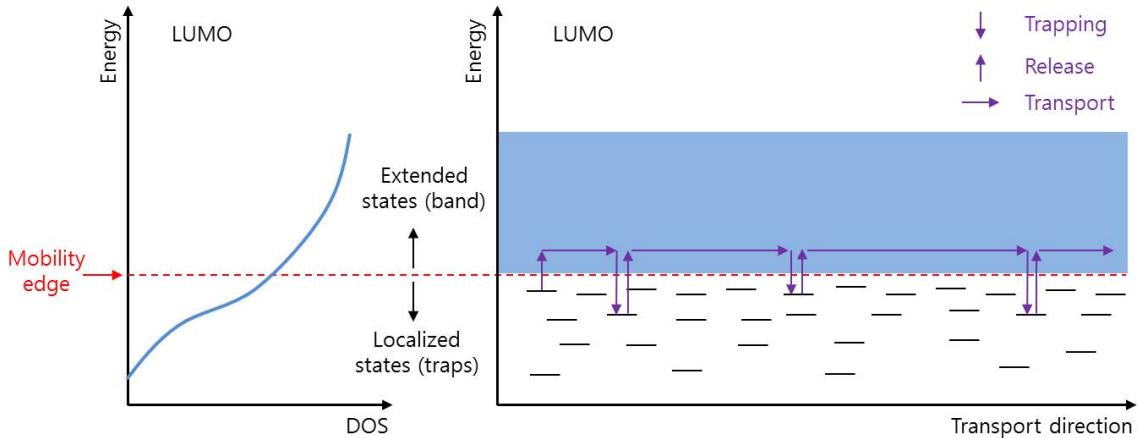
Figure 2.7: Illustration of the multiple trapping and release process. DOS consist of extended states above mobility edge (ME) and trap states below ME.

be generally well described by this model. They can form relatively well-ordered small domains with different orientation between domains, which can be regarded as poly-crystalline phase. The main origin of localized tail states in a-Si are dangling bonds, and that in polycrystalline organic semiconductors can generally be attributed to the grain boundaries [51].

In this energetic situation, the charge-transport is based on the multiple trapping and release (MTR) process illustrated in Figure 2.7. Here we only consider electron transport at LUMO level. The mobility edge (ME) is defined as the energy above which the states are delocalized, thus the mobility increases dramatically. Charge carriers tend to be trapped into the localized states and be thermally released up to the band states where an effective transport can take place. The expression for mobility is dependent on the energetic distribution of the trap states.

Exponential density-of-states (DOS) $N(E)$ for trap states are expressed by

$$N(E) = \frac{N_t}{E_t} \exp\left(-\frac{E_c - E}{E_t}\right), \tag{2.2}$$

where N_t is the total trap states, E_t the trap distribution energy, and E_c the conduction band edge (equivalent to ME). A detailed analytical formulation for obtaining trapped and free charge carrier density will be given in Section 4.1.5. Here, for discussion purpose, we simply present the expression of the effective mobility μ_{MTR} determined by the trapped-to-total carrier density,

$$\mu_{\text{MTR}} = \mu_0 \frac{n_f}{n_f + n_t} \simeq \mu_0 \frac{N_c}{N_t} \exp\left(-\frac{E_c - E_F}{k_B T}\right), \tag{2.3}$$
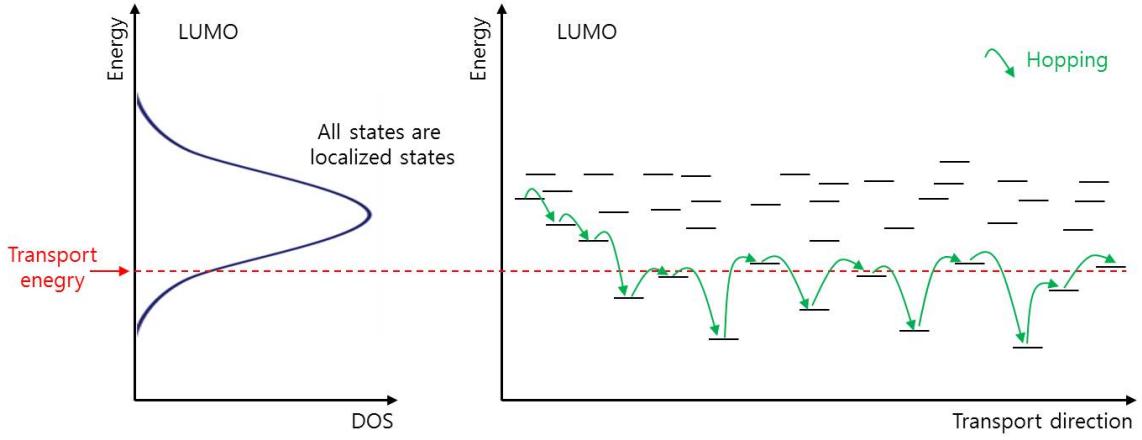
Figure 2.8: Illustration of the hopping transport through the localized states in the Gaussian disorder model (GDM). Upward hopping due to the low DOS at tail states is possible and the charge transport resembles the MTR process with the transport energy (TE) analogous to the ME.

where μ_0 is the band mobility, n_f the free electron density, n_t the trapped electron density, N_c the effective DOS at the conduction band edge, E_F the Fermi level, and k_B the Boltzmann constant. We assume $E_0 \gg k_B T$ and $n_t \gg n_f$ for Equation (2.3).

Equation (2.3) shows Arrhenius temperature dependence for thermally activated charge transport. The exponential dependence on $E_c - E_F$ manifests itself by typical phenomenological observations, such as the super-quadratic current-voltage dependence of the space-charge-limited current (Mark-Helfrich law) [52], and the power-law dependence of the gate-voltage dependent mobility in OFETs [53].

2.2.4 Gaussian disorder model (GDM)

In a system where the degree of disorder is high, such as non-crystalline polymeric films, 'strong localization' results in absence of extended band states. Therefore, all electronic states have to be regarded as localized states, and their energetic distribution is described by Gaussian distribution $g(E)$,

$$g(E) = \frac{N_0}{\sqrt{2\pi}\sigma} \exp\left(-\frac{E^2}{2\sigma^2}\right), \tag{2.4}$$

where N_0 is the total density of transport sites and σ is the half-width of Gaussian DOS.

In the Gaussian disorder model (GDM), the charge transport is based on the thermally assisted tunneling events between localized states, which is generally called hopping transport. There is no analytical solution for charge transport in the GDM.

In 1993, Bälsser reported on a Monte Carlo simulation study for the charge transport in the GDM [54], where hopping rate ν is assumed to be Miller-Abraham type [55]:

$$\nu = \nu_0 \exp\left(-\frac{2R_{ij}}{\alpha}\right) \times \begin{cases} \exp\left(-\dfrac{E_j - E_i}{k_B T}\right) & \text{if } E_j > E_i \\ 1 & \text{if } E_j < E_i \end{cases} \tag{2.5}$$

where ν_0 is the attempt frequency, R_{ij} the geometrical distance between sites, α the localization length, E_i the energy of the initial site, and E_j the energy of the arrival site. An illustration of the hopping charge transport related to Equation (2.5) is shown in Figure 2.8. Electrons at high-energy states tend to make downward hops. However, below a certain energy level, there is difficulty in finding any low-energy site with small distance R_{ij}. At this moment, they can make an upward hop toward a nearest site with the aide of thermal energy. This type of continuous process defines the transport energy (TE) around which the hopping transport proceeds [56]. Because the electrons below the TE need to be thermally elevated for efficient hopping transport, the transport near and below this TE resembles the MTR process, with the TE analogous to the ME. From the Monte Carlo simulation in [54], an empirical expression for the GDM mobility μ_{GDM} can be written as

$$\mu_{\text{GDM}} = \mu_\infty \exp\left[-\left(\frac{2\sigma}{3k_B T}\right)^2\right] \exp\left\{ C\left[\left(\frac{\sigma}{k_B T}\right)^2 - \Sigma^2\right] \sqrt{F}\right\}, \tag{2.6}$$

where μ_∞ is the mobility prefactor (zero field, high temperature limit), C an empirical constant, Σ the variance of geometrical disorder, and F the strength of electric field. Therefore, the major characteristics of this model are the non Arrhenius temperature behavior and the dependence of the mobility on the electric field.

2.3   Charge-carrier injection

2.3.1   Barrier formation

As current in unintentionally-doped organic semiconductors is carried predominantly by injected carriers, energetic at the metal/organic interface plays a crucial role on device operation.

Figure 2.9 shows a schematic representation of the energy diagram of an ideal metal/organic junction at flat-band condition. Upon considering an injection from the metal toward the organic semiconductor, the electron injection barrier E_n and the hole injection barrier E_p are given by

$$E_n = W_m - EA, \tag{2.7}$$
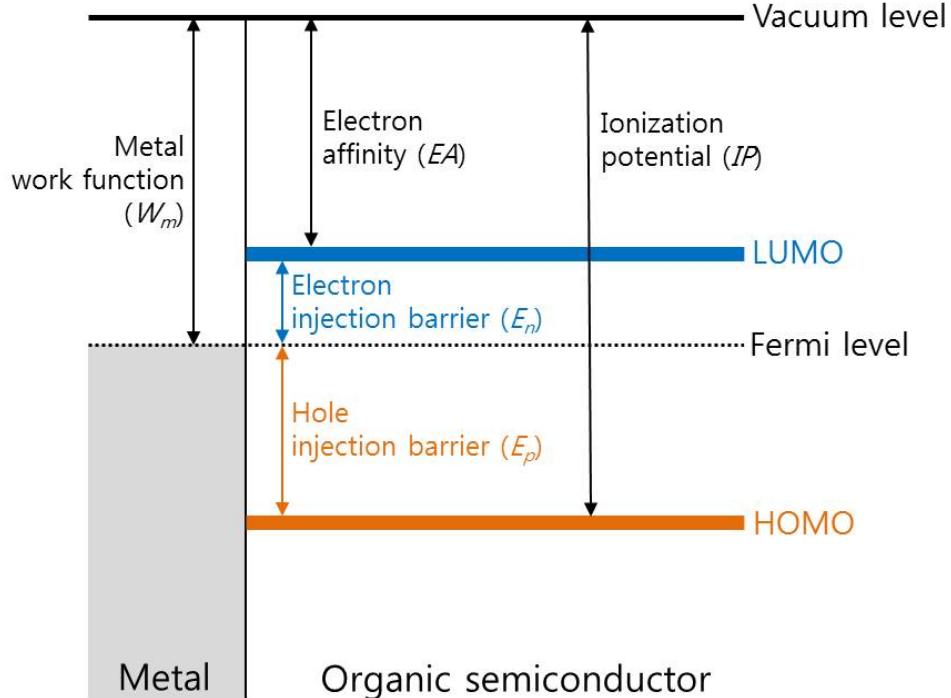
Figure 2.9: Energy diagram of an ideal metal/organic junction.

$$E_p = IP - W_m, \tag{2.8}$$

where W_m is the metal work function, EA the electron affinity of the organic semi-conductor, and IP its ionization potential.

This picture assumes the vacuum-level alignment between the two materials, which is also called the Mott-Schottky rule [57,58]. By this assumption, the carrier injection barriers are determined by the intrinsic material parameters of the organic semiconductor and the electrode metal. We can refer to the Boltzmann statistics for describing electronic distribution and express the carrier density at a metal/semiconductor interface as an exponential function of the barrier height [23]. It implies sharp decrease of the injected carrier density with increasing barrier height, thus allowing to define the type of dominant carriers by comparing E_n and E_p in a particular metal/organic combination. It means that p-type conduction is expected when $E_n > E_p$, and n-type conduction is favored for $E_n < E_p$. Ambipolar conduction can take place when the Fermi level is positioned near the middle of the HOMO-LUMO band gap because the injection barriers for both type of carriers are similar.
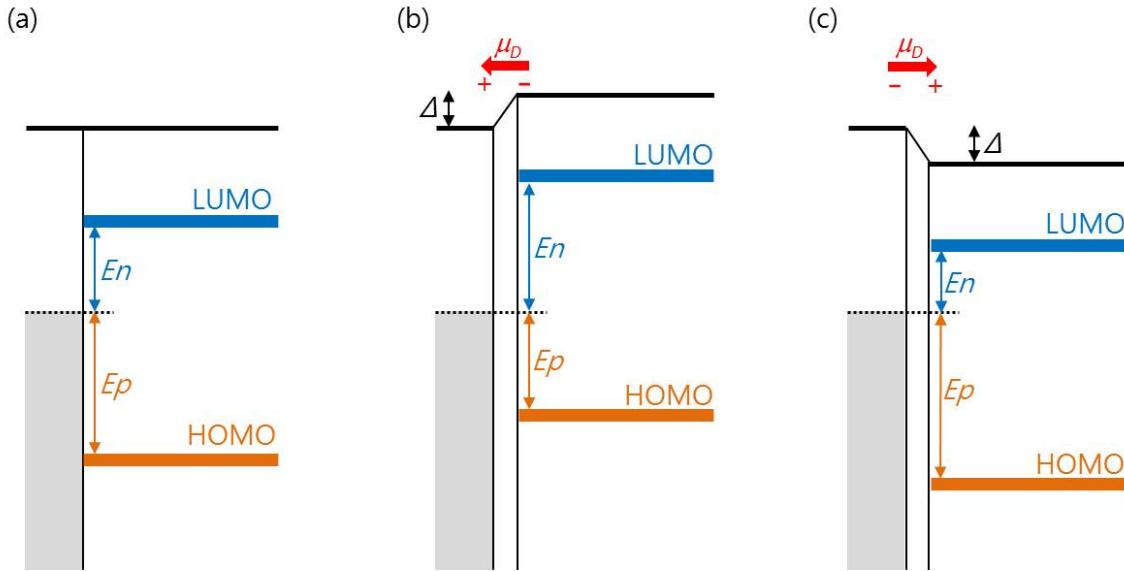
Figure 2.10: (a) Energy diagram of an ideal metal/organic junction. (b) Energy diagram of a realistic junction with an interface dipole pointing toward the metal. (c) Energy diagram of a realistic junction with an interface dipole pointing toward the semiconductor.

2.3.2   Non-ideal effects

For more realistic junctions, it has been observed that the Mott-Schottky limit is not always satisfied [59]. Measurements of the electronic structure at a metal/organic interface with a wide variety of materials show that the primary non-ideal effect is the formation of an interface dipole, which can significantly change the injection barrier heights [57, 60]. Figure 2.10 shows the formation of interface dipoles and their impact on the energy diagram. The dipole moment vector μ_D is created due to the interface dipole and, as a consequence, barrier heights are either increased or decreased according to the direction of μ_D and the type of carriers, by the magnitude Δ. The origin of interface dipole is attributed to several mechanisms; charge transfer across the interface, formation of induced or permanent dipoles into the organic layer, chemical interaction, and presence of interface states [61].

In the case where the density of interface states is very high, a Fermi-level pinning can take place. The injection barrier becomes independent on the metal work function, which means an extreme case where the choice of a contact metal has no importance for the resulting injection barriers [62,63]. This phenomenon accounts for an important implication for organic devices; they should generally bear a substantial injection barrier that cannot vanish below a certain level determined by the position of the pinned Fermi level.

Chapter 3

Methods

Upon analyzing and modeling various organic device geometries, we have consistently used multiple approaches in order to benefit from balanced and enhanced understanding of each device and observation. In this chapter, the techniques or methods used in the thesis are categorized into four fields; impedance spectroscopy, analytical modeling, numerical simulation, and experimental investigation. Background and purpose of each method, with practical explanation on how to use a particular method, are provided to help understand the results in Chapters 4.

3.1 Impedance spectroscopy

3.1.1 Generalities

Impedance (Z) of an electrical component is defined as the ratio of the phasor voltage and the phasor current measured in ohms (Ω) [64]. We denote the impedance of three basic circuit elements as Z_R, Z_C, and Z_L, in which the subscript indicates the corresponding element as illustrated in Figure 3.1. The relationship between the
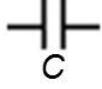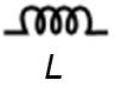
$$Z_R = R \qquad Z_C = \frac{1}{j\omega C} \qquad Z_L = j\omega L$$

Figure 3.1: Impedance of passive circuit elements.

Series connection

Parallel connection

$$Z_{tot} = Z_1 + Z_2 + Z_3 \qquad\qquad Z_{tot} = \left(\frac{1}{Z_1} + \frac{1}{Z_2} + \frac{1}{Z_3} \right)^{-1}$$
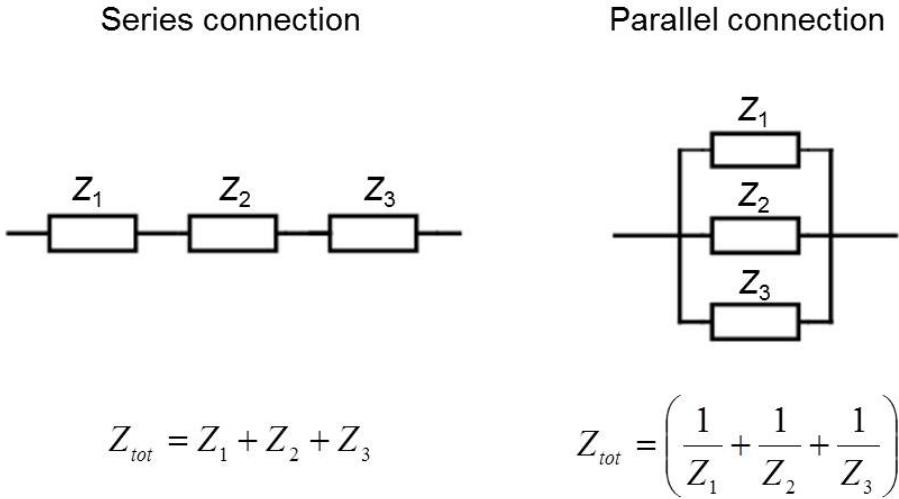
Figure 3.2: Total impedance of a series impedance circuit and a parallel impedance circuit by combination rules.

circuit parameter (R, C, L) and the impedance (Z_R, Z_C, Z_L) is also given in this figure.

In the case when several impedance elements are connected in an arbitrary manner, we are able to estimate the total impedance Z_{tot} (also called equivalent impedance or terminal impedance) of the whole circuit by using the combination rules. Figure 3.2 illustrates the combination rule for a series connection and that for a parallel connection of impedance elements. The equations are more familiar when we assume that all the elements are resistors, and we note that the same rules hold for any arbitrary impedance elements.

3.1.2   Equivalent circuit modeling

Our particular interest in the thesis is to use impedance spectroscopy for equivalent circuit modeling of two-terminal organic devices (organic diodes). Impedance spectroscopy is a well established technique, by which we measure complex impedance of a given electrical or electrochemical system while sweeping the ac small-signal frequency usually at a fixed dc voltage [65]. Because every circuit element responds differently to the frequency ω (Figure 3.1), a full spectrum of impedance spectroscopy provides the information on which elements exist in the system and how they are connected to each other. In other words, one can extract a realistic equivalent circuit of a two-terminal device under analysis by measuring its total impedance over a broad frequency range. This whole process from the measurement to the extraction of an equivalent circuit

with the exact circuit parameters (R, C, L, etc.) is to be called impedance modeling, impedance fitting, or equivalent circuit modeling. More advanced analysis involves assigning physical meaning to particular circuit elements and monitoring the variation of circuit type and parameters upon different measurement or biasing conditions. In the literature, there are many reports showing practical applications of impedance spectroscopy to the analysis of organic devices [66–70].

3.1.3 Typical impedance spectra

A basic knowledge on typical impedance data of simple circuits is helpful for a quick guess after conducting measurements and plotting the experimental data. Here, we describe several simple and representative circuits.

The simplest one to be discussed is the parallel resistance and capacitance (RC) circuit. The total impedance of an RC circuit (Z_{RC}) is calculated by the combination rule

$$Z_{RC} = \frac{1}{\frac{1}{Z_R} + \frac{1}{Z_C}} = \frac{R}{1 + j\omega RC}. \tag{3.1}$$

Equation (3.1) can be manipulated to get separate real and imaginary part of Z_{RC},

$$\mathrm{Re}(Z_{RC}) = \frac{R}{1 + \omega^2 R^2 C^2}, \tag{3.2}$$

$$\mathrm{Im}(Z_{RC}) = -\frac{\omega R^2 C}{1 + \omega^2 R^2 C^2}, \tag{3.3}$$

where $\mathrm{Re}(Z_{RC})$ and $\mathrm{Im}(Z_{RC})$ represent the real and imaginary part of Z_{RC}, respectively. Equations (3.2) and (3.3) show that the impedance-frequency spectrum of an RC circuit visualized on a complex plane draws a characteristic semicircle because they meet the condition

$$\mathrm{Im}(Z_{RC}) = -\sqrt{\left(\frac{R}{2}\right)^2 - \left[\mathrm{Re}(Z_{RC}) - \frac{R}{2}\right]^2}, \tag{3.4}$$

which corresponds to the equation of a lower semicircle centered at ($\frac{R}{2}$, 0) with a radius of $\frac{R}{2}$.

As Equations (3.2) and (3.3) are analytical expressions of R, C, and w, we can calculate and plot the impedance of an RC circuit by assuming values of R and C with a certain frequency range. A more practical and general way to predict impedance spectra is to use an impedance spectroscopy software, which usually features impedance data fitting and also simulation of user-defined circuits. Figure 3.3 shows the simulated impedance spectra of the RC circuits by EC-Lab software [71]. When $f \to 0$,
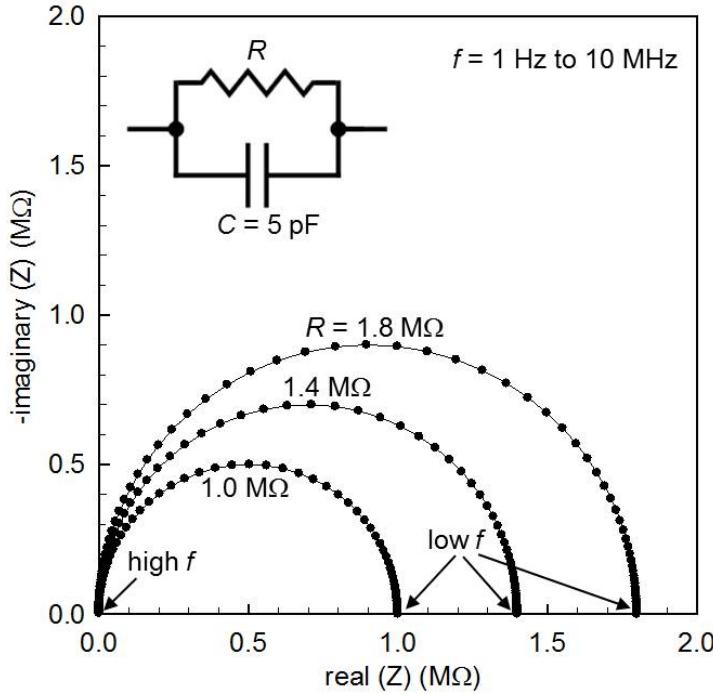
Figure 3.3: Complex-plane representation of the simulated impedance spectra of an RC circuit with a fixed capacitance and different resistance values. Simulation frequency points are from 1 Hz to 10 MHz with 20 points per decade.

the impedance modulus of a capacitor $|Z_c| \to \infty$, so that the capacitance branch becomes open-circuited and the circuit reduces to a resistor. It explains why the marked low-frequency impedances are only real numbers corresponding to R. In contrast, when $f \to \infty$, the whole circuit becomes short-circuited due to $|Z_c| \to 0$, which explains the convergence to zero of all the three curves at high frequency.

The uppermost point of a circular arc has an importance because the frequency corresponding to that point contains the time constant (RC) of that parallel RC circuit. We define it as a characteristic frequency (ω_{RC} or f_{RC}). As $\mathrm{Im}(Z_{RC})$ has the minimum value at this point, we can calculate from Equation (3.3) to see that

$$\left. \frac{d\mathrm{Im}(Z_{RC})}{d\omega} \right|_{\omega = \omega_{RC}} = 0 \tag{3.5}$$

is fulfilled when

$$\omega_{RC} = 2\pi f_{RC} = \frac{1}{RC}. \tag{3.6}$$

The effect of a series resistance R_s connected to a parallel RC circuit is shown in Figure 3.4. In principle, it is also possible to deduce mathematical expressions of the total impedance of any circuits by using the combination rules. However, we only present the simulation results for the purpose of emphasizing the expected
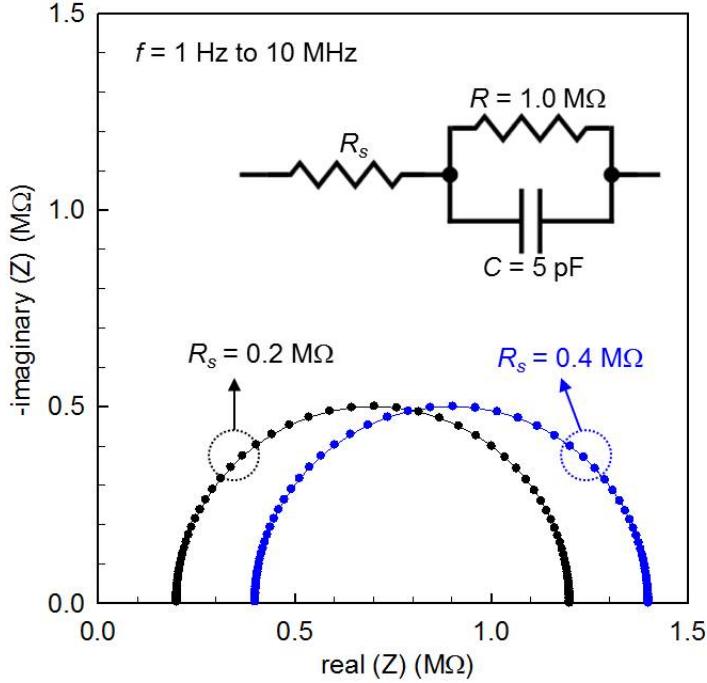
Figure 3.4: Complex-plane representation of the simulated impedance spectra of the circuit in the inset with different series resistance R_s values. Simulation frequency points are from 1 Hz to 10 MHz with 20 points per decade.
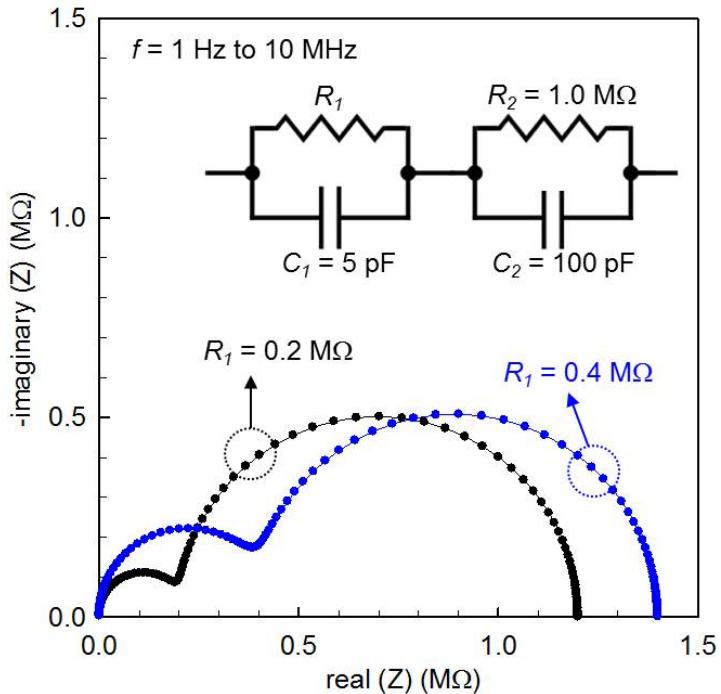
Figure 3.5: Complex-plane representation of the simulated impedance spectra of the circuit in the inset with different R_1 values. Simulation frequency points are from 1 Hz to 10 MHz with 20 points per decade.

impact of R_s on the impedance spectra. It appears that adding a series resistance results in a horizontal shift of the impedance semicircle. In other words, there is a non-zero modulus of the high-frequency impedance. It is because the short-circuiting capacitance branch with $f \to \infty$ only eliminates the parallel RC element. Therefore, characteristic features of such circuits are the low-frequency impedance equal to $R_s + R$ and the high-frequency value corresponding to R_s. In device analysis, the observation of a series resistance is generally attributed to the contact resistance that arises from the charge-injection problem at the metal/semiconductor interface [72, 73].

Figure 3.5 shows the simulated impedance spectra of the circuit of two series-connected parallel RC elements. Expected impedance spectrum of such a circuit is a curve composed of two intermixed semicircles. The characteristic frequency of each semicircle is given by the time constant of each RC element. An observation of two RC elements in experimental results is often considered to be evidence for two spatially distinguished regions, such as interface and bulk regions within a semiconductor film, where the conductivity of one region can be significantly lower than that of the other region [67].

3.2   Analytical modeling

3.2.1   Physical point of view: Goals and limitations

Analytical modeling plays a pivotal role throughout the entire thesis. In a practical sense, we use the word 'analytical modeling' as the process of mathematical step-by-step development of given physical problems for the purpose of obtaining a closed-form equation. This approach will be exemplified by developing the current-voltage equation of organic diodes in Chapter 4 and the charge-based contact resistance model for OFETs in Chapter 5. The goal of analytical modeling is thus to establish more realistic and physically-reliable equations that efficiently capture universal device operations and to use them as an interpretation and prediction tool for real devices.

An apparent limitation is that analytical modeling rarely ends up with a 'fully' analytical equation. For contextual clarity, we define an 'analytical model' as a closed-form equation in which all parameters and variables appear explicitly. In other words, an analytical model should allow straightforward calculation without involving unsimplified integrals, differential equations, and/or iterative processes. Often, an analytical modeling flow encounters a moment at which no further mathematical manipulation toward a compact equation is possible. In this case, the final equation can

be called a 'semi-analytical model' because it is based on an analytical process but requires a numerical computation for getting the final value.

Another point to be addressed is that analytical modeling is inevitably accompanied by numerous approximations and simplifying hypotheses. It is a definite but necessary limitation when using analysis for tackling a complex problem. This aspect is to be regarded as a sacrifice for applicability. However, this simplification is often justified by proving the validity of the approximation under specific operation range, or by comparing with the numerical results.

3.2.2 Device models for circuit simulation

According to the definition in [74], a compact model is a mathematical description of an electrical component as used by circuit designers and technologists to mimic the electrical device behavior in a technology. A particularly important interest in developing analytical models, even by tolerating compromising simplification, is to eventually integrate them into a circuit simulator. In widely-used SPICE simulators, characteristic devices are represented by corresponding compact models [75,76]. Compactness of a current-voltage equation of an electronic device is of great importance, because it enables fast convergence in the calculation of a circuit that can possibly contain hundreds or thousands of various electrical components.

On that account, developing a fully compact model also requires empirical methods for extending its operation range. As best exemplified by our compact modeling approach of organic gap-type diodes and OFETs, there is a need to introduce transition functions that merge equations for discrete regimes into a single analytical equation.

3.3 Numerical simulation

3.3.1 How a device simulator works

We have used the commercially available device simulator ATLAS from Silvaco, Inc [77] for numerical simulation of organic devices. ATLAS is a well known device simulation framework for technology computer-aided design (TCAD) in semiconductor industry. This simulator is specified to be physically-based finite-element two-dimensional simulator. A full description of various modules, supported materials and physical models, and detailed numerical algorithms can be found in the provider's manual. Here, we explain briefly the most basic and practical working principles.
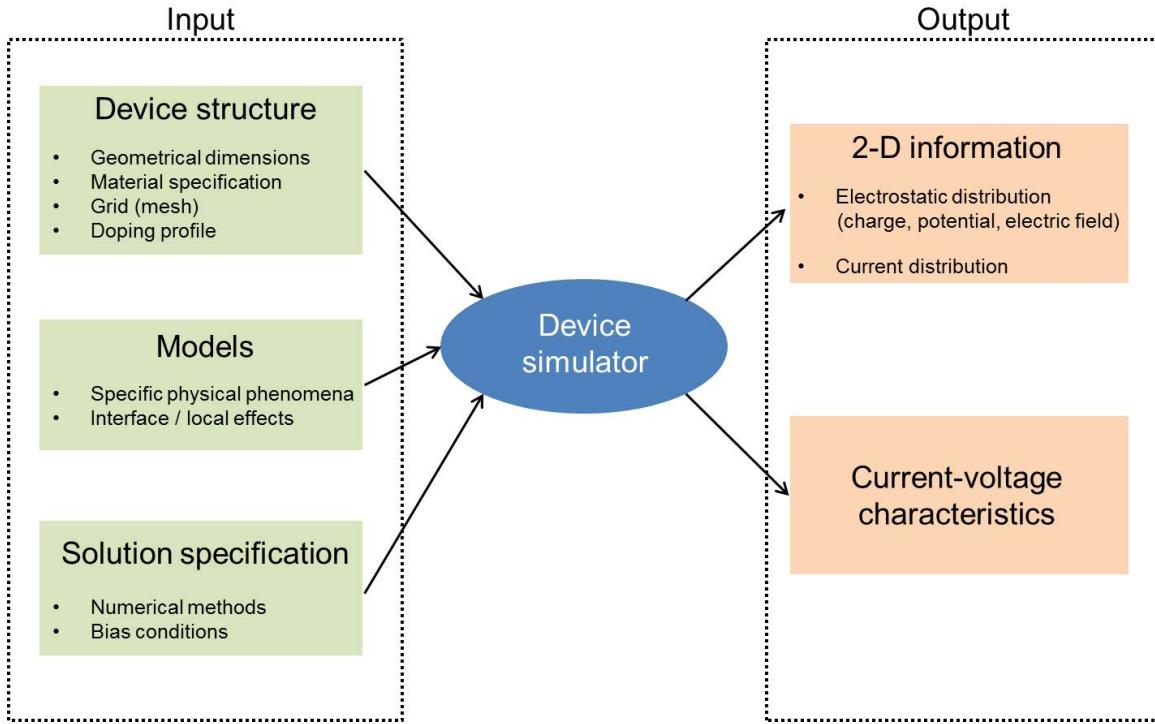
Figure 3.6: Illustration of the working principle and flow of the 2-D physically-based finite-element simulator.

The simulator calculates a set of physical equations in a user-defined device structure, which is approximated to a two-dimensional (2-D) mesh (or grid). In Figure 3.6, the function of this type of simulator is illustrated by specifying the information required to run a simulation, and the results obtained for analysis and design. The device structure is first defined by specifying the size of the whole structure, followed by dividing it into different parts or layers. Material specification consists of assigning conventional or newly definable semiconductors, metals, or insulators to each part of the 2-D structure. Defining a mesh structure involves turning a continuous medium into many (finite number of) cross section points of the grid lines. The desired spatial distribution of the dopants inside semiconductors can be inserted in a highly controlled manner. Then, one can choose, among a wide variety of supported physical models, the models to be included for the calculation. The default models include Poisson's equation, carrier continuity equation, and drift-diffusion transport model. In addition to them, specific density of states models, mobility models, defect/trap models are available based on the recent technological developments. It is also possible to simulate any local and interface effects by confining the application of the chosen models to any specific location inside a layer. Numerical methods for
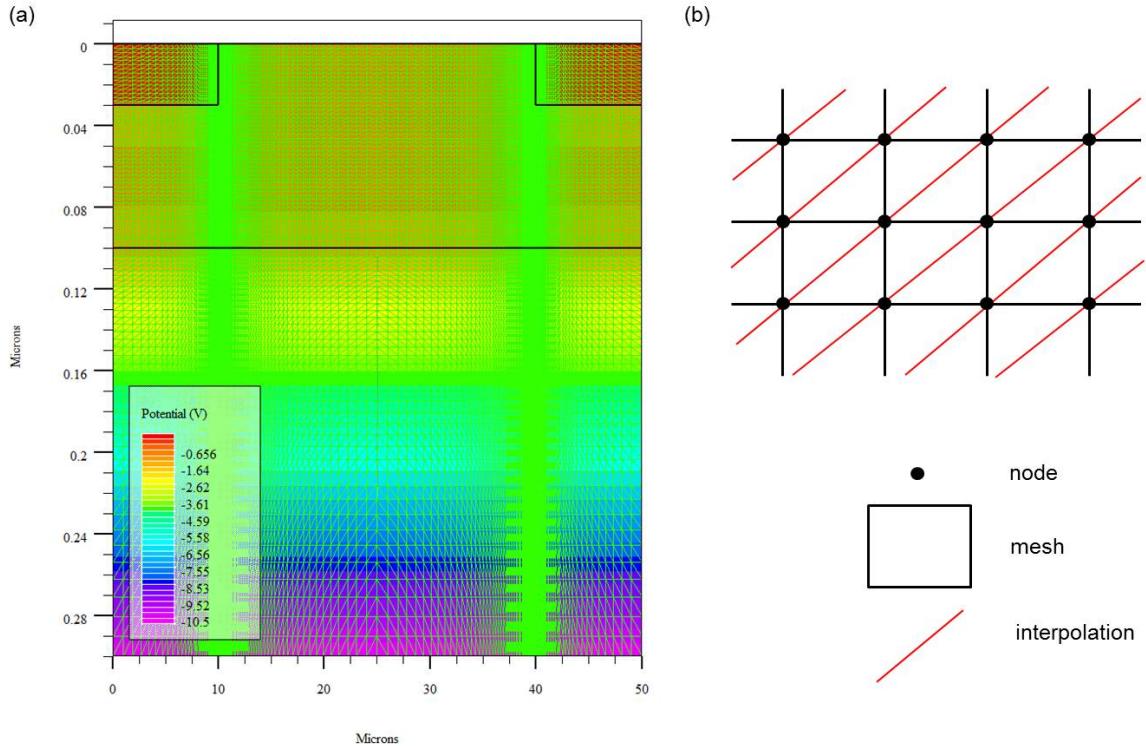
Figure 3.7: (a) Example of a non-uniform mesh structure for an OFET. The color contour map represents the simulated 2-D potential distribution. (b) Illustration of the mesh, nodes, and interpolation lines.

calculating the solutions are to be specified. We can select the degree of coupling the system of equations, number of carriers in this statement. Finally, the bias condition should be defined either by giving a fixed value, or by writing a sweeping range at each electrode.

The work of a simulator is to solve all the specified equations within the defined 2-D structure, in a way that the final solution is self-consistent at every mesh point. The success of a calculation manifests itself by the convergence of the problem without any error.

There are basically two possible output analyses after a calculation is done. The final structure contains the 2-D solutions of the calculation at a fixed bias condition. We can extract the 2-D contour maps of potential, electric field, charge, and current distribution. If a bias sweeping syntax was inserted in a input file, current-voltage characteristics are saved in another type of output file.

3.3.2   Defining a mesh

Because simulation is based on the finite-element method, mesh definition before calculation is an important step to conduct efficient simulation and to get exact results. Figure 3.7(a) shows an example 2-D output file from ATLAS and Figure 3.7(b) is a simplified illustration of the mesh structure. Basically, using a fine mesh that contains very closely-defined lines results in more reliable results because it approximates well a real continuous medium. However, the simulation time gets longer as the number of cross-section points (nodes) is increased. Therefore, it is reasonable to define high-resolution fine mesh only within the most important region where the analysis is to be made, with a relatively coarse mesh elsewhere. We applied this principle of making use of a non-inform mesh, with a significantly improved accuracy at metal/semiconductor interfaces. ATLAS provides exact solutions at each node defined by the grid lines, and also calculates interpolation values along the diagonals as illustrated in Figure 3.7(b). There is a maximum allowed node limit of 10^6, which is large enough in most cases.

3.3.3   Use in device modeling

In contrast to the analytical modeling, the numerical simulation does not directly lead to any apparent mathematical relationship between input and output quantities. We rather consider the ensemble of all the specified inputs (structure, mesh, models, parameters, etc.) as a numerical model when the calculation outputs well match and explain experimental characteristics. Building such 2-D numerical models for OFETs can be exemplified by the results in [78, 79], where the systematic variation of the contact geometry and injection barrier is simulated to predict physical behaviors.

Another important use of the numerical method, emphasized in our results, is to check the validity of the analytical models. After achieving an analytical expression for charge distribution or current-voltage relationship, for example, we can compare the analytical calculation to the numerical simulation with identical parameters, to justify the approximations and approaches made for analytical developments.

3.4   Experimental investigation

Basically, modeling consists of making a model that can explain, fit, and eventually predict a real world problem. Therefore, through the whole study, we made a continuous effort to keep a good balance between theory and experiments. As a consequence,

the results of all the five types of studied devices are supported by both theoretical and experimental work.

The main purpose of using experimental results is to compare with a developed model, to finally confirm its validity. From another point of view, an experimental observation can be q starting point of model development. The best example of the latter approach is the experimental observation of full depletion in unintentionally-doped organic semiconductors (Section 4.1), which formed the solid basis for the zero-doping assumption that has been applied to the rest of the results.

In order not to interrupt a natural flow of the explanation, all the experimental details on the device fabrication and characterization are collectively given in Appendix C.

Chapter 4

Modeling organic diodes

In this chapter, the term 'diode' is used by its broadest meaning, which indicates a device containing two (di-) terminals. The choice of a metal basically determines how the device functions, or more precisely, the charge injection barrier at each of two metal/organic interfaces is a dominating factor in predicting the device operation. To obtain substantial currents in a diode, at least one of the two electrodes has to form an 'injecting' contact that has a sufficiently low energy barrier into the transport orbital of the given organic material. In contrast, a metal with a high injection barrier is to be called a 'blocking' contact, and it can only extract or collect the carriers injected from the injecting contact.

Based on the above clarification, we graphically describe in Figure 4.1 three characteristic diode structures which have been studied in the thesis. One can realize that there are two criteria applied to the appellation of each structure; the current-flow direction (with respect to the substrate) and the sameness of the two contact metals. Various theoretical and experimental methods have been adopted to understand or model the specific behaviors of each diode configuration.
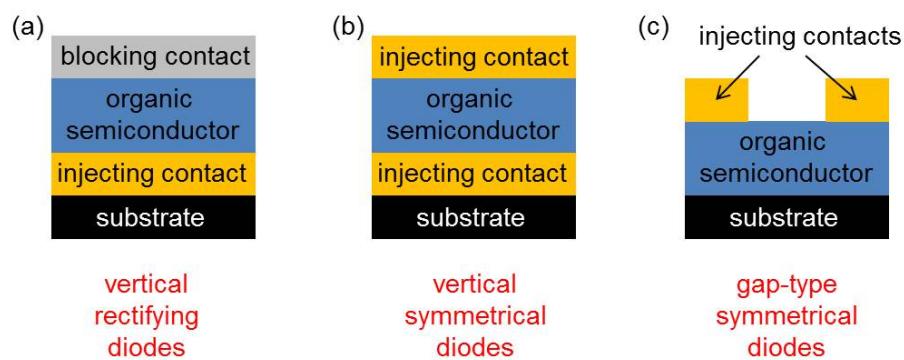
Figure 4.1: Illustration of the different diode structures.

4.1 Vertical rectifying diodes

4.1.1 Metal-insulator-metal (MIM) model

An organic layer with an injecting contact and a blocking contact forms a rectifying diode. In the literature, Steudel and co-workers successfully demonstrated the single organic layer diodes with the Au/pentacene/Al structure as a high-frequency rectification unit, which is of great interest for the radio-frequency identification (RF-ID) tag application [80, 81]. The work by Haldi and co-workers [82] also shows the electrical characteristics of the rectification diodes in ITO/organic/Al structure. They used C_{60}, pentacene, 4,4'-bis[N-(1-naphthyl)-N-phenyl-amino]biphenyl (α-NPD), and a N,N'-bis(m-tolyl)-N,N'-diphenyl-1,1'-biphenyl-4,4'-diamine (TPD) based polymer as an organic semiconductor.

Because of their behavioral similarity, single-layer organic rectification diodes have been generally described as conventional Schottky diodes [83–85], where the current is dominated by the modulation of the depletion width at the blocking interface (Schottky contact) [21]. An underlying assumption of a Schottky contact is that the depletion width is smaller than the semiconductor thickness, or in other words, the semiconductor layer is only 'partially' depleted at thermal equilibrium. When this assumption holds, reverse bias applied to a diode widens the depletion region, and in turn decreases the measured depletion capacitance (C_d). This forms the basis for the so-called Mott-Schottky analysis, for which one plot $1/C_d^2$ as a function of the applied voltage, to extract the doping concentration and the built-in potential [23, 86].

However, a constant reverse bias capacitance in rubrene organic diodes has recently been observed, which implies that the doping concentration is so low that the entire organic layer is already depleted at thermal equilibrium [87]. When assuming uniform doping, the depletion width W_d is dependent on the doping concentration N_a [21] through

$$W_d = \sqrt{\frac{2\epsilon_s(V_d - V_a)}{qN_a}}, \tag{4.1}$$

where ϵ_s is the permittivity of the semiconductor, V_d the diffusion potential, V_a the applied anode voltage, and q the elementary charge. V_d is also called built-in potential, and it arises from the work function difference between the metal and the semiconductor. Figure 4.2(a) illustrates the 'conventional' energy diagram of a metal/semiconductor junction at thermal equilibrium (V_a= 0 V). The deletion region is localized at the junction interface, because W_d is normally 'assumed' to be smaller than the semiconductor thickness. In Figure 4.2(b), the expected depletion width,
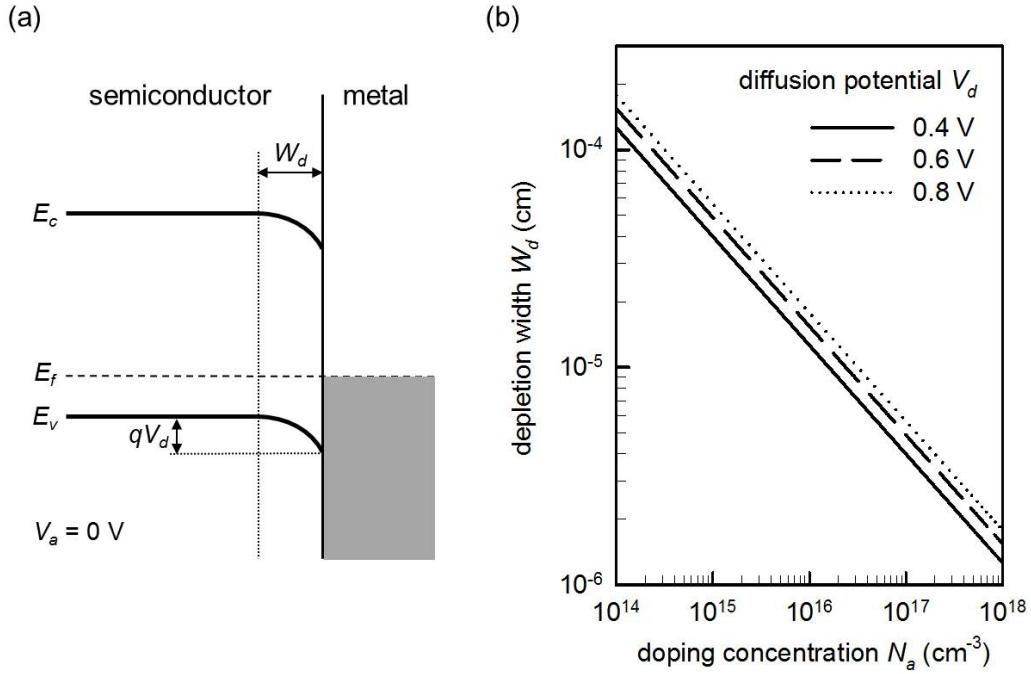
Figure 4.2: (a) Energy band structure at a metal/p-type semiconductor interface at thermal equilibrium (V_a= 0 V). E_c: conduction band edge, E_v: valence band edge, and E_f: Fermi level. (b) Calculated depletion width as a function of doping density at several diffusion potential values.

calculated by Equation (4.1), is drawn as a function of doping level. Here, the fixed parameters for calculation are $\epsilon_s = 3.6 \times \epsilon_0$, $V_a = 0$ V, with ϵ_0 as the permittivity of vacuum. Note that, when N_a is lower than $\sim 10^{16}$ cm^{-3}, W_d becomes larger than 100 nm. When W_d exceeds the semiconductor thickness, the depletion region extends until it reaches the opposite contact, and the film is 'fully' depleted. In this case, a reverse bias cannot modulate the depletion capacitance, because it cannot widen the depletion region any more.

In order to bring more evidence for the 'full depletion' concept, we fabricated and analyzed rectifying organic diodes with thick pentacene layers. Figure 4.3 shows the measured current-voltage (I_a-V_a) characteristics of the Au/pentacene/Al diodes with 520 nm and 1.0 μm pentacene films. The active area of both devices is 4.3×10^{-4} cm^2. In this structure, the bottom Au electrode serves as an injecting contact and the top Al is a blocking contact. The Fermi levels of both Au and Al are expected to be far below the LUMO level of pentacene, and therefore the diodes are described as unipolar hole-only devices. As shown in Figure 4.3(a), the fabricated devices exhibited significantly high rectification ratio.
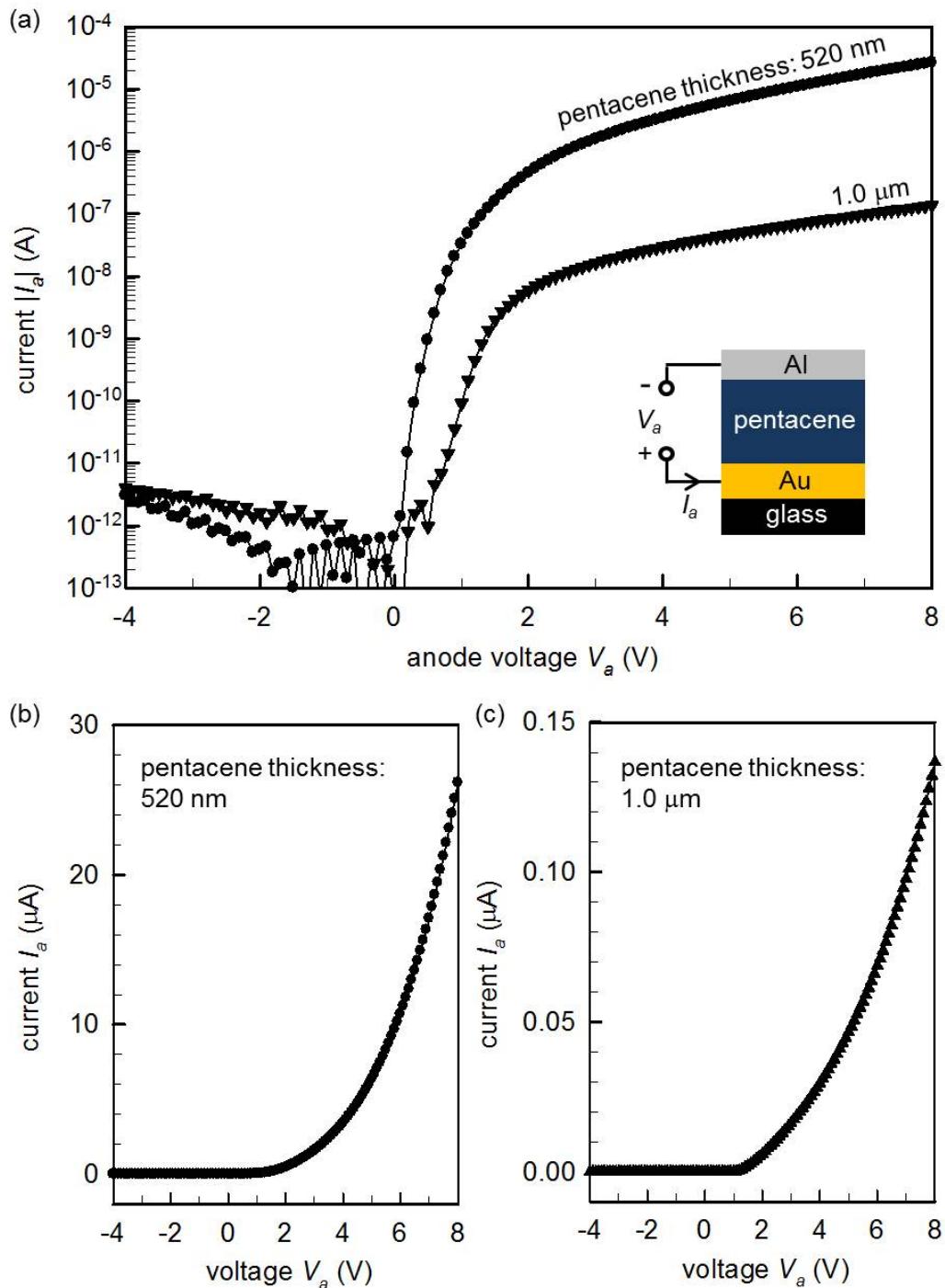
Figure 4.3: (a) Current-voltage characteristics of the pentacene diodes fabricated with the structure depicted in the inset. The applied voltage corresponds to the voltage at the bottom Au contact with the top Al electrode grounded. This plot is drawn on a semi-logarithmic scale. (b) and (c): the same results drawn on a linear scale.
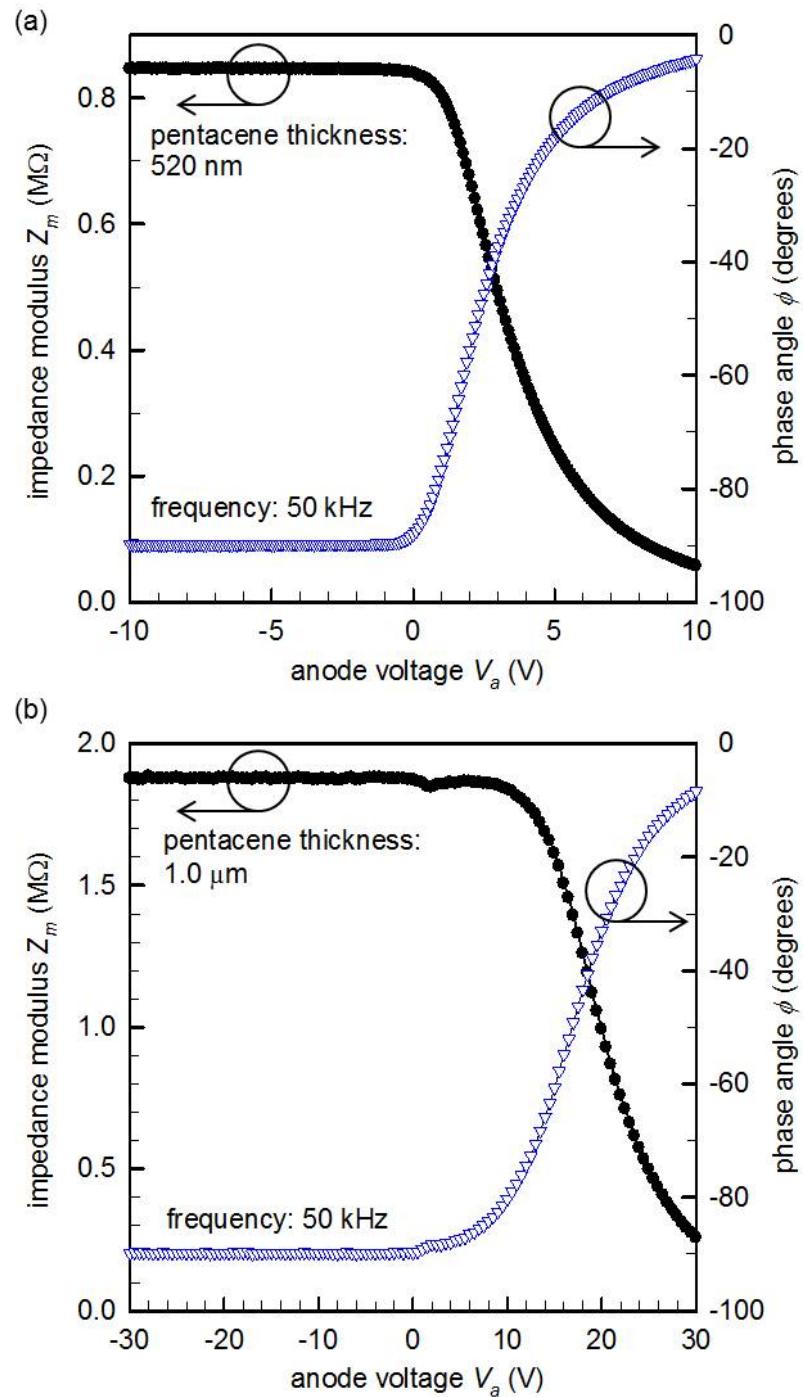
Figure 4.4: Impedance-voltage characteristics of the pentacene diodes with (a) 520-nm-thick pentacene and (b) 1.0-μm-thick pentacene.

The electrical impedance of both devices were measured as a function of V_a. Figure 4.4 shows the impedance-voltage characteristics represented by separate modulus and phase angle. First, in the reverse-bias regime, the phase angle is fixed at -90° and the modulus remains constant. It means that the diodes show purely capacitive behavior and the capacitance does not depend on the applied reverse bias. Next, when the diodes are positively biased, the current increases rapidly, thus leading to decreasing Z_m. Phase angle ϕ departs from -90° and approaches zero, which means that the resistive component of the total impedance becomes more and more dominant with increasing V_a.

The observed full depletion in 1.0-μm-thick film implies that the doping concentration in pentacene is extremely low. We can estimate the upper limit of the doping concentration N_a of pentacene by Equation (4.1). By assuming $V_d = 0.6$ V and $\epsilon_s = 3.6 \times \epsilon_0$, it is revealed that the depletion width W_d over 1.0 μm can be achieved when doping concentration N_a is lower than 2.4×10^{14} cm^{-3}. Organic semiconductors are mostly used as undoped form in applications, except for the cases where deliberate electrical doping is desirable [88,89]. In any cases, ambient oxygen can serve as molecular dopant in p-type molecular matrix [90], which is called 'unintentional' doping of organic semiconductors. The estimated doping concentration as low as $\sim 10^{14}$ cm^{-3} indicates that unintentional doping agents only lightly doped our pentacene films.

It is important to note that, under full depletion, the diode characteristics cannot be correctly described as a Schottky contact due to the non-existence of depletion modulation. Therefore, organic diodes should be explained by the metal-insulator-metal (MIM) model in Figure 4.5. At variance with the conventional picture in Figure 4.2(a), MIM diagram is based on the thermal equilibrium established by the Fermi-level alignment between the electrodes at both sides of the semiconductor. The fully-depleted sandwiched organic layer has straight band profiles, which is characteristic of an electrical insulator. The electrical conductivity of a diode is entirely due to the 'injected' carriers, and the organic layer is to be regarded as a transporting medium for injected carriers.

In the reverse-bias regime [Figure 4.5(a)], strong electric field inside the diode prevents any transport of the injected holes at the anode toward the cathode. Reverse current is extremely low, because Al cathode here cannot inject a sufficient amount of either type of charge carriers. When a small forward bias is applied ($0 < V_a < V_d$), the electric field is significantly lowered, and as a result, the high-energy holes at the anode side can overcome the potential barrier to reach the cathode. The current in this regime is thus strongly injection limited, and exponentially increases with increasing
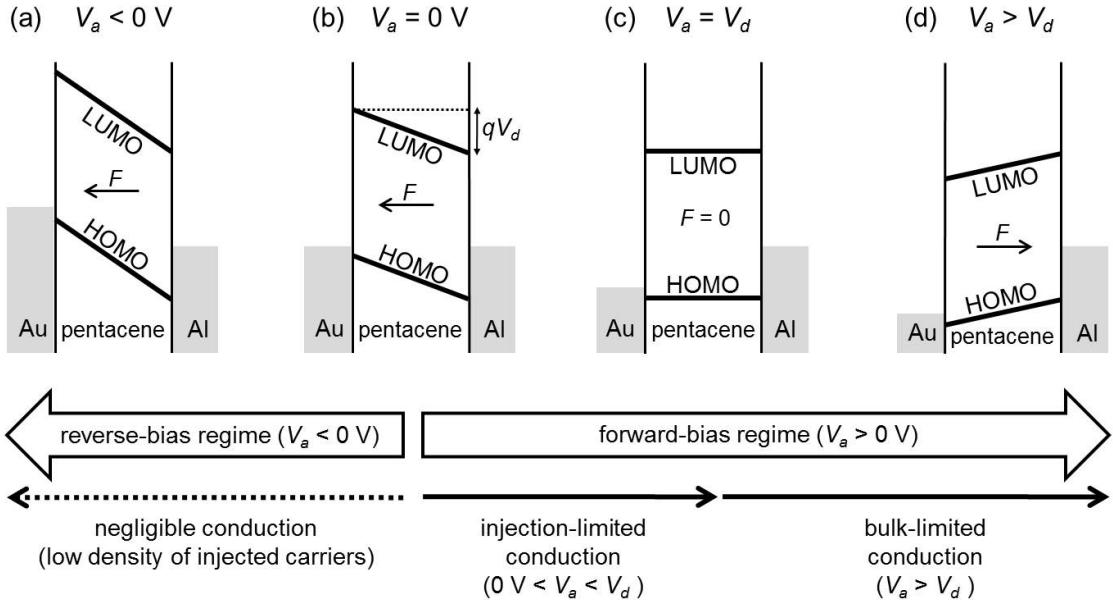
Figure 4.5: MIM-type energy diagram of a pentacene diode at different operation regimes. (a) Reverse-bias regime, (b) thermal equilibrium, (c) flat-band condition, (d) bulk-limited regime. The lower panel indicates the dominant conduction mechanisms under each bias condition.

V_a [see Figure 4.3(a)]. Finally, when V_a exceeds V_d, the internal electric field now favors the drift of the anode-injected holes. Consequently, the current is no longer injection-limited but limited by the bulk conductivity of the organic semiconductor.

4.1.2 Frequency-dependent impedance analysis

Impedance-voltage (Z-V) characteristics shown in Figure 4.4 indicate that the pentacene MIM diode is equivalent to an ideal capacitor ($\phi = -90°$) in the reverse-bias regime. Under forward-bias, on the other hand, the phase angle is intermediate $-90° < \phi < 0°$, which means that both capacitive and resistive elements contribute to the frequency response of the device. In order to find an appropriate equivalent circuit in this regime, we have conducted impedance spectroscopy on a forward-biased diode with 520 nm of pentacene.

The impedance-frequency (Z-f) data obtained over a frequency range from 5 Hz to 2 MHz are represented on a complex plane in Figure 4.6(a). It is observed that at various V_a, the data curves are close to ideal semicircles, which means that the forward-biased pentacene diode can be well described by a simple parallel RC circuit. The fitting result shown in Figure 4.6(b) confirms the correctness of the use of an RC equivalent circuit. Note that this observation can be distinguished from more complex
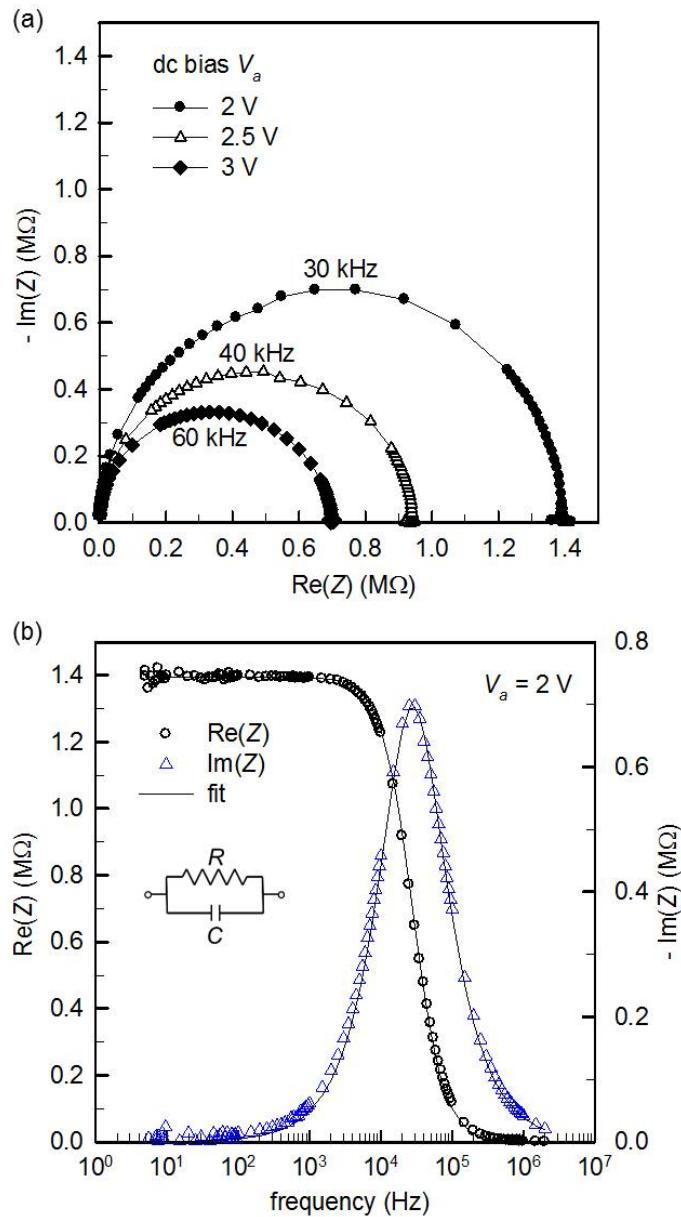
Figure 4.6: (a) Impedance spectroscopy data of a Au/pentacene/Al diode on a complex plane (Nyquist digram). Device area: 4.3×10^{-4} cm^2, pentacene thickness: 520 nm. Data obtained with three different dc voltages are shown. The frequency values written on each curve is the characteristic frequency that gives the maximum -Im(Z) point at each measurement. (b) Separate real and imaginary impedance data with $V_a = 2$ V drawn as a function of ac frequency. The symbols represent the experimental data and the solid lines are the fitting curves by using a parallel RC equivalent circuit (inset).
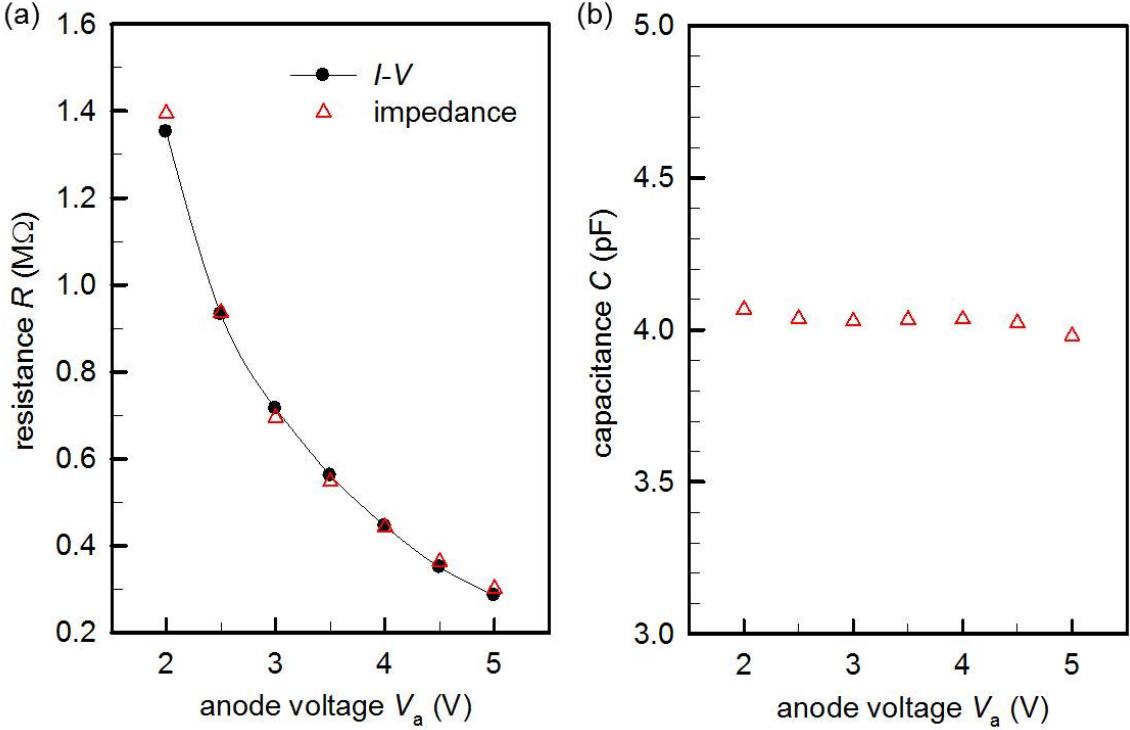
Figure 4.7: (a) Resistance from the impedance modeling in comparison with the current-voltage characteristics. (b) Capacitance from the impedance modeling.

equivalent circuits often needed to fit the experimental data on organic diodes. For example, when the metal/organic interface region is damaged or oxidized, there is possibility of observing a second parallel RC element as shown in [87]. Another possible situation is the existence of a high contact resistance, which manifests itself by a series resistance connected to the bulk RC element [72, 73].

We realized that Z-f measurements at other V_a values could also be fitted to the RC parallel circuit, with the two circuit parameters varying by changing V_a. The extracted resistance and capacitance values are plotted as a function of V_a in Figure 4.7. Resistance in Figure 4.7(a) is decreasing with increasing V_a, which is in line with the superlinear rise of the current in the space-charge-limited conduction (SCLC) regime. The resistance from the impedance equivalent-circuit model is also in good agreement with the resistance calculated from the I-V characteristics in Figure 4.2. Capacitance in Figure 4.7(b), on the other hand, is practically constant over the measurement range, which is because this capacitance corresponds to the geometrical capacitance determined by the overlap region of the top and bottom electrodes.
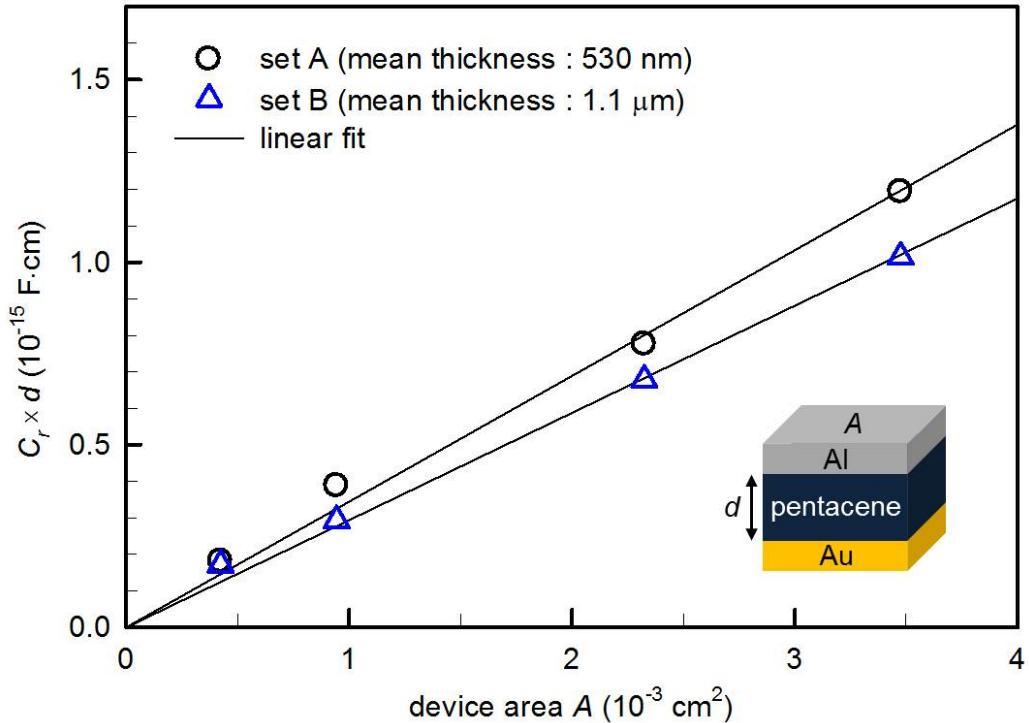
Figure 4.8: Experimental method for estimating quasi-static dielectric constant. The slope of the linear fit corresponds to $k\epsilon_0$ by Equation (4.2). Inset: MIM capacitance with the geometrical dimensions.

4.1.3   Dielectric properties of pentacene

Based on the observation of a purely capacitive behavior in the reverse bias regime, we are able to estimate basic dielectric properties of pentacene films. The measured reverse bias capacitance C_r can be defined by using the parallel-plate capacitor equation

$$C_r = \epsilon_s \frac{A}{d} = k\epsilon_0 \frac{A}{d}, \tag{4.2}$$

where A is the overlap area of the two electrodes, d the semiconductor thickness, and k the dielectric constant. We measured d and C_r of the diodes with different A, in two independently fabricated device sets. In Figure 4.8, measured $C_r \times d$ values are plotted as a function of A with the linear fit trough the origin. Equation (4.2) shows that the slope of this regression line is equal to ϵ_s, from which the dielectric constant k can be calculated. The obtained k is 3.9 ± 0.25 for Set A and 3.3 ± 0.17 for Set B.

The dielectric constant of an organic semiconductor has been often assumed to be around three and many people have used $k = 3$ for theoretical calculations [91–93]. We infer that this value rather corresponds to a high-frequency dielectric constant
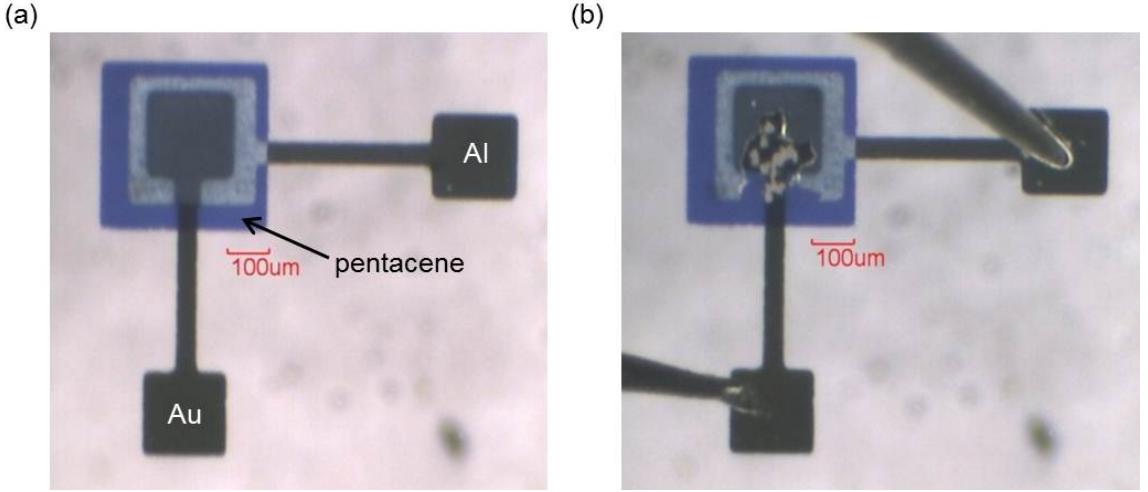
Figure 4.9: Optical microscopical images (a) before and (b) after the breakdown measurement.

estimated within the optical frequency range. Our results show that, in electrical low-frequency regime, the dielectric constant turns out to be higher. When the applied frequency is low, a dielectric medium can respond to the signal with more polarization mechanisms [42], so it is logical to get a higher effective dielectric constant. The difference observed between Set A and Set B might be attributed to the uncontrollable morphological variation of pentacene in each diode. Therefore, we will use the average value of $k = 3.6$ as the quasi-static dielectric constant of pentacene throughout the thesis.

The dielectric strength of an insulating material is quantitatively described by the breakdown field, which is defined as the maximum electric field that can be applied before immediate breakdown [94, 95]. An electrical breakdown generally causes irreversible damages on the material due to abnormally high current through it. Figure 4.9 shows the microscopic images of a pentacene diode under the breakdown test. We measured reverse-regime I-V characteristics and recorded the voltage at which the breakdown occurs. As shown in Figure 4.9(b), the device is irrecoverably damaged after the breakdown measurement is done.

Figure 4.10 shows the measured breakdown field of ten test devices for a statistical result. The average value is calculated to be 1.02 ± 0.06 MV/cm. This value is relatively smaller than that of SiO_2 (8-9 MV/cm) or various polymeric insulators (2-6 MV/cm) [94, 95]. We infer that the polycrystalline nature of pentacene films [96] can result in formation of pin holes and early breakdown. It is known that disordered amorphous phase can exhibit a stronger morphological stability against electrical
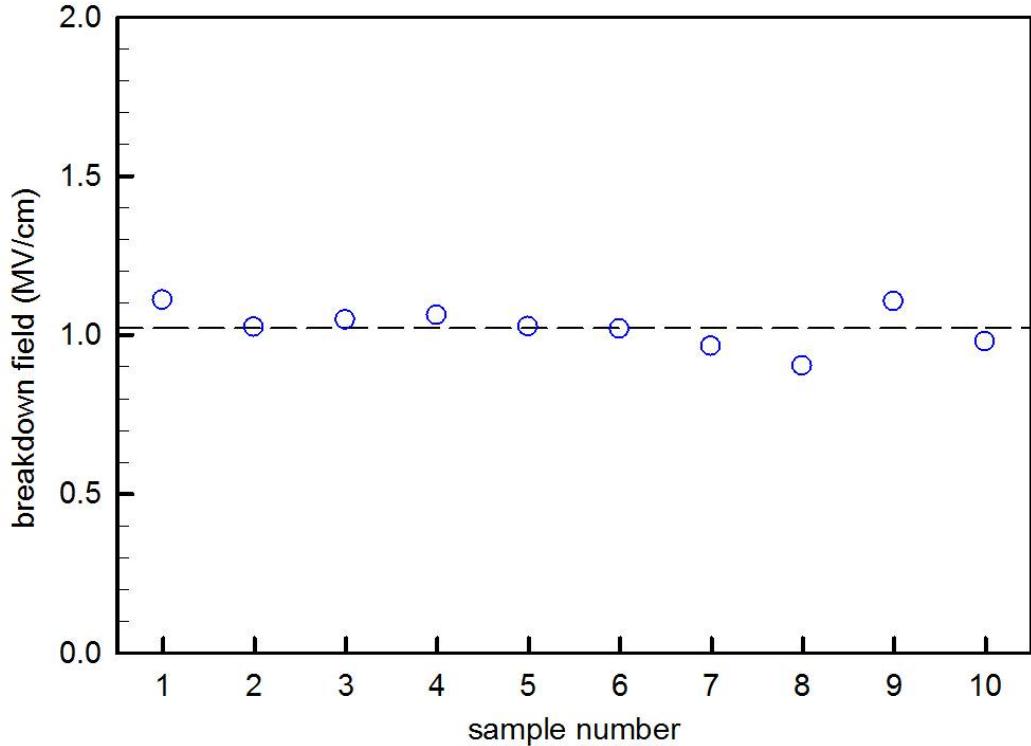
Figure 4.10: Scatter plot of the measured dielectric strength of pentacene. The dashed line shows the average value of the ten devices.

stress [97].

4.1.4   Modeling the low-voltage regime

Because of the absence of a depletion modulation in fully depleted MIM-type organic diodes, a specific model that differs from the Schottky model is to be defined. We revisited the classical theories on metal/insulator junctions that have been intensively dealt with in the early days of solid-state electronics, during which semiconductors have been generally regarded as highly resistive materials that are capable of transporting electrode-injected charge carriers [98, 99].

We start by analyzing electrostatics in an MIM diode at thermal equilibrium. Figure 4.11 shows a schematic diagram of the one-dimensional MIM system to be solved. Here, $x = 0$ is defined at the anode/organic interface and d is the semiconductor thickness. Self-consistent evaluation of Poisson's equation [Equation (4.3)] and the transport equation (drift-diffusion equation) [Equation (4.4)] is conducted for this structure;

$$\frac{\mathrm{d}F}{\mathrm{d}x} = \frac{qp}{\epsilon_s}, \tag{4.3}$$
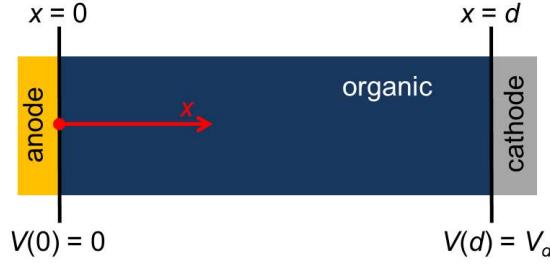
Figure 4.11: Illustration of the one-dimensional coordinate on an MIM diode.

$$J = qp\mu F - qD\frac{\mathrm{d}p}{\mathrm{d}x}, \tag{4.4}$$

where F is the electric field, p the hole concentration, J the net hole current density, μ the hole mobility, and D the hole diffusion coefficient. Note here that, the space-charge term in Equation (4.3) is greatly simplified by assuming hole-only conduction in the absence of thermal carriers; the term p represents the 'injected' holes distributed throughout the semiconductor. It is this assumption that forms the basis for the analytical model development.

These two equations can be merged, with the Einstein relation $D/\mu = k_B T/q$ (k_B is the Boltzmann constant and T is the absolute temperature), into

$$J = \epsilon_s \mu \left(F\frac{\mathrm{d}F}{\mathrm{d}x} - \frac{k_B T}{q}\frac{\mathrm{d}^2 F}{\mathrm{d}x^2} \right). \tag{4.5}$$

At thermal equilibrium, J should be zero, which requires

$$F\frac{\mathrm{d}F}{\mathrm{d}x} - \frac{k_B T}{q}\frac{\mathrm{d}^2 F}{\mathrm{d}x^2}, \tag{4.6}$$

which can be then integrated once giving

$$\left(\frac{q}{2k_B T} \right)^2 F^2 - \frac{q}{2k_B T}\frac{\mathrm{d}F}{\mathrm{d}x} = g^2, \tag{4.7}$$

where g is an integration constant.

In the Boltzmann approximation, Equation (4.8) defines a relationship between the density of holes and the potential:

$$p = p_0 e^{-qV/k_B T}, \tag{4.8}$$

where $p_0 = N_v e^{-E_b/k_B T}$ is the density of holes at $x = 0$. Here, N_v is the effective density of states at the valence band edge and E_b is the anode barrier height at the electrode-semiconductor interface.

Equation (4.7) was first resolved by Mott and Gurney for a semi-infinite semiconductor [98], then by Skinner [100] for a semiconductor of finite thickness. The general solution writes:

$$F(x) = -\frac{2k_BT}{q}g\coth g(x + x_1), \tag{4.9}$$

$$p(x) = \frac{2\epsilon_s k_B T}{q^2}\frac{g^2}{\sinh^2 g(x + x_1)} = p_0\left[\frac{gx_0}{\sinh g(x + x_1)}\right]^2, \tag{4.10}$$

where x_1 is an integration constant, and x_0 the characteristic distribution length:

$$x_0 = \sqrt{\frac{2\epsilon_s k_B T}{q^2 p_0}}. \tag{4.11}$$

Writing that $p(0) = p_0$ leads to:

$$x_1 = \frac{\arg\sinh gx_0}{g}. \tag{4.12}$$

Substitution of Equation (4.12) in Equations (4.9) and (4.10) gives:

$$F(x) = -\frac{2k_BT}{q}g\coth(gx + \arg\sinh gx_0), \tag{4.13}$$

$$p(x) = p_0\left[\frac{gx_0}{\sinh(gx + \arg\sinh gx_0)}\right]^2. \tag{4.14}$$

The potential is obtained by integrating the electric field:

$$V(x) = -\int_0^x F(x)\mathrm{d}x = \frac{2k_BT}{q}\ln\frac{\sinh(gx + \arg\sinh gx_0)}{gx_0}. \tag{4.15}$$

Here, we assumed that $V = 0$ at the anode. The integration constant g can now be estimated by introducing the boundary condition $V(d) = V_d$, that equals the difference between the work functions of the anode and the cathode.

The results in Equations (4.13) to (4.15) accurately describe the electrostatic distribution in the model diode in Figure 4.11. At this stage, however, the calculation can no longer be performed by analysis and a numerical computation is necessary. Figure 4.12 shows the model-calculated potential profiles with different E_b values. The fixed parameters are $d = 200$ nm, $\epsilon_s = 3.6 \times \epsilon_0$, $N_v = 10^{20}$ cm^{-3}, $T = 300$ K, and $V_d = 0.6$ V. We can justify the MIM diagram (Figure 4.5) with this result; as along as a substantial injection barrier exists at the injecting contact, the potential profile is linear and the electric field is constant throughout the whole semiconductor thickness. It should be note that, in most realistic metal/organic junctions, a Fermi-level pinning occurs to limit the minimum barrier height not less than ~ 0.3 eV [58,63],
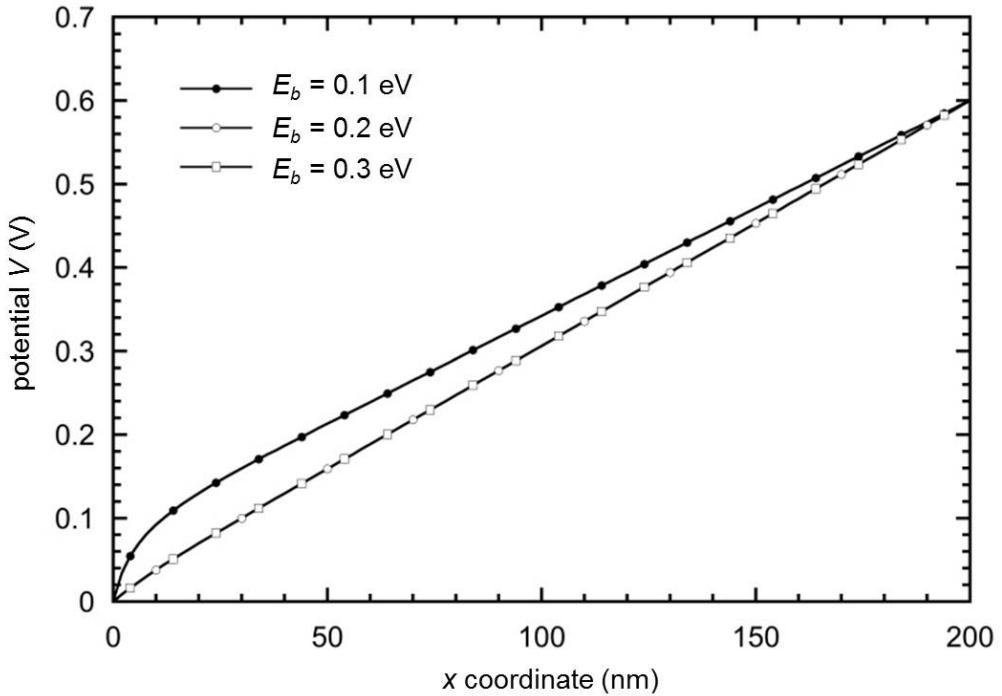
Figure 4.12: Potential profiles along the semiconductor thickness calculated by the model Equation (4.15). The profiles are practically straight as long as the injection barrier is not too small.

which supports the applicability of the MIM model. On the other hand, the reason of a slight band bending with $E_b = 0.1$ eV is that an accumulation layer forms near $x = 0$ due to a vanishing barrier, which in turn tends to obstruct further injection from the electrode by large opposing electric field (space-charge effect).

For predicting current-voltage characteristics, Equation (4.5) needs to be solved under out-of-equilibrium condition ($J \neq 0$). The calculation tends to be complicated but the exact solution was already given by Skinner and Wright [101, 102]. Their solution, however, includes Bessel functions that do not lead to easy-to-handle analytical expressions. Here, we propose a simplified analytical model for the low-voltage regime, which is of special interest for OPVs that operate below the open-circuit voltage [16, 103].

Figure 4.13 illustrates the energy diagram under a small forward-bias. The anode current J_{an} should be diffusion-dominated because the injected carriers are many but the internal electric field points against their drift toward the cathode. The number of anode holes that can overcome the barrier $q(V_d - V_a)$ increases by applying V_a.
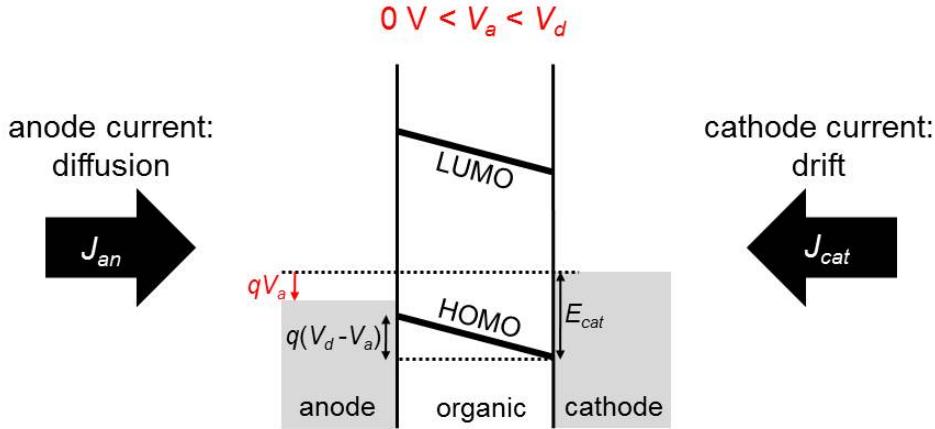
Figure 4.13: Energy diagram of an MIM organic diode under small forward-bias V_a. An analytical current-voltage model is developed here by only considering the dominant current mechanism at each contact side; diffusion current from the anode ant drift current from the cathode.

Hence, J_{an} is proportional to $e^{-q(V_d - V_a)/k_B T} \propto e^{V_a/k_B T}$, and we write as

$$J_{an} = J_{an0} e^{qV_a/k_B T}, \qquad (4.16)$$

where J_{an0} is the anode current at $V_a = 0$ V. The cathode current J_{cat}, on the other hand, is drift-dominated because the electric field favorably sweeps the holes injected from the cathode even though their concentration is low. By using p_{cat} as the injected hole concentration from the cathode and $(V_d - V_a)/d$ as the electric field strength,

$$J_{cat} = q p_{cat} \mu \frac{V_d - V_a}{d} = q N_v e^{-E_{cat}/k_B T} \mu \frac{V_d - V_a}{d}, \qquad (4.17)$$

where the last expression shows the explicit role of the cathode barrier E_{cat}. At thermal equilibrium, the net current should be zero,

$$J_{an}(V_a = 0) = J_{cat}(V_a = 0), \qquad (4.18)$$

and this condition requires

$$J_{an0} = q N_v e^{-E_{cat}/k_B T} \mu \frac{V_d}{d}. \qquad (4.19)$$

Now we can write the final net current model as

$$
\begin{aligned}
J &= J_{an} - J_{cat} \\
&= q N_v e^{-E_{cat}/k_B T} \mu \frac{V_d}{d} \left(e^{qV_a/k_B T} - 1 + \frac{V_a}{V_d} \right) = J_s \left(e^{qV_a/k_B T} - 1 + \frac{V_a}{V_d} \right), \quad (4.20)
\end{aligned}
$$
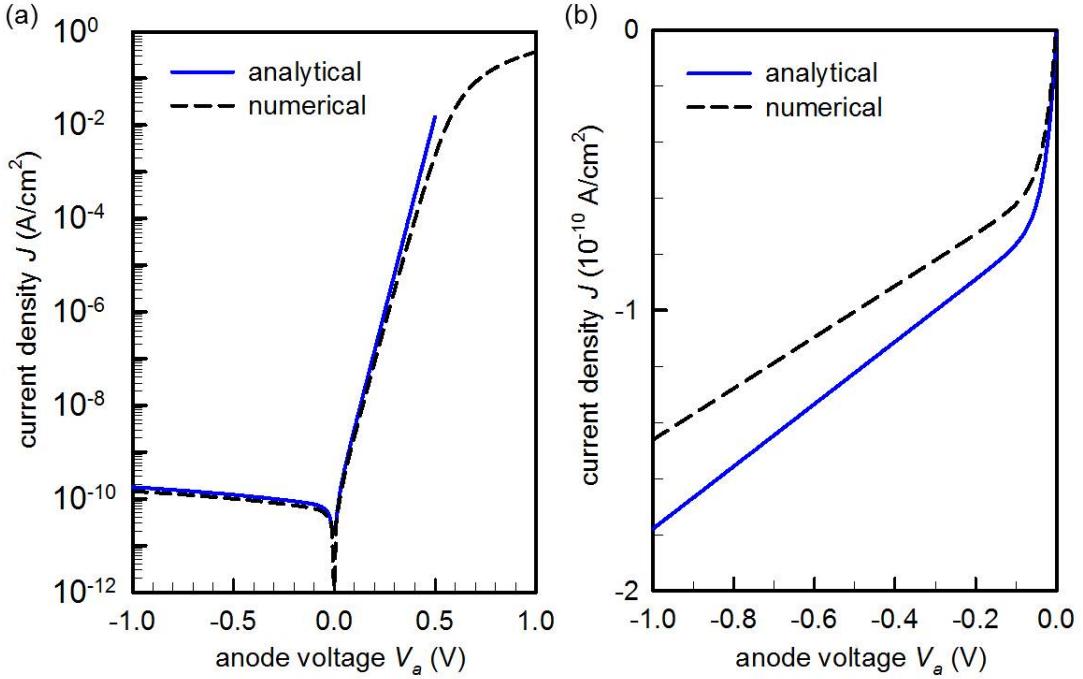
Figure 4.14: Current voltage characteristics for comparing the analytical model with the numerical finite-element simulation. (a) From reverse- to injection-limited regime in semi-log scale. (b) Reverse-bias regime in linear scale.

where J_s is the saturation current. Note that the model Equation (4.20) is a compact, fully analytical description with physcally-based parameters, which is an important requirement for practical circuit simulation. Also note that the current level is very sensitive to the barrier at the blocking contact E_{cat}, which only permits low-level injection. This operation mechanism strongly reminds that of the conventional p-n junction, in which the current is controlled by minority carriers [21]. In addition to a different definition of J_s, a major difference from the Schottky model is the V_a-dependence of the reverse-bias current, which manifests itself by the third factor in the brackets in Equation (4.20). When the applied forward-bias is larger than a few $k_B T/q$, Equation (4.20) simply approximates to

$$J = J_s e^{qV_a/k_B T}. \tag{4.21}$$

Figure 4.14 shows the validity of the analytical model in comparison to the numerical simulation by ATLAS. Both calculations were conducted with the physical parameters summarized in Table 4.1. As shown in Figure 4.14(a), the analytical model is in excellent agreement with the numerical one as long as we remain in the

Table 4.1: Physical parameters for the analytical calculation and numerical simulation in Figure 4.14.

Parameter	Value
Temperature	300 K
Effective DOS	10^{20} cm^{-3}
Dielectric constant	3.6
Doping concentration	0 cm^{-3}
Semiconductor thickness	200 nm
Ionization potential	5.1 eV
Hole mobility	0.15 cm^2/V·s
Anode work function	4.8 eV
Cathode work function	4.2 eV

low-voltage regime, which justifies the assumptions made above for analytical development. The numerical curve also shows a decline of the slope when V_a exceeds V_d, because the current in this regime starts to be limited by the bulk conductivity. The reverse-bias regime shown in Figure 4.14(b) clearly indicates that the current at negative V_a is not constant, which is correctly predicted by Equation (4.20).

All analytical results up to this point are strongly based on the primary assumption that the organic semiconductor is undoped, so that only injected charges govern the current flow in the diode. In order to solidify this hypothesis, a series of simulations with increasing doping concentration has been conducted. Figure 4.15 shows the forward $J - V$ characteristics from zero to heavily-doped case. Obviously, doping up to 10^{14} cm^{-3} does not influence the current because the injected carriers are more abundant. It is only when the doping concentration becomes higher than 10^{16} cm^{-3} that the current significantly raises owing to additional free carriers. Accordingly, the organic semiconductor can be safely described as undoped in realistic cases even though small amounts of unintentional dopants could exist.

4.1.5   Trap-induced ideality factor

The effect of charge-trapping states on the electrostatic distribution is discussed and its impact on the diode current will be elucidated. Small molecular semiconductors generally exhibit exponential trap DOS of which the origins are attributed to various chemical and structural imperfections [104–106]. The trap DOS $N(E)$ is written as

$$N(E) = \frac{N_t}{k_B T_c} e^{-(E-E_v)/k_B T_c},\tag{4.22}$$

where E_v is the energy of the valence band edge, N_t the total density of traps, and T_c the trap characteristic temperature corresponding to the distribution width. The
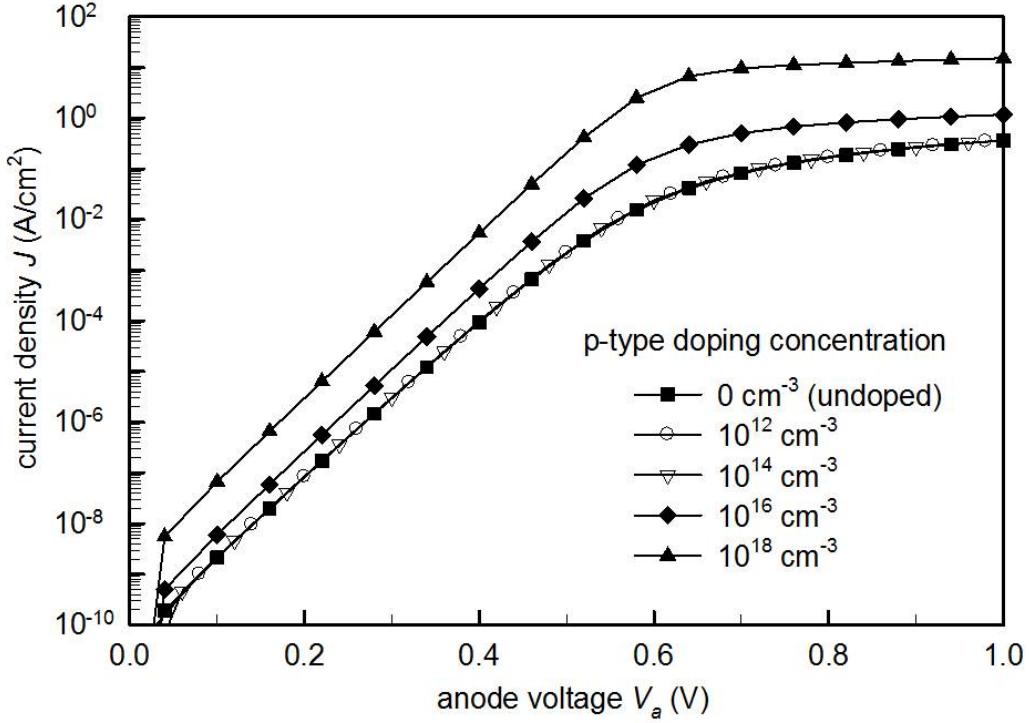
Figure 4.15: Numerical simulation with a variation of the doping concentration in the organic semiconductor. This result shows that the effect of doping on the current does not appear as long as a moderate doping is concerned and the assumption of zero doping is usable for analytical simplicity.

density of trapped holes p_t is estimated by integrating this DOS times the Fermi-Dirac distribution over the available energy range,

$$p_t(E_F) = \int_{-\infty}^{+\infty} \frac{N(E)\mathrm{d}E}{1 + e^{-(E-E_F+qV)/k_BT}}. \tag{4.23}$$

Because $T_c > T$ in general, the DOS in Equation (4.22) is a slowly varying function with E compared to the Fermi function, so that the latter can be approximated to a step function. This assumption yields

$$p_t = p_{t0}e^{-qV/k_BT_c}, \tag{4.24}$$

with $p_{t0} = N_t e^{-E_b/k_BT_c}$ is the boundary value of p_t at $x = 0$. From Equations (4.8) and (4.24), the ratio between free and trapped holes is given by

$$\frac{p}{N_v} = \left(\frac{p_t}{N_t}\right)^{T_c/T}. \tag{4.25}$$

The potential profile can now be calculated by replacing p by $p + p_t$ in Poisson's equation (4.3). However, generally $p_t \gg p$, so that a valid equation can be simply
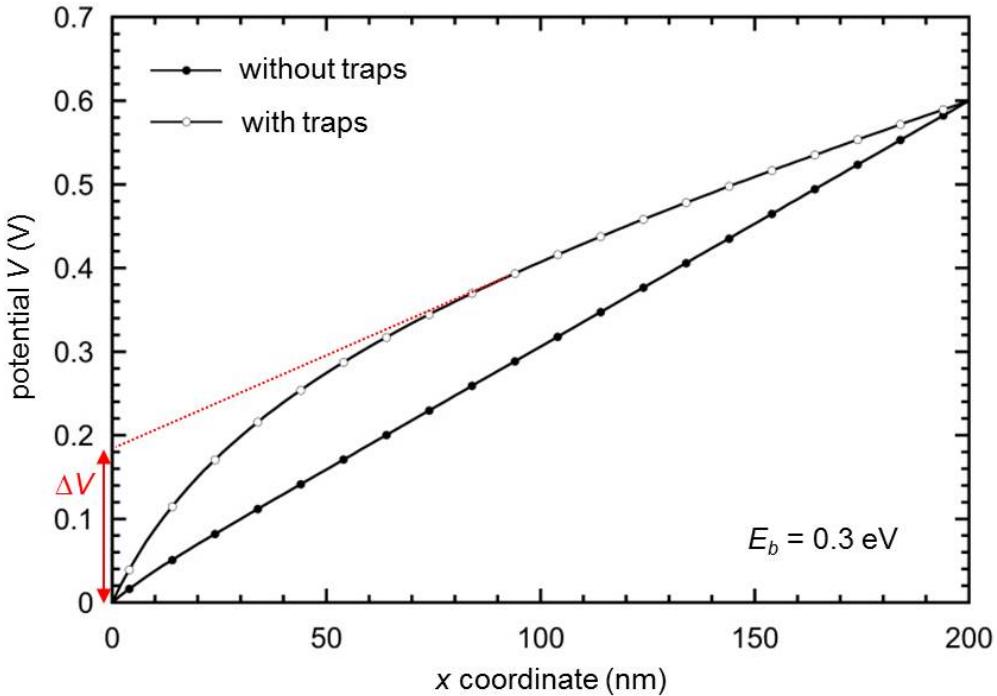
Figure 4.16: Semi-analytical estimation of the potential profiles with and without trap states. ΔV denotes the barrier reduction for the holes diffusing from the anode toward the cathode.

obtained by replacing p by p_t in Equation (4.3). On the other hand, drift-diffusion equation must be left unchanged because only free carriers can participate in the charge transport. Making use of Equations (4.3) and (4.25), Equation (4.5) is modified as

$$J = qN_v\mu \left(\frac{\epsilon_s}{qN_t}\right)^l \left(\frac{\mathrm{d}F}{\mathrm{d}x}\right)^{l-1} \left(F\frac{\mathrm{d}F}{\mathrm{d}x} - \frac{k_BT_c}{q}\frac{\mathrm{d}^2F}{\mathrm{d}x^2}\right), \qquad (4.26)$$

where $l = T_c/T$. At thermal equilibrium, Equation (4.26) reduces to Equation (4.6) with T_c instead of T. Accordingly, the solution for $V(x)$ is obtained by changing T to T_c and p_0 to p_{t0}. Figure 4.16 shows the effect of traps on the potential profile in the model diode. The parameters are those used for the calculation in Figure 4.12 with fixed $E_b = 0.3$ eV. For the potential 'with traps' we used $N_t = 2 \times 10^{18}$ cm^{-3} and $T_c = 1200$ K. Note that, in the presence of traps, a band bending similar to a low-barrier profile in Figure 4.12 occurs. This is because, even with a high E_b of 0.3 eV, the trap DOS provides available states near the Fermi level of the anode, which in turn leads to the formation of an accumulated space-charge region. This effect is, in other words, a barrier lowering effect by trap DOS as denoted by the barrier reduction ΔV in Figure 4.16.
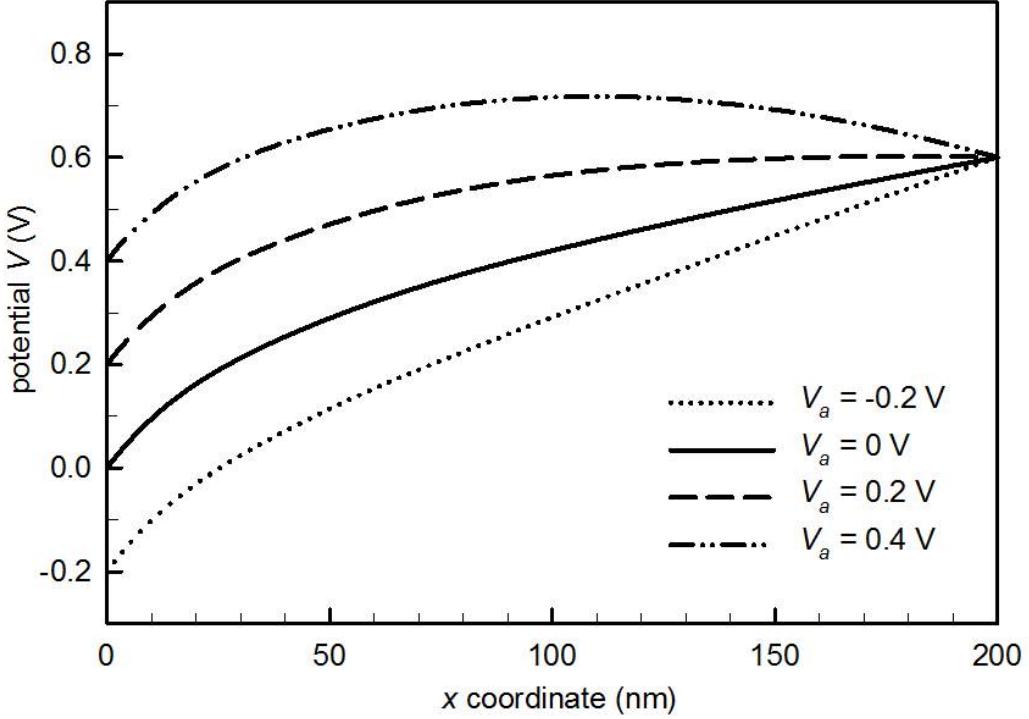
Figure 4.17: Potential profiles obtained by the numerical simulation under different bias conditions. The variation of the effective ΔV is the evidence for the trap-induced ideality factor in the low-voltage regime.

In order to understand the effect of traps on the diode current, we conducted numerical simulation (ATLAS) with an inclusion of the exponential trap DOS model. Figure 4.17 shows the variation of potential profiles with increasing V_a. This result indicates that ΔV tends to increase with V_a. Now we see that the forward-bias current is no longer proportional to e^{qV_a/k_BT}, but rather to $e^{q(V_a-\Delta V)/k_BT}$. If we take a first order approximation of the dependence of ΔV on V_a as $\Delta V \simeq \alpha V_a$, the diode current with traps becomes

$$J = J_s e^{q(1-\alpha)V_a/k_BT} = J_s e^{qV_a/nk_BT} \tag{4.27}$$

under a forward bias higher than a few k_BT/q. It means that the ideality factor n, which corresponds to the deviation of the exponential slope of a J-V curve, is well expected by the trap states that change the electrostatic distribution.

Current-voltage characteristics calculated by ATLAS in Figure 4.18 confirms this argument. At first, it is shown that the effect of traps is not significant in the reverse-bias regime. In the injection-limited forward regime, however, the traps decrease the slope of the J-V curve. We also realize that as T_c increases, the slope further decreases due to the increased number of trapped charges, which in turn increases α and n.
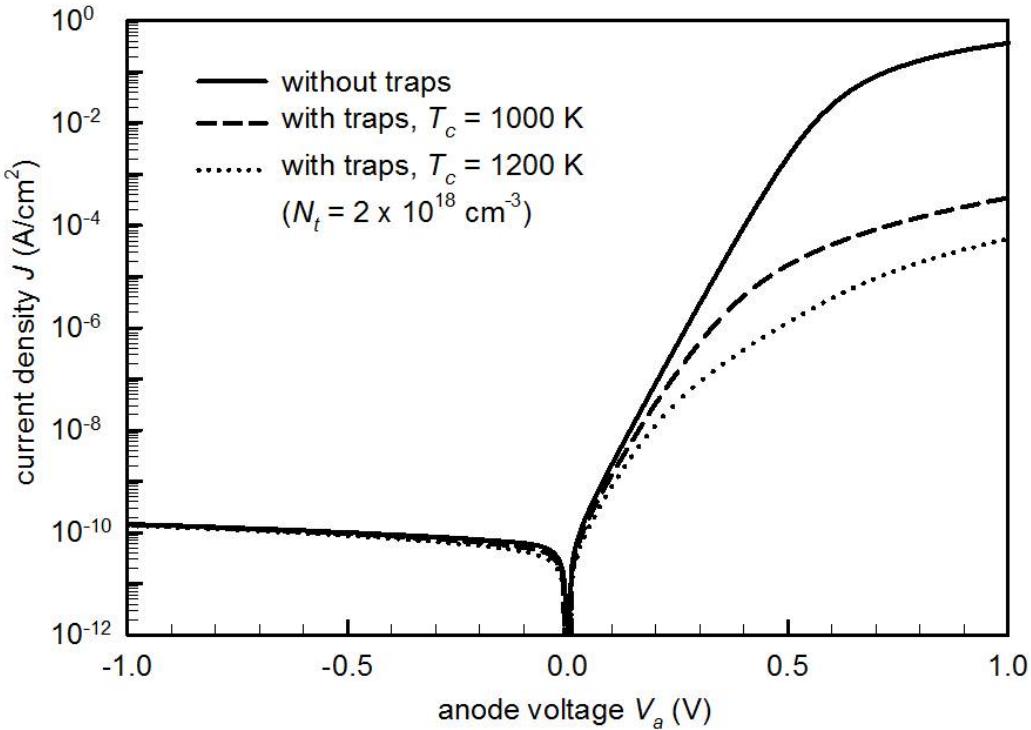
Figure 4.18: Numerical simulation showing the effect of exponential trap DOS on the current of an organic diode. The traps result in a deviation of the forward current in the exponential regime, which is interpreted in terms of the ideality factor n. Ideality factor increases with increasing T_c.

Note that Equation (4.27) based on the first order approximation is not sufficient when T_c is too high; the $T_c = 1200$ K curve in Figure 4.18 does not have perfectly straight exponential slope. In this case, a constant n value cannot be defined.

It is clear that the traps also significantly affect the bulk-limited-regime current; we see the decrease of the current level at $V_a = 1$ V in Figure 4.18. The trap-limited SCLC with exponential DOS was modeled by Mark and Helfrich in [52]. We refer to this classical model to examine the trap parameters in the fabricated devices. The Mark-Helfrich model can be written in the form of

$$J = qN_v\mu \left(\frac{\epsilon_s}{qN_t} \frac{l}{l+1} \right)^l \left(\frac{2l+1}{l+1} \right)^{l+1} \frac{(V_a - V_d)^{l+1}}{d^{2l+1}}, \tag{4.28}$$

where $(V_a - V_d)$ is used to compensate the built-in electric field due to the asymmetric contact geometry. The slope of the measured J-V curve on a log-log plot in Figure 4.19 is 5.4, which shows that the bulk-current in the fabricated pentacene diode is strongly trap-limited. The diode measured here has the Au/pentacene/Al structure with d of 200 nm and the active area of 4.0×10^{-4} cm^2. The extracted slope corresponds to
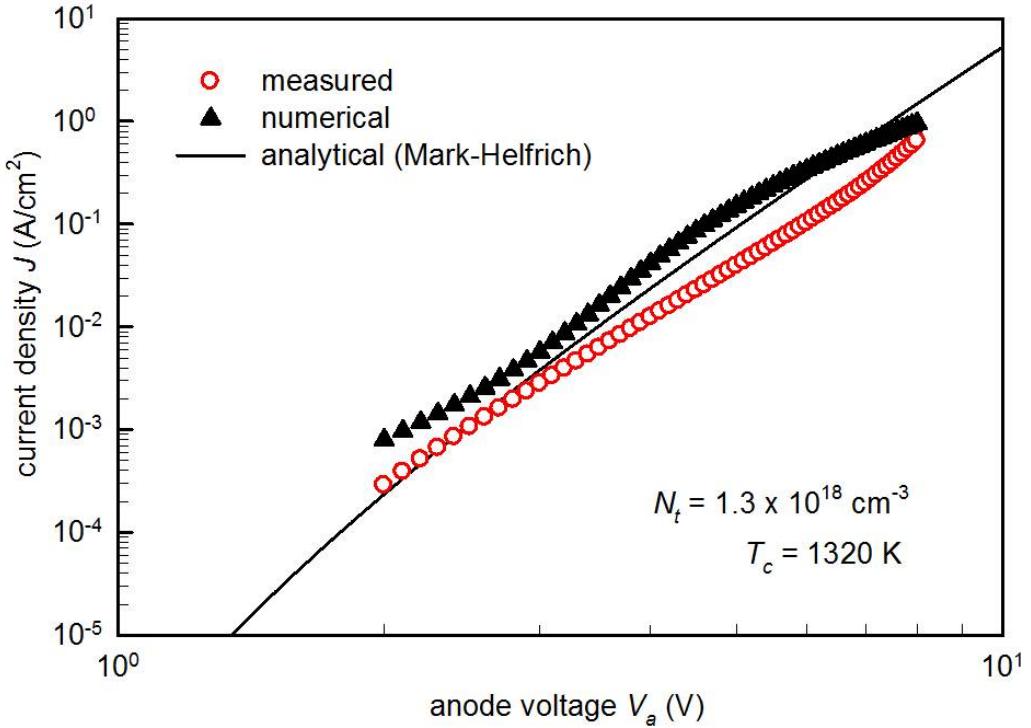
Figure 4.19: Experimental current-voltage curve in the bulk-limited regime drawn on a log-log plot. The measured current is compared to the Mark-Helfrich model and the ATALS simulation.

$l = 4.4$ and $T_c = 1320$ K. Then, we inserted this T_c value in the numerical model and optimized simulated J-V characteristics to approach the measured one for estimating N_t. This process led to the optimized numerical curve in Figure 4.19 with $N_t = 1.3 \times 10^{18}$ cm^{-3}. As a confirmation, these obtained N_t and T_c are put into the Mark-Helfrich model Equation (4.28) and the analytical curve in Figure 4.19 corresponds to this calculation.

Finally, we were able to very accurately model the measured low-voltage current-voltage curve by using the extracted trap parameters. As the low-voltage current is dominated by the blocking contact, we adjusted the cathode (Al) work function in the simulator with an assumed ionization potential of pentacene and an anode (Au) work function. Figure 4.20 shows an excellent agreement between the measurement and the optimized numerical simulation. The final physical parameters for the pentacene diode are summarized in Table 4.2. Note that the most critical factor for fitting the low-voltage regime was the cathode barrier, which turns out to be $5.2 - 4.38 = 0.82$ eV. The foremost result is that the ideality factor in the real device, here $n = 2.1$, was exactly reproduced by taking into account exponential trap DOS, with the trap
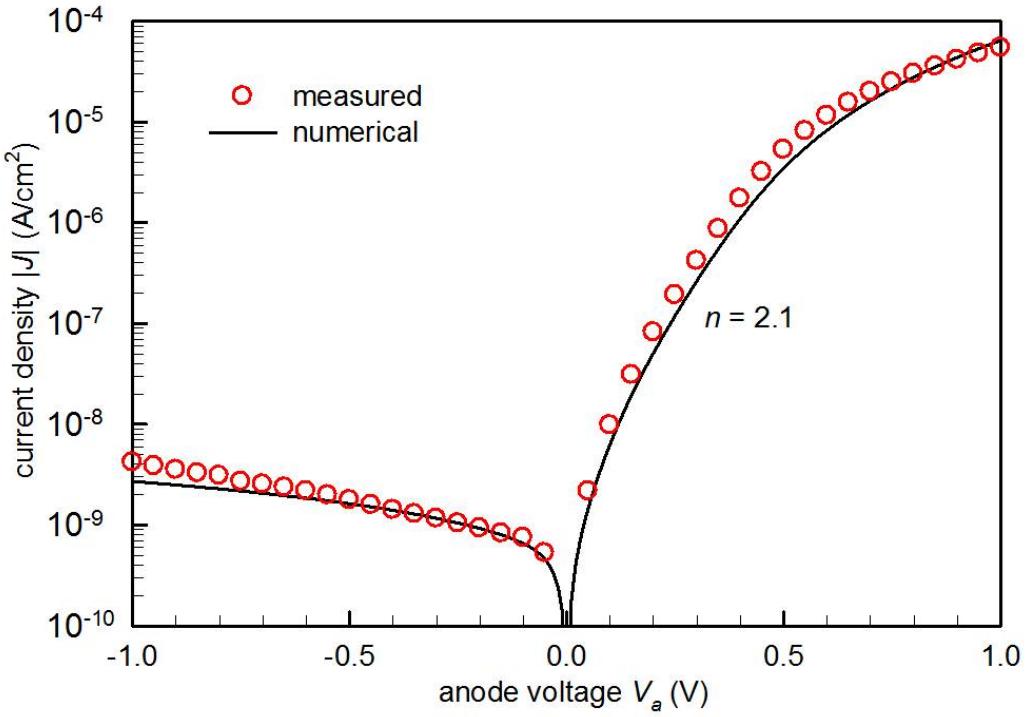
Figure 4.20: Final comparison of the low-voltage regime current of a fabricated pentacene diode with the best-fit numerical model with the systematically estimated parameters.

Table 4.2: Physical parameters used for the numerical simulation that produces the best-fit curve to the experimental current-voltage characteristics of the pentacene diode in Figure 4.20.

Parameter	Value
Temperature K	300 K
Effective DOS N_v	10^{20} cm^{-3}
Dielectric constant k	3.6
Doping concentration	0 cm^{-3}
Pentacene thickness d	200 nm
Ionization potential	5.2 eV
Hole mobility μ	0.15 cm^2/V·s
Total trap density N_t	1.3×10^{18} cm^{-3}
Trap characteristic temperature T_c	1320 K
Anode (Au) work function	4.9 eV
Cathode (Al) work function	4.38 eV

parameters accurately estimated from the same device in the high-voltage regime.

4.2   Vertical symmetrical diodes

This section deals with data from a collaboration with the group of Prof. Jacek Ulanski at the Department of Molecular Physics, Technical University of Lodz, Poland. The device fabrication and measurement were conducted in Poland and we received the data and analyzed them for equivalent circuit modeling.

We name the device vertical 'symmetrical' diode because of the similarity of the two contact metals. However, actual devices do not always exhibit perfectly symmetrical current-voltage characteristics. It is because the order in which the metal and the organic material are deposited can influence the energetic of the junction even with the same material combination [89]. A major reason for this is the softness of organic materials. In general, a metal deposited on top of an organic film is prone to slightly penetrate into the molecular matrix, forming a less sharp metallurgical interface compared to that of an organic-on-top-of-metal interface [107]. Work function shift of the metal due to contamination before depositing an organic layer can be another reason for energetic asymmetry [108]. If those effects are minimized, a vertical symmetrical diode can have fairly symmetrical *I-V* characteristics.

Here, a vertical metal/organic/metal diode with Au/P3HT/Au structure is analyzed to study their impedance characteristics under light exposure and during time relaxation.

4.2.1   Film and device properties

Figure 4.21 shows the measured absorption spectrum of a deposited P3HT film. As well known from the literature, the P3HT layer absorbs a large portion of the visible photons (roughly from 400 nm to 700 nm) [109, 110]. Making use of this broad absorption spectrum, Antognazza and co-workers have demonstrated selective color sensors based on P3HT photodiodes [111]. By estimating the wavelength at the absorption edge in Figure 4.21 (645 nm), we calculate the optical bandgap of P3HT. The resulting optical bandgap is 1.9 eV, in good agreement with the literature [103].

Current-voltage measurements on a Au/P3HT/Au device were conducted under two different atmospheric conditions; low vacuum (2×10^{-2} mbar) and ambient air. The *I-V* characteristics are shown in Figure 4.22. The voltage is applied to the bottom electrode with the top electrode grounded. We first see good symmetry in the *I-V* curves in both cases, which indicates that the top and bottom Au/P3HT interfaces are
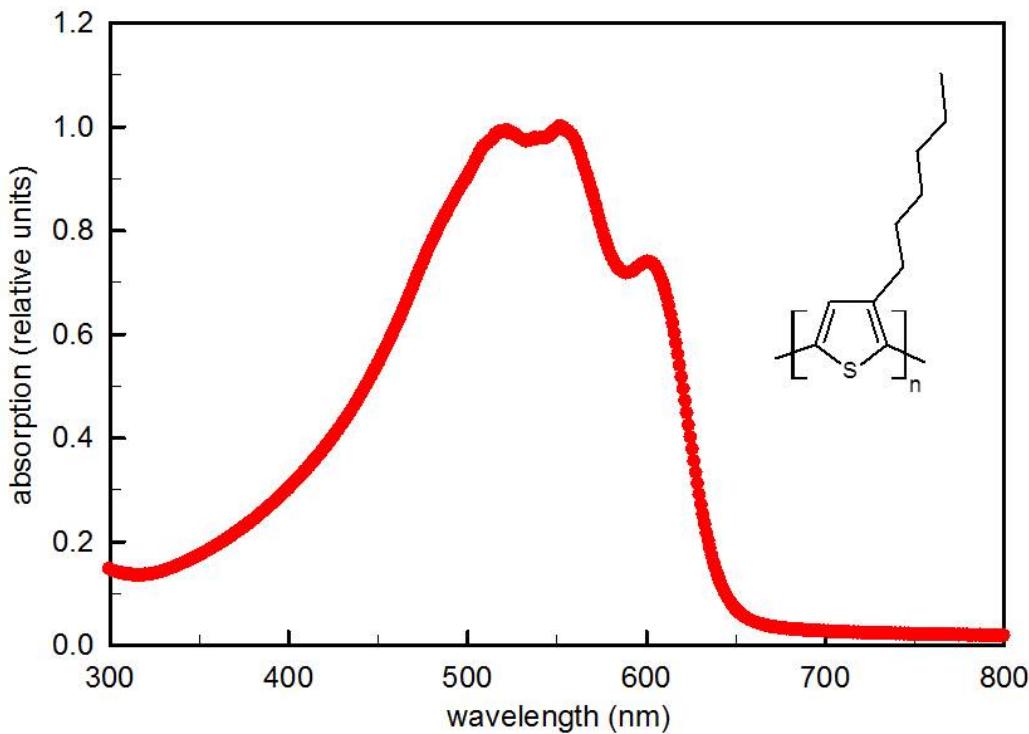
Figure 4.21: Abosrption spectrum of a P3HT film. Inset: molecular structure of P3HT.

practically equivalent. Also note that the *I-V* characteristics are straight. It implies that the carrier injection barrier from the Au Fermi level to the P3HT HOMO level is negligible, and the contact resistance is much smaller than the bulk resistance. When a substantial injection barrier exists, the current is expected to follow an exponential increase, which is revealed by a bended *I-V* curve at low voltage.

An important finding is that the current increases significantly under ambient air. For both curves, we conducted linear regression through the origin and the fitted lines are shown together with the measured data. The slope corresponds to the ohmic conductivity and the extracted values are 3.9 μS for the vacuum data and 8.6 μS for the ambient-air data; the conductivity is enhanced by a factor of 2.2 under exposure to the ambient air. This phenomenon is attributed to oxygen doping [90, 112]; oxygen molecules can be adsorbed and diffuse into the organic solid and they can serve as efficient p-type dopants (acceptors) by redox reaction via their molecular orbitals. The enhanced ohmic contact is then regarded as a concomitant event. Even though it seems marginal, an energy mismatch between the Fermi levels of Au and P3HT could lead to the formation of a depletion region. Higher carrier density is expected when ambient doping takes place and these additional carriers could reduce the depletion
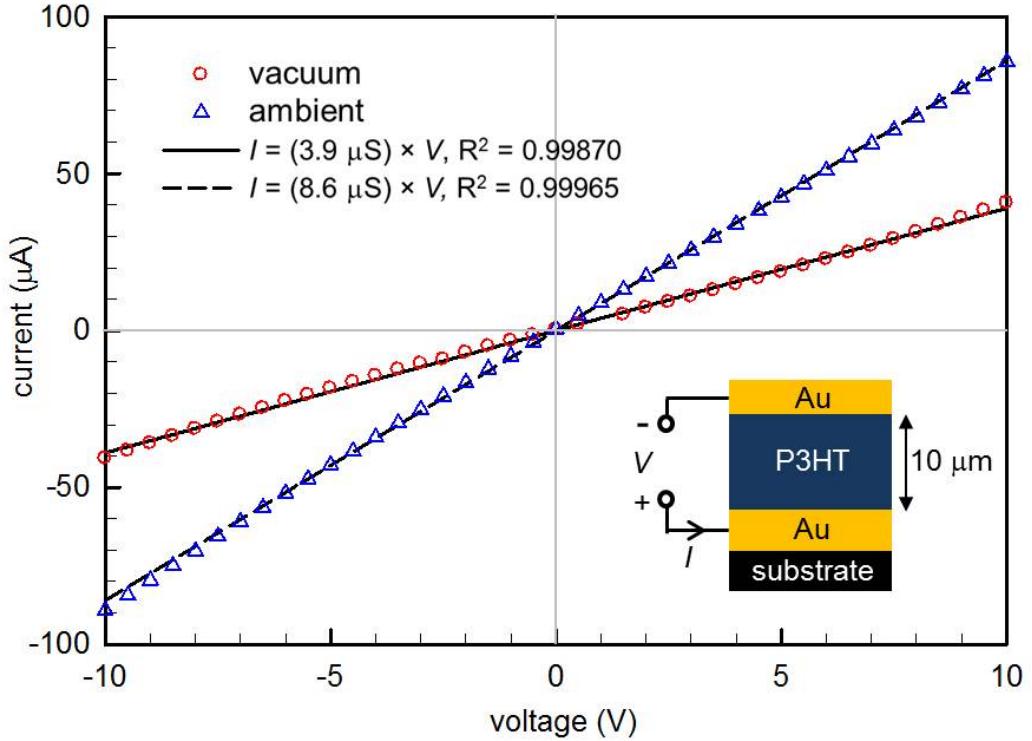
Figure 4.22: Current-voltage characteristics of a vertical Au/P3HT/Au diode under low vacuum and ambient air. Inset: device structure.

width down to a negligible scale and/or compensate other interface-related parasitic (non-ohmic) effects.

4.2.2 Equivalent circuit model

In order to understand the effect of light exposure on the impedance characteristics of the Au/P3HT/Au device, a series of broad-range impedance spectroscopy experiments were conducted (10^{-2} to 10^7 Hz). To focus on the natural relaxation behavior after illuminating the sample, dc bias was kept at 0 V. Figure 4.23 shows the impedance spectroscopy data on a complex plane (Nyquist diagram). Upon light exposure, the device responded quickly and came to the state in which the overall impedance modulus is strongly reduced compared to the initial state. At this point, it is worth reminding that an impedance modulus corresponds to the distance from the origin to each measurement point on a complex plane. Surprisingly, this excited state does not immediately recover towards its initial state after turning off the light. Instead, it took several hours for the system to recover as monitored by repeated measurements. It turned out that, in spite of this extraordinarily slow relaxation, the device could fully relax to its initial state so that the excitation/relaxation process
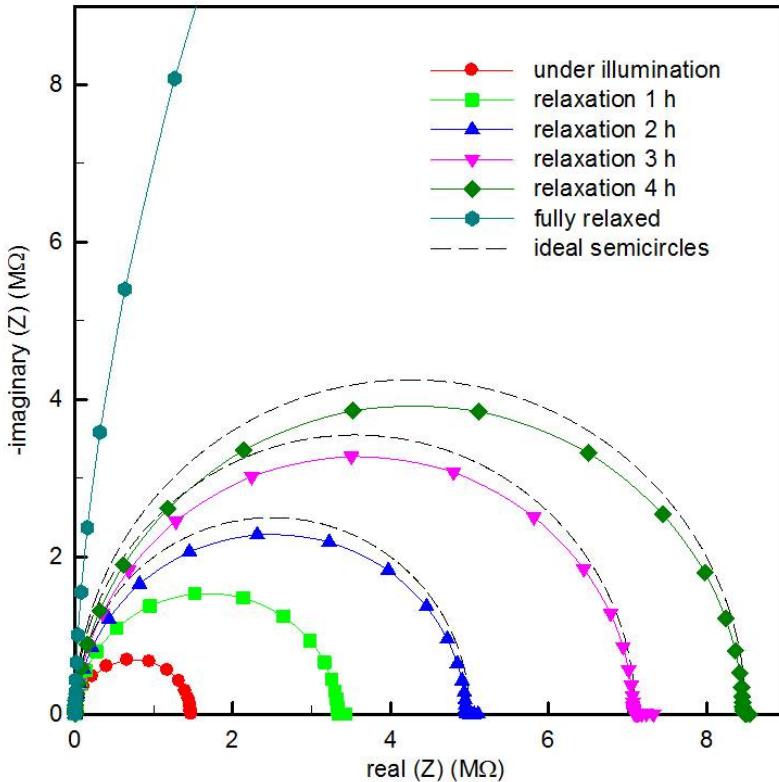
Figure 4.23: Nyquist diagram for the frequency-dependent impedance data under light exposure and relaxation. The applied dc voltage is 0 V and the amplitude of small-signal (ac) voltage is 0.01 V. Frequency range is from 10^{-2} to 10^7 Hz. Three ideal semicircles are drawn to help recognize the non-ideality of the data curves; the height of an experimental arc is smaller than the half-width.

is considered to be reversible. Note that because we focus on the 'relaxation' process, Figure 4.23 is not scaled with an entire feature of the fully relaxed state. The impedance modulus of the unexposed state is much higher than that of the illuminated state. The trajectory of the 'fully relaxed' data extends very far out of the region shown, intercepting the real axis at 91 MΩ.

When the shapes of the measured data curves in Figure 4.23 are compared to the ideal semicircles with the same width drawn together, we realize that they are not perfectly matched. This implies that a simple parallel RC circuit is not sufficient to model the measured frequency response of the P3HT diode. We found that such depressed circular arcs can be appropriately modeled by replacing the normal capacitor by a constant-phase element (CPE) [113]. The impedance of a CPE (Z_Q) is defined by

$$Z_Q = \frac{1}{(j\omega)^\alpha Q}. \tag{4.29}$$

Here α is a characteristic exponent that indicates the degree of imperfection of the capacitive element ($0 < \alpha \leq 1$). The value α equally determines the phase shift by a CPE that is independent of ω. The phase shift can be between 0 and $-\frac{\pi}{2}$ rad. By definition, Q has a unit of $F \cdot s^{\alpha-1}$. Its meaning will be further discussed below.

The total impedance of a parallel resistance-CPE circuit (RQ circuit) is denoted as Z_{RQ}. The combination rule is used for deducing Z_{RQ} and its real part $[\mathrm{Re}(Z_{RQ})]$ and imaginary part $[\mathrm{Im}(Z_{RQ})]$ can be expressed as

$$Z_{RQ} = \frac{1}{1/Z_R + 1/Z_Q} = \frac{R}{1 + (j\omega)^\alpha RQ}, \tag{4.30}$$

$$\mathrm{Re}(Z_{RQ}) = \frac{R[1 + \omega^\alpha RQ \cos(\frac{\alpha\pi}{2})]}{1 + 2\omega^\alpha RQ \cos(\frac{\alpha\pi}{2}) + \omega^{2\alpha} R^2 Q^2}, \tag{4.31}$$

$$\mathrm{Im}(Z_{RQ}) = -\frac{\omega^\alpha R^2 Q \sin(\frac{\alpha\pi}{2})}{1 + 2\omega^\alpha RQ \cos(\frac{\alpha\pi}{2}) + \omega^{2\alpha} R^2 Q^2}. \tag{4.32}$$

Note here that when $\alpha = 1$, a CPE reduces back to a normal capacitance. However, with $\alpha \neq 1$, Equations (4.31) and (4.32) show that the complex-plane representation of Z_{RQ} results in a depressed semicircle. We took the data curve 'under illumination' from Figure 4.23 and fitted them to both RC and RQ circuits to see the difference. As shown in Figure 4.24, the RQ circuit nicely fits the impedance data. The extracted α is 0.96. In the literature, a CPE is generally interpreted in terms of a non-ideal capacitance. Physical arguments for CPE comprise distribution of energy states, spatially distributed conductivity, dispersive (frequency-dependent) dielectric property, and so on [73, 114]. We infer that the observation of a CPE in our P3HT diode is due to the inhomogeneous contact interfaces between the rough polymer surface and the metal.

Additionally, we define the characteristic frequency of an RQ circuit (ω_{RQ} or f_{RQ}) in a similar way to that used for the RC circuit, which corresponds to the highest point on a data curve,

$$\left.\frac{d\mathrm{Im}(Z_{RQ})}{d\omega}\right|_{\omega=\omega_{RQ}} = 0 \text{ with } \omega_{RQ} = 2\pi f_{RQ} = \frac{1}{(RQ)^{\frac{1}{\alpha}}}. \tag{4.33}$$

Note that ω_{RQ} is uniquely determined by the three circuit parameters R, Q, and α.

4.2.3 Circuit parameters during relaxation

It is found that all measured data over the relaxation period are also well fitted by the RQ circuit. The extracted circuit parameters α, R, and Q are to be compared
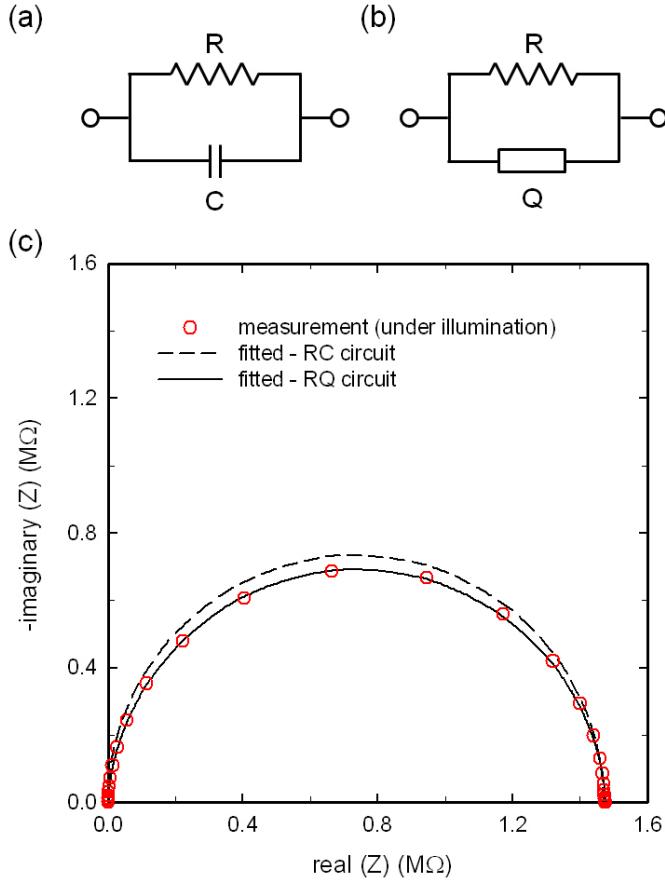
Figure 4.24: (a) Parallel resistance and capacitance circuit (RC circuit). (b) Parallel resistance and CPE (constant-phase element) circuit (RQ circuit). (c) Fitted experimental data to both RC and RQ equivalent circuits.

to understand their variation upon photoexcitation and relaxation. However, the parameter Q has a unit of $F \cdot s^{\alpha-1}$, which is α-dependent. It makes difficult to argue over changing Q values if its unit changes as well. One strategy to transcend this limitation, is to focus on the response of the P3HT diode at the characteristic frequency ω_{RQ}. We can define an effective capacitance C_{eff} that has a unit of an ordinary capacitance. The definition is done by finding an equivalent RC circuit that features the same characteristic frequency as that of the RQ circuit. This is expressed as

$$\omega_{RQ} = \frac{1}{(RQ)^{\frac{1}{\alpha}}} = \frac{1}{RC_{\text{eff}}}, \tag{4.34}$$

which readily gives C_{eff} as

$$C_{\text{eff}} = R^{\frac{1}{\alpha}-1} Q^{\frac{1}{\alpha}}. \tag{4.35}$$

Table 4.3: Summary of the circuit parameters during relaxation

State	α	R [MΩ]	Q [pF $\cdot$ s$^{\alpha-1}$]	C_{eff} [pF]
Illuminated	0.96	1.5	340	250
1h relaxed	0.94	3.4	380	260
2h relaxed	0.95	5.0	370	260
3h relaxed	0.95	7.1	360	260
4h relaxed	0.95	8.5	350	260
Fully relaxed	0.96	91	290	250

Note that C_{eff} is uniquely determined by a combination of α, R, and Q. It is considered that C_{eff} is a parameter that keeps any non-ideal capacitive characteristics of the RQ system and enables practical analysis in the capacitance unit.

Table 4.1 lists the extracted α, R, Q with the calculated C_{eff}, and Figure 4.25 shows the variation of R and C_{eff} during the relation process. There is no significant variation of α under excitation and relaxation. Therefore, it can be inferred that the degree of deformation of the CPE is not seriously affected by the light exposure. This seems logical as the physical meaning of the CPE was mainly attributed to geometrical problems. In contrast, R dramatically reduces under light and gradually increases towards its final state value. The decrease of R can be interpreted as the increase of the conductivity by photogenerated excess carriers. C_{eff} is practically constant under illumination/relaxation process so that we can think of this capacitance as the geometrical capacitance that is defined by geometrical overlap of the two metal electrodes. Therefore, it is possible to estimate the dielectric constant of the P3HT film by using the parallel-plate capacitor equation. Using the average capacitance value 257 pF, the film thickness 9.6 μm, and the area 0.78 cm^2, the dielectric constant of P3HT is calculated to be 3.6, which would correspond to the quasistatic value.

Now, it is possible to tactically simplify the impedance response to a variation of the bulk resistance R of P3HT because there was no critical influence of light on either α or C_{eff}. At this point, we can regard the Au/P3HT/Au diode as a photoconductor due to its ohmic conduction [Figure 4.22] and photosensitive resistance [Figure 4.25]. We first convert the extracted resistances (R) to the conductivities (σ) by taking the geometrical dimensions into account, and calculated the photoconductivity (σ_{ph}) of the device by

$$\sigma_{\text{ph}} = \sigma_{\text{illu}} - \sigma_{\text{dark}}, \tag{4.36}$$

where σ_{illu} indicates each conductivity value under illumination/relaxation and σ_{dark} is the dark conductivity from the resistance of the final fully relaxed state.
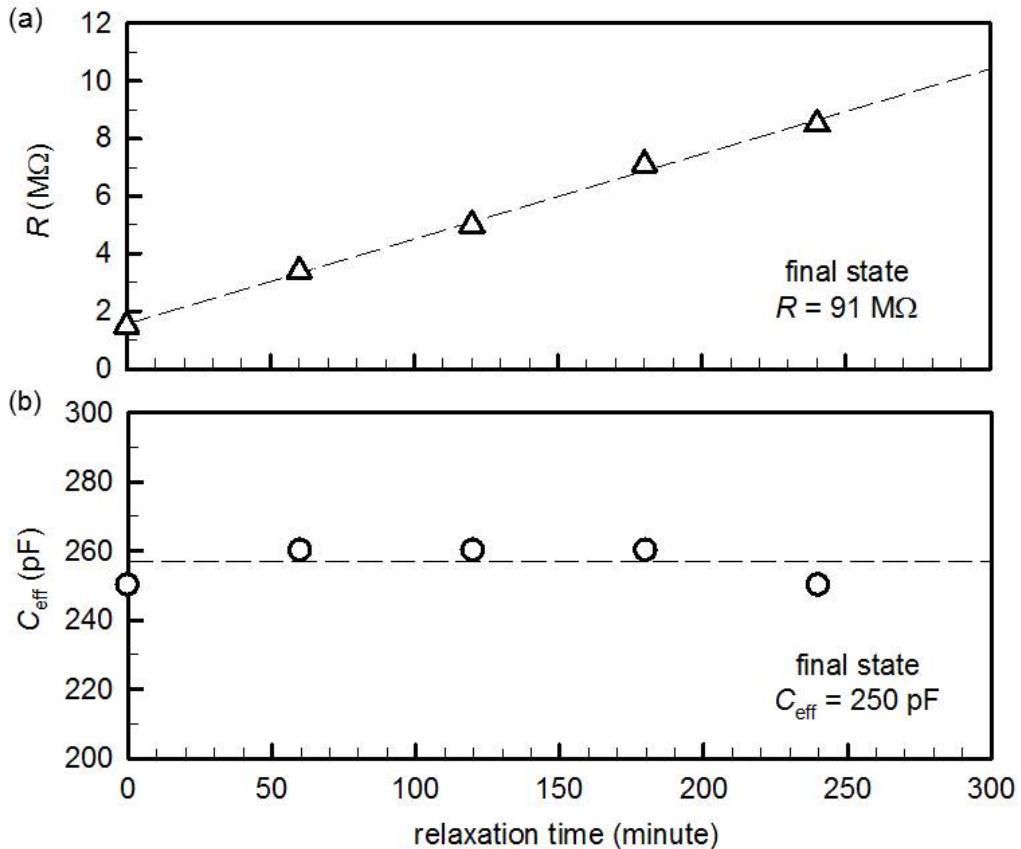
Figure 4.25: Variation of the circuit parameters: (a) resistance R and (b) effective capacitance C_{eff}. Final (or relaxed) state value is also indicated in each panel.

Figure 4.26 shows the change of σ_{ph} as a function of relaxation time. From conventional generation/recombination kinetics, it is expected that the photogenerated electron-hole pairs recombine with a carrier-density-dependent recombination rate at every instance. This mechanism results in an exponential decay of the photoconductivity [21], which is expressed as

$$\sigma_{\text{ph}}(t) = \sigma_{\text{ph},0} \exp\left(-\frac{t}{\tau_d}\right). \tag{4.37}$$

Here, $\sigma_{\text{ph}}(t)$ is the time-dependent photoconductivity of the P3HT layer, $\sigma_{\text{ph},0}$ the photoconductivity under illumination (when the relaxation begins), and τ_d the decay time constant. The best fit curve shown in Figure 4.26 gives $\tau_d = 110$ minutes.

Such an extremely slow relaxation behavior (or light-induced memory effect) of the P3HT film in metal/semiconductor/metal configuration has not been found in the literature. Previously, photocapacitance measurements of the P3HT-based MIS (metal-insulator-semiconductor) device showed prolonged recovery of the modulated
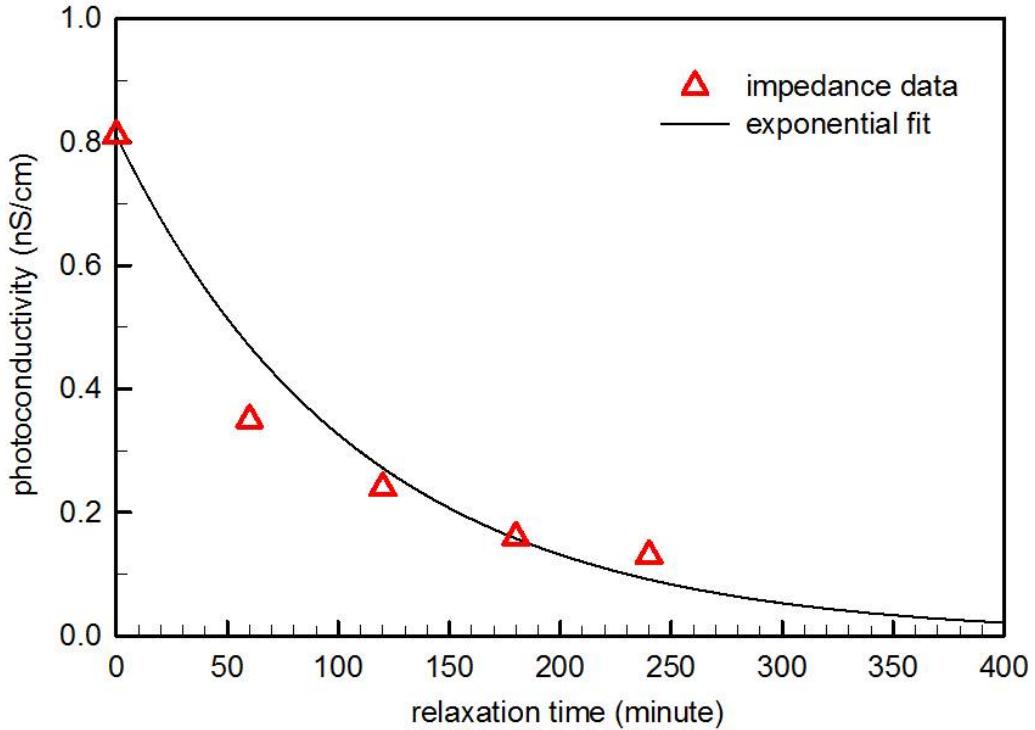
Figure 4.26: Photoconductivity as a function of time. The calculated values are compared with the exponential fit that accounts for the recombination of the excess carriers with a fixed decay time constant.

capacitance due to trapped minority carriers at the interface states [115, 116]. More recently, Kim and co-workers explained the persistent photocurrent in dihexylquarterthiophene (DH4T) organic transistor with a slow detrapping of photogenerated carriers and they observed that the gate electric field accelerated this detrapping process [117]. A similar phenomenon was reported by Lutsyk and co-workers on the study of poly(3-octylthiophene) (P3OT) transistor and they also emphasized the role of gate bias for erasing the memory effect [118]. Despite the dissimilarities in the material and/or device geometry, it is likely that these results help interpret the observation in our study. Note that our impedance spectroscopy results in Figure 4.23 are obtained under dc bias of 0 V and a P3HT film with disordered polymer network should contain high density of defect or trap sites. With these two factors combined, photogenerated carriers can easily be trapped in the bulk film and their detrapping would take long time without assisting high electric field applied. Therefore, the slow detrapping of carriers results in a slow recombination and in turn, leads to the persistent effect on the device.

4.3   Gap-type diodes

An organic gap-type diode has a planar geometry with two electrodes on the same side of the semiconductor [Figure 4.1 (c)]. The electrodes can be either on top or at the bottom of the semiconductor depending on the fabrication sequence. We use the term 'gap-type' diode because the gap between two coplanar electrodes define the zone of the current flow. Our particular interest is in the observation and the modeling of the current-voltage behaviors of this device.

Historically, the early experimental report by Polke and co-workers in 1963 was an important result for understanding the current of gap-type devices [119]. They measured the current in thin layers of crystalline Se and the observed I-V characteristics were linear at low voltage and quadratic at higher voltage. The quadratic regime brought evidence for the space-charge-limited conduction (SCLC), but they observed that the scaling rule for the electrode spacing L was not exactly the same as that predicted by the Mott-Gurney law for vertical SCLC [98]. In his paper in 1966, Geurst (by using the notation 'gap-type') theoretically described the SCLC in the thin-film geometry, where the current is basically 2-D, but the vertical electric field plays an important role of accumulating the space charge [120]. In 1967, Zuleeg and Knoll applied the analytical model of Geurst to their Si thin-film gap structures, while confirming the validity of the model by observing the current proportional to L^{-2} [121]. They also realized that when the Mott-Gurney model is applied to the same data, the extracted mobility is highly overestimated.

Analysis of SCLC in gap-type diodes can be a useful way to estimate the mobility of organic materials. However, there are only a few papers on organic gap-type diodes in the literature. Recently, the fabrication of a gap-type structure and the extraction of the in-plane mobility by Geurst's model have been conducted for pentacene crystals [122], dithienothiophene-derivative thin-films [123], rubrene crystals [124], and 4-hydroxycyanobenzene crystals [125].

Here, we present the measurement and modeling of the current in organic gap-type diodes based on evaporated pentacene and solution-cast 6,13-bis (triisopropy-lsilylethynyl) pentacene (TIPS-pentacene). We propose the extraction of the bulk mobility and the thermal carrier concentration by complementary use of the linear and quadratic regimes. Then, a compact analytical model for connecting both regimes is introduced.
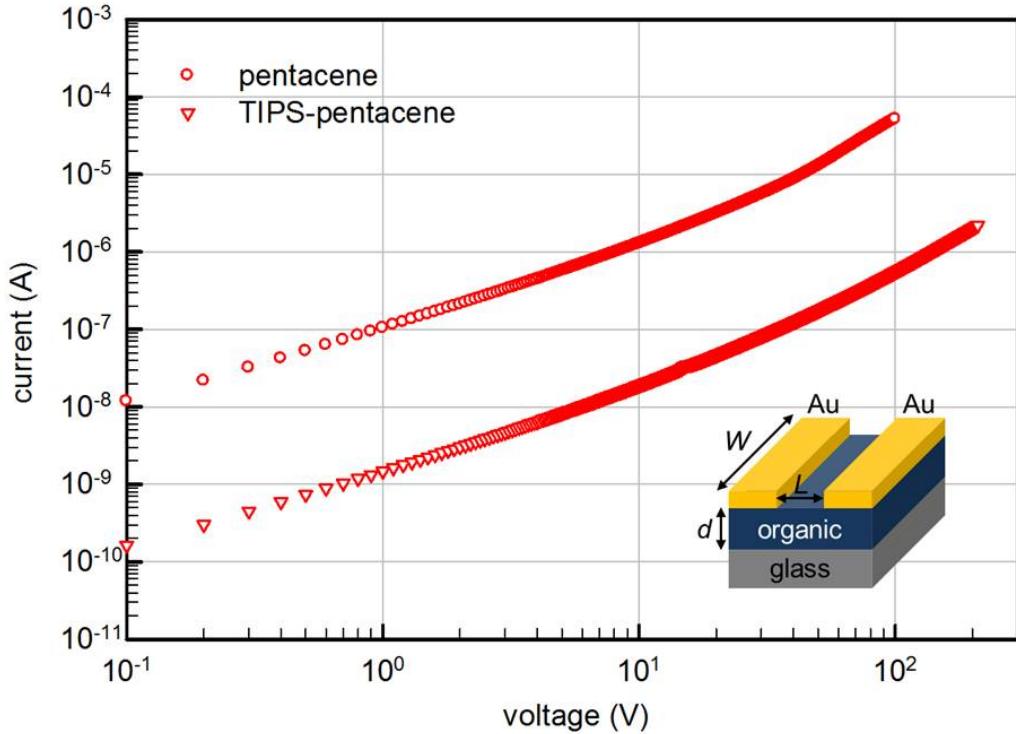
Figure 4.27: Current-voltage characteristics of pentacene and TIPS-pentacene gap-type diodes drawn on a log-log plot. The inset is the schematic device structure.

4.3.1   Current in organic gap-type diodes

Organic gap-type diodes were fabricated with the top-contact geometry illustrated in Figure 4.27. Vacuum-evaporated pentacene and spin-coated TIPS-pentacene film serve as the organic semiconductor and vacuum-evoparted Au electrodes are for the injecting electrodes that define the gap structure. The geometrical dimensions are identical in the two diodes in analysis. The electrode width W is 1000 μm, the electrode spacing L is 30 μm, and the film thickness d is 150 nm. The measured electrical characteristics in Figure 4.27 show the two-regime behavior distinguished by the slope in the log-log plot. Current is proportional to the voltage at low voltage and it becomes proportional to the square of the voltage at higher applied voltage.

4.3.2   Compact modeling approach for gap-type diodes

Here, we describe the separate analysis of the two current mechanisms with a systematic parameter extraction, and finally suggest a compact model that can capture the continuous transition from ohmic to SCLC regime.

Figure 4.28 shows the low-voltage regime (-1 V to 1 V) *I-V* data. We note an
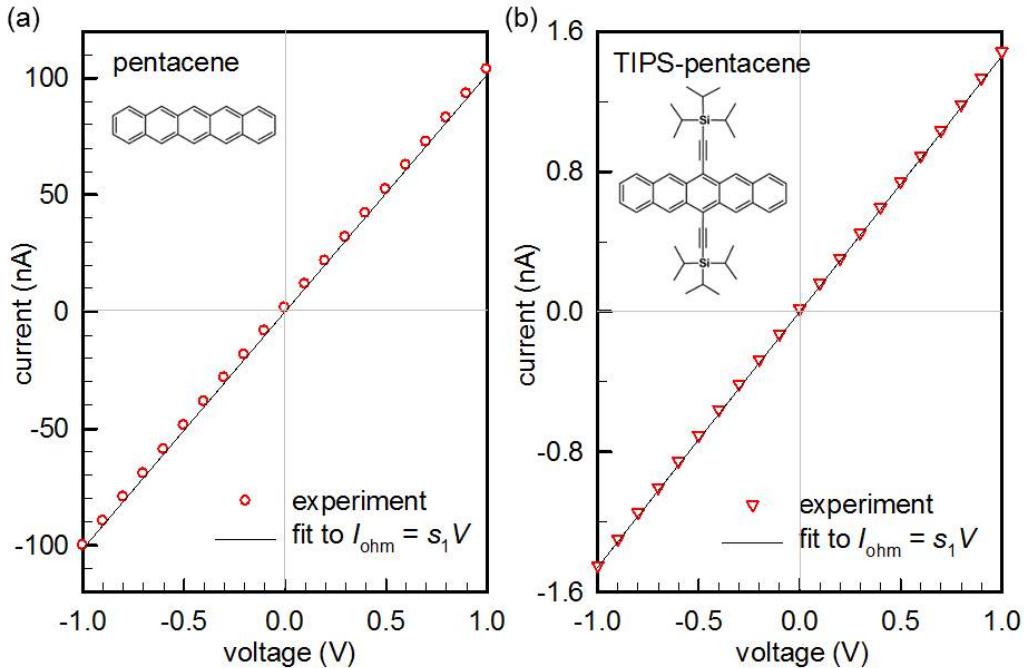
Figure 4.28: Ohmic regime *I-V* data and model for (a) the pentacene diode and (b) the TIPS-pentacene diode. The inset shows the corresponding molecular structure.

excellent symmetry of the curves, which excludes non-ideal contact problems [124]. The current in this linear regime is supposed to be the drift current of the thermal carriers originating from small amount of unintentional dopants [126]. We can write the ohmic current I_{ohm} as

$$I_{\text{ohm}} = \frac{qp\mu W d}{L} \times V = s_1 \times V, \tag{4.38}$$

where p is the thermal hole density, μ is the hole mobility, and s_1 represents the slope of the linear regime that actually corresponds to the conductance of the film. As shown in Figure 4.28, the experimental data can be nicely fitted to Equation (4.38), with extracted s_1 of each diode. The slope s_1 gives access to the carrier density p by

$$p = \frac{s_1 L}{q\mu W d}, \tag{4.39}$$

where the value of μ will be given from the SCLC regime.

For the high-voltage SCLC regime, we can refer to Geurst's model [120, 121] and express I_{SCLC} as

$$I_{\text{SCLC}} = \frac{2\mu\epsilon_s W}{\pi L^2} \times V^2 = s_2 \times V^2. \tag{4.40}$$

As shown in Figure 4.29, it is recommended that the current in the SCLC regime is drawn as a function of V^2 to see the linearity. Both diodes exhibit good linearity, and
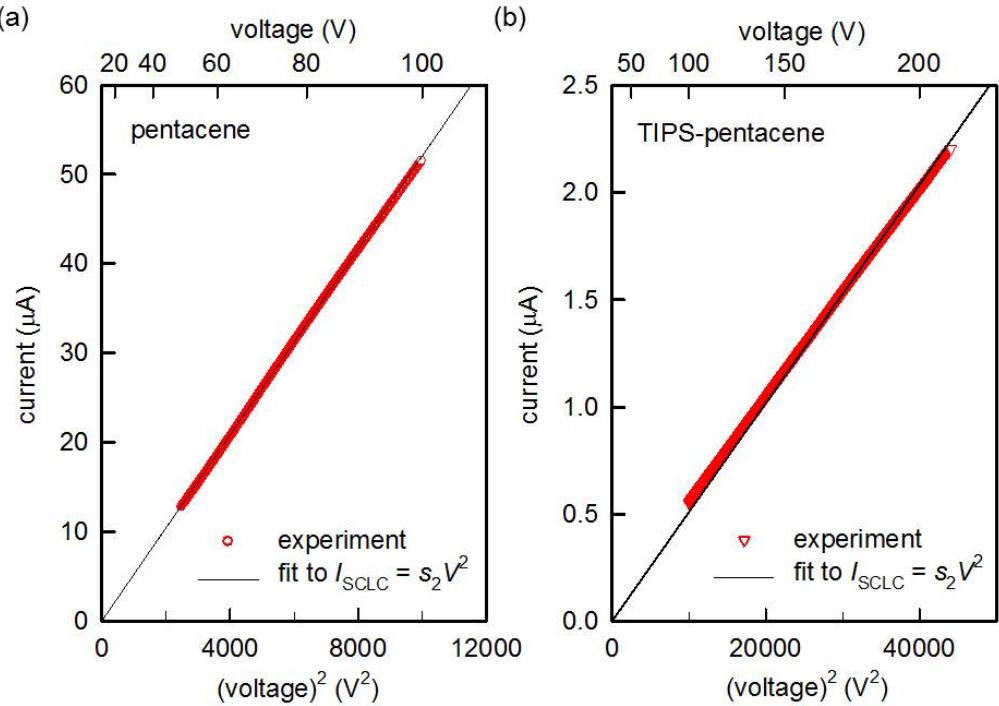
Figure 4.29: SCLC regime current as a function of V^2 for (a) the pentacene diode and (b) the TIPS-pentacene diode.

we can estimate the slope s_2 by conducting a linear regression through the origin. The mobility μ is now extracted by

$$\mu = \frac{s_2 \pi L^2}{2 \epsilon_s W}. \tag{4.41}$$

We have independently modeled I_{ohm} and I_{SCLC}, and naturally they can only describe the corresponding regime. A single compact model can be proposed by using a transition technique for smoothly linking the different regimes. The basic idea is to have the two current components in overall voltage range, but to make appear the component with the greater magnitude at each regime. A conventional method is to take a generalize mean (also known as power mean or Hölder mean) of the two components [76]. With this method, we finally write the expression for the total diode current I_{diode} as

$$I_{\mathrm{diode}} = [(I_{\mathrm{ohm}})^m + (I_{\mathrm{SCLC}})^m]^{1/m}, \tag{4.42}$$

where the parameter m controls the abruptness of the transition at the point where two current components meet.

Figures 4.30 and 4.31 show the comparison of the experimental data in the entire measurement range with the modeled cuves with I_{diode}. The currents in both
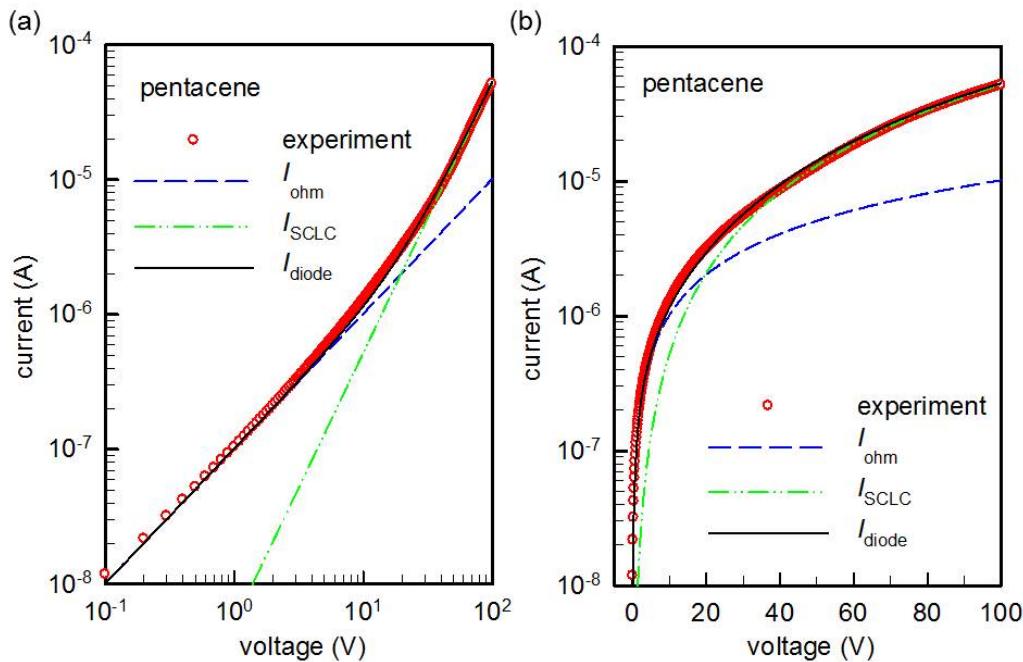
Figure 4.30: Final comparison of the model with the experimental data of the pentacene gap-type diode; (a) log-log plot and (b) semilog plot.
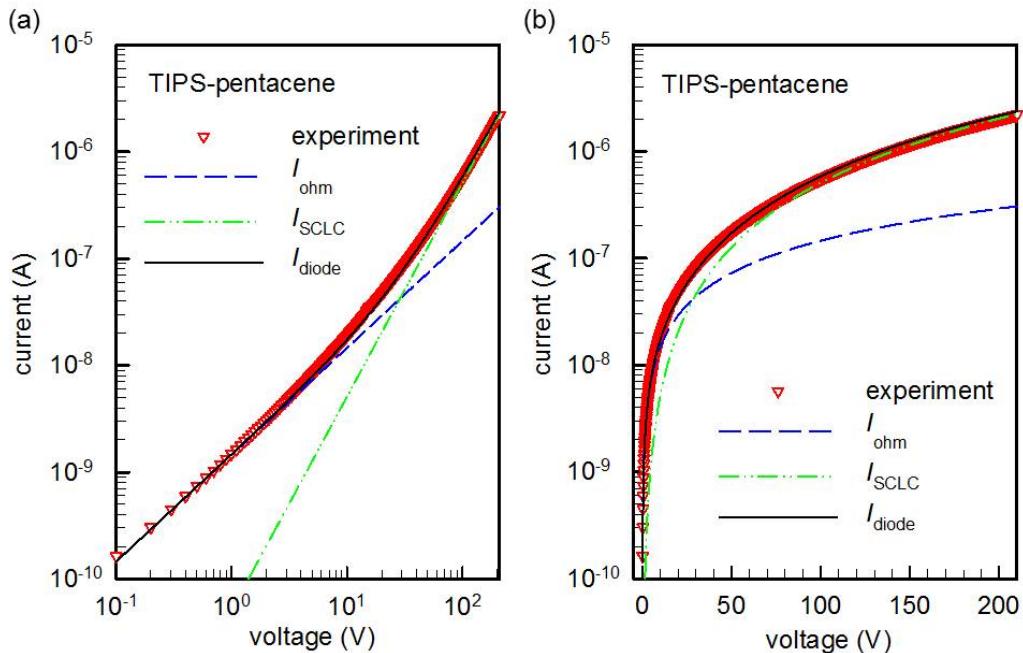
Figure 4.31: Final comparison of the model with the experimental data of the TIPS-pentacene gap-type diode; (a) log-log plot and (b) semilog plot.

Table 4.4: Model parameters for the pentacene and TIPS-pentacene gap-type diodes.

	W [μm]	L [μm]	d [nm]	ε_s	μ [cm²/V·s]	p [cm⁻³]	m	σ_{ohm} [S/cm]	V_{SCLC} [V]
pentacene	1000	30	150	$3.6 \times \varepsilon_0$	2.3	5.5×10^{14}	1.9	2.0×10^{-4}	19
TIPS-pentacene	1000	30	150	$3.6 \times \varepsilon_0$	0.023	8.1×10^{14}	1.3	2.9×10^{-6}	29

pentacene and TIPS-pentacene diodes are well described by the proposed compact model with a smooth transition from ohmic to SCLC regime. The model parameters used for the final I_{diode} model are summarized in Table 4.4. It should be pointed out that, in this modeling, the mobility is assumed to be constant over the whole voltage range. The assumption is based on the well-documented carrier-density-dependence of the mobility in organic semiconductors [127, 128]. The carrier density in a diode is generally orders of magnitude lower than that involved in OFETs, and the low-density mobility is less dependent on the carrier density. Our experimental data support this assumption, because no variation of the slope in *I-V* curve is observed especially in the SCLC regime. Additionally, the extracted mobility is regarded as a bulk mobility, because the current flows through the whole volume of the film despite its 2-D nature. The situation is different in OFETs, because the current is confined to the thin accumulation region at the semiconductor/insulator interface. We infer that, for the same material, the bulk mobility in a gap-type diode can be higher than the field-effect mobility in an OFET, because there exist various scattering centers related to the roughness of the insulator in an OFET, which eventually hinders the charge transport [129, 130]. The pentacene mobility as high as 2.3 cm²/V·s in our result might support this argument. However, the mobility of the TIPS-pentacene film is lower than expected, which can be attributed to the poor ordering of the solution-cast molecules on the glass substrate.

Two parameters σ_{ohm} and V_{SCLC} are additionally given in Table 4.4. σ_{ohm} is the ohmic-regime conductivity calculated from the extracted μ and p by

$$\sigma_{\mathrm{ohm}} = qp\mu. \tag{4.43}$$

V_{SCLC} is the SCLC onset voltage defined by the intersection point of I_{ohm} and I_{SCLC}. By equalizing Equations (4.38) and (4.40) at $V = V_{\mathrm{SCLC}}$, we get

$$V_{\mathrm{SCLC}} = \frac{qpd\pi L}{2\epsilon_s}. \tag{4.44}$$
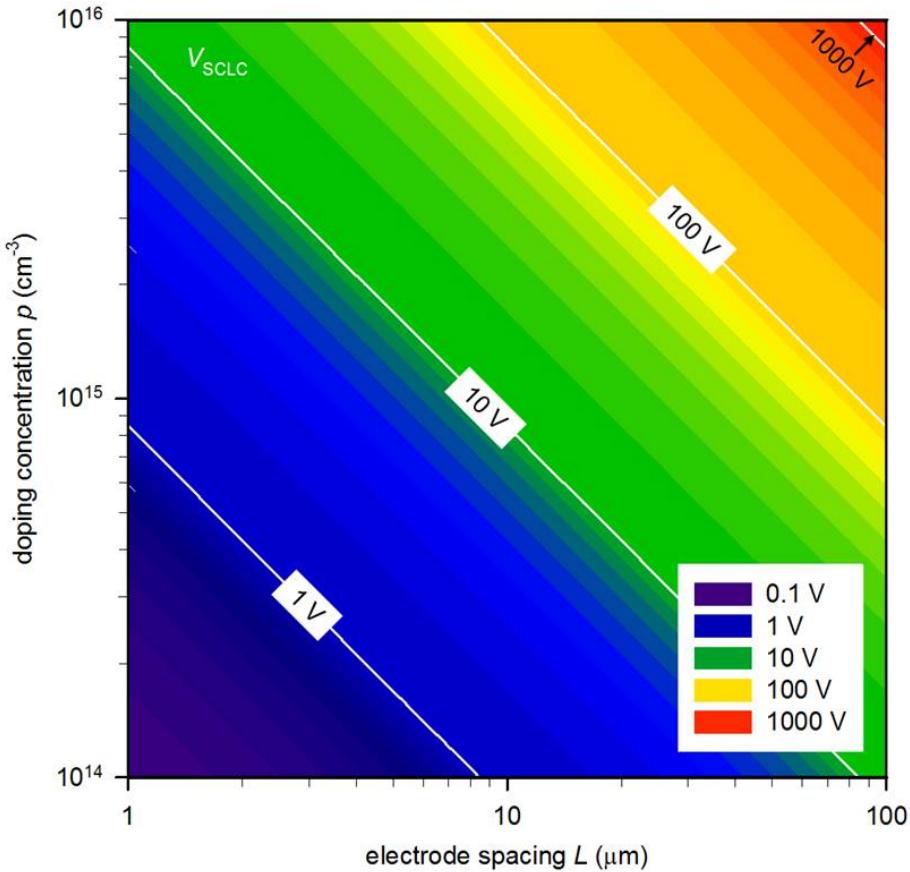
Figure 4.32: The SCLC onset voltage V_{SCLC} calculated by Equation (4.44) for expecting the operation regime of an organic gap-type diode. Fixed parameters are d=150 nm and $\epsilon_s = 3.6 \times \epsilon_0$.

This expression provides a meaningful insight into the operation of an gap-type diode. V_{SCLC} is a function of geometrical dimensions and unintentional doping concentration and if the measurement voltage does not reach V_{SCLC}, we will only observe the ohmic current. We put emphasis on minimizing the geometrical gap L for monitoring SCLC behavior, otherwise the device is rather considered as a thin-film resistor due to its extended ohmic regime. Figure 4.32 shows the calculated V_{SCLC} with varying p and L with fixed d=150 nm and $\epsilon_s = 3.6 \times \epsilon_0$. As V_{SCLC} is a linear function of both p and L, a huge variation is traced here, upon considering realistic range of p and L.

Chapter 5

Modeling organic transistors

Transistors are three-electrode devices that are categorized primarily by the device structures, and also by the materials used and main applications [21]. In this chapter, we present the modeling of two organic transistor structures; organic metal-semiconductor field-effect transistors (OMESFETs) and organic field-effect transistors (OFETs).

An OMESFET is made up of a metal-semiconductor (MES) 'blocking' contact at the gate electrode with two injecting source/drain electrodes also in intimate contact with the semiconductor [Figure 5.1(a)]. In the literature, there is only a small number of publications on organic MESFETs. In 2007 and 2008, Takshi and co-workers reported experimental and simulation results on P3HT-based OMESFETs [85, 91]. They emphasized the ease of fabrication process compatible with a printing technique and also the possibility of realizing low-voltage operation. More recently, MESFETs fabricated on rubrene single crystals were reported by two different groups. In 2009, Kaji and co-workers demonstrated rubrene MESFETs in coplanar geometry, where all
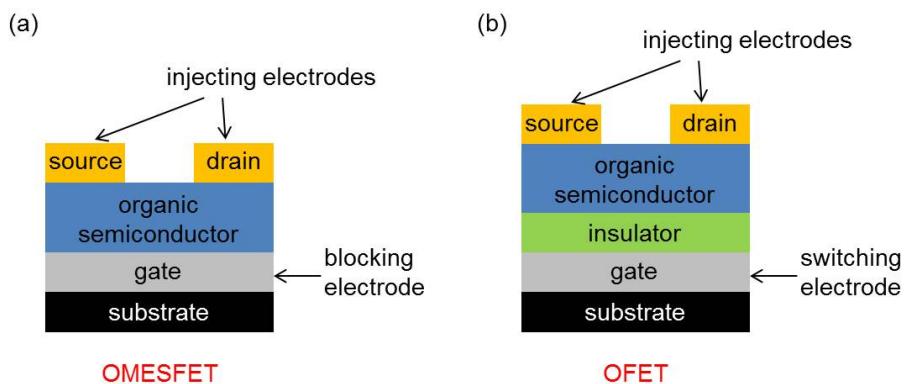
Figure 5.1: Illustration of the representative device structure for (a) an OMESFET and (b) an OFET.

three contacts are deposited on the same side of the semiconductor [131]. The results by Braga and co-workers in 2010 shows staggered type rubrene MESFETs, where the gate electrode is separated from the source/drain electrode by the semiconductor [87]. Here, we present experimental results on pentacene-based MESFETs. Based on the full depletion in unintentionally doped pentacene, we also suggest simulation study for understanding operation mechanism that is necessarily different from the depletion-modulation in conventional MESFETs [21].

A representative OFET device structure is illustrated in Figure 5.1(b). The sole difference from an OMESFET is the existence of an insulator layer between the gate and the semiconductor. Because this structure contains a metal-insulator-semidoncutor (MIS) block, the notation of 'OMISFET' is also used [48]. Historical view and main applications of OFETs have been already explained in Chapter 1. Here, we focus on the geometrical impact on the device characteristics, charge-based contact resistance model, and compact modeling for circuit simulations.

5.1   OMESFETs

5.1.1   Current-voltage characteristics

The device structure of the fabricated OMESFETs is shown in Figure 5.2. This structure is characterized by the relative positions of the electrodes and to be called the top-gate, staggered structure. We used Al as the gate, Au as the source/drain electrodes, and 1 μm of pentacene as the channel material. The structure used here can be considered as two vertical rectifying Au/pentacene/Al diodes with a common Al top electrode and isolated Au bottom electrodes. We first measured two diodes within an OMESFET shown in the optical image in Figure 5.2. We observe that the *I-V* curves well exhibit the three-regime behavior detailed in the diode modeling part Section 4.1; reverse, injection-limited, and bulk-limited currents. Note here that the forward-bias regime corresponds to the negative gate voltage (V_G). As desired, the two *I-V* curves are identical.

To examine basic transistor behaviors, we measured the output characteristics of an OMESFET that has 400 μm of channel width (W) and 50 μm of channel length (L). Figure 5.3 shows the results. Note that the drain current (I_D) modulation by V_G can be achieved within a very small variation of V_G. The transistor is called a 'normally-on' device because substantial current flows at $V_G = 0$ V and this zero-gate current can be lowered (in magnitude) by applying a positive V_G.
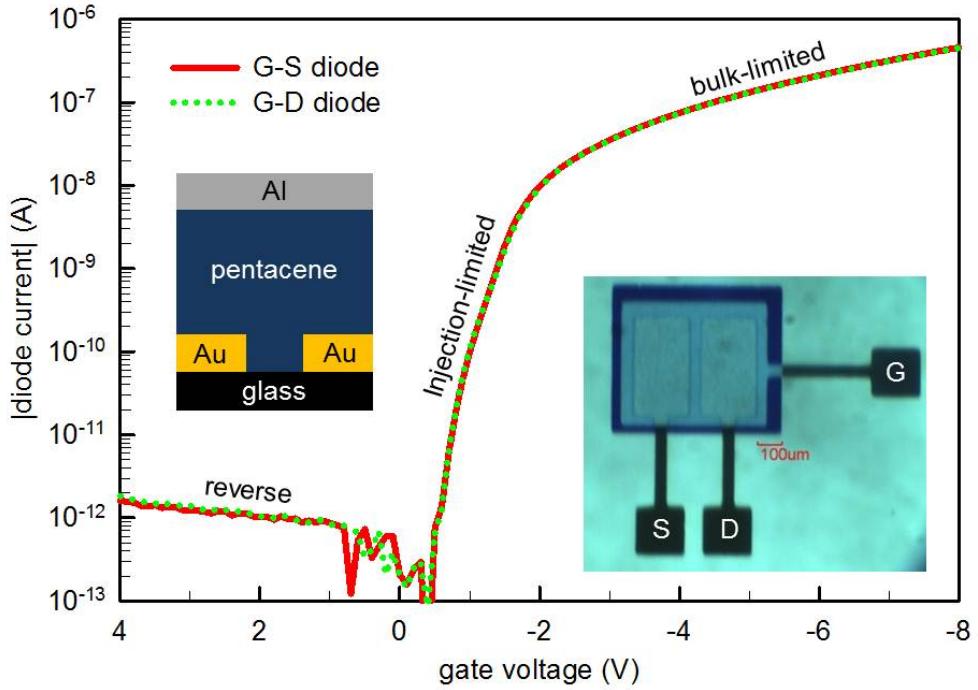
Figure 5.2: Current-voltage characteristics of the two organic diodes constituting an OMESFET. The left inset shows the schematic representation of the top-gate staggered device structure. The right inset is an optical microscopic image of the measured device.
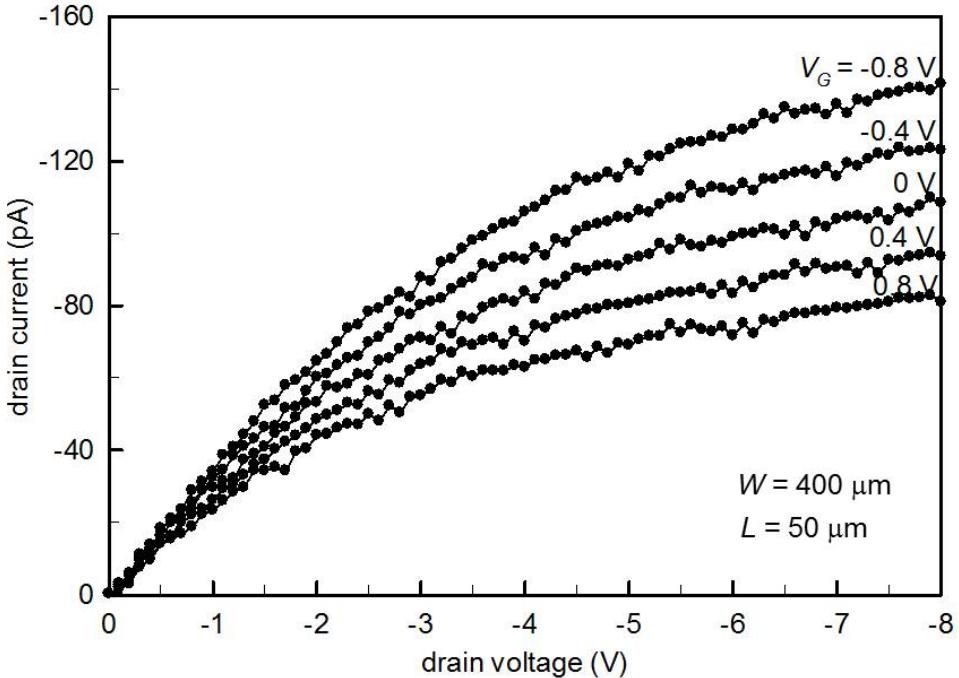
Figure 5.3: Output characteristics of an OMESFET.
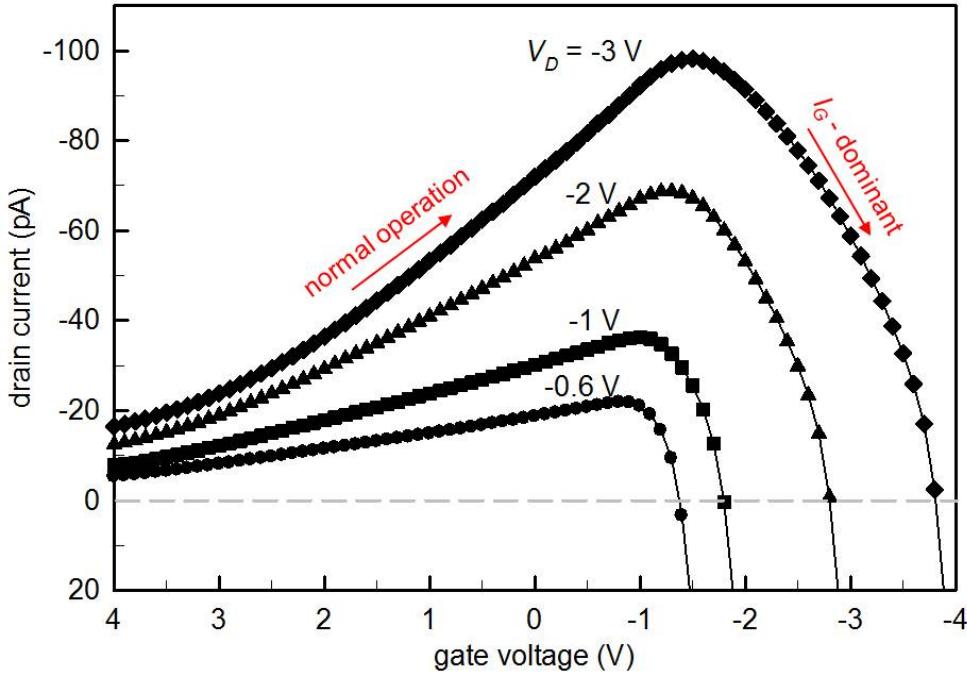
Figure 5.4: Transfer characteristics of an OMESFET.

The measured transfer characteristics (I_D-V_G) of the same device at different V_D are shown in Figure 5.4. We first notice two distinguishable regimes with respect to V_G, according to whether I_D increases or decreases by sweeping V_G from positive to negative values. We marked the first regime as the 'normal operation' regime because it is coherent with the output characteristics shown in Figure 5.3; around $V_G = 0$ V, negatively biasing gate electrode results in higher $|I_D|$. In contrast, when V_G becomes too negative, $|I_D|$ starts to decrease rapidly and finally passes $I_D = 0$. Here we call this second regime 'I_G-dominant' regime, which will be explained in more detail hereinafter. The effect of increasing $|V_D|$ on the transfer curves is an overall negative shift of the current I_D and a negative shift of the transition point between two regimes.

5.1.2   Operation mechanism

The experimental results on pentacene OMESFETs allow us to make sure of the transistor behaviors with particular role of V_G and V_D in each measurement condition. However, the basic operation mechanism seems unclear at this point. It is because the observation of full depletion in pentacene (Section 4.1) prevents adopting the conventional MESFET theory that explains the current modulation by the depletion

Table 5.1: Physical parameters used for the finite-element simulation of an OMES-
FET.

Parameter	Value
Temperature	300 K
Pentacene thickness	1.0 μm
Valence band effective DOS	10^{20} cm^{-3}
Doping concentration	0 cm^{-3}
Electron affinity (LUMO)	2.8 eV
Ionization potential (HOMO)	5.2 eV
Hole mobility	0.5 cm^2/V·s
Electrode thickness	50 nm
Gate work function (Al)	4.2 eV
Source/drain work function (Au)	4.9 eV

width changing with V_G [21]. The reason of the rapid decrease in I_D in the trans-
fer characteristics is also to be verified in depth to define and distinguish different
operation regimes.

For those purposes, we defined a two-dimensional finite-element model for the
pentacene MESFET and simulated the structure using ATLAS. The model structure
is equivalent to the real device shown in Figure 5.2 and the physical parameters used
for simulation are listed in Table 5.1.

Figure 5.5 shows simulated 2-D contour maps for the charge-carrier distribution
inside the pentacene film at different V_G values with zero V_D. Note first the hole
concentration map at thermal equilibrium in Figure 5.5 (b). As the carrier density
at a metal/semiconductor interface is determined by the injection barrier, we first
observe the large concentration gradient from the source/drain regions to the gate
region. The hole injection barriers estimated from the parameters in Table 5.1 are
0.3 eV for the Au/pentacene junction and 1 eV for the Al/pentacene interface. When
a positive V_G is applied, the injected holes from Au are much more confined near
the source/drain electrodes [Figure 5.5 (a)]. Therefore, a positive V_G decreases the
effective bulk conductivity of the semiconductor, which in turn leads to the decreased
$|I_D|$ observed in Figure 5.3 at $V_G = 0.8$ V. On the other hand, with a negative V_G,
the whole volume of the pentacene is more populated with holes as shown in Figure
5.5 (c), thus raising the conductivity and current between the source and the drain.
Hence, together with the measured output curves, we realize that the role of V_G is to
repel or attract the injected charges, and thus to control the bulk conductivity that
determines the magnitude of I_D.

Figure 5.6 shows the simulation results at fixed V_D, which shows the effect of V_G
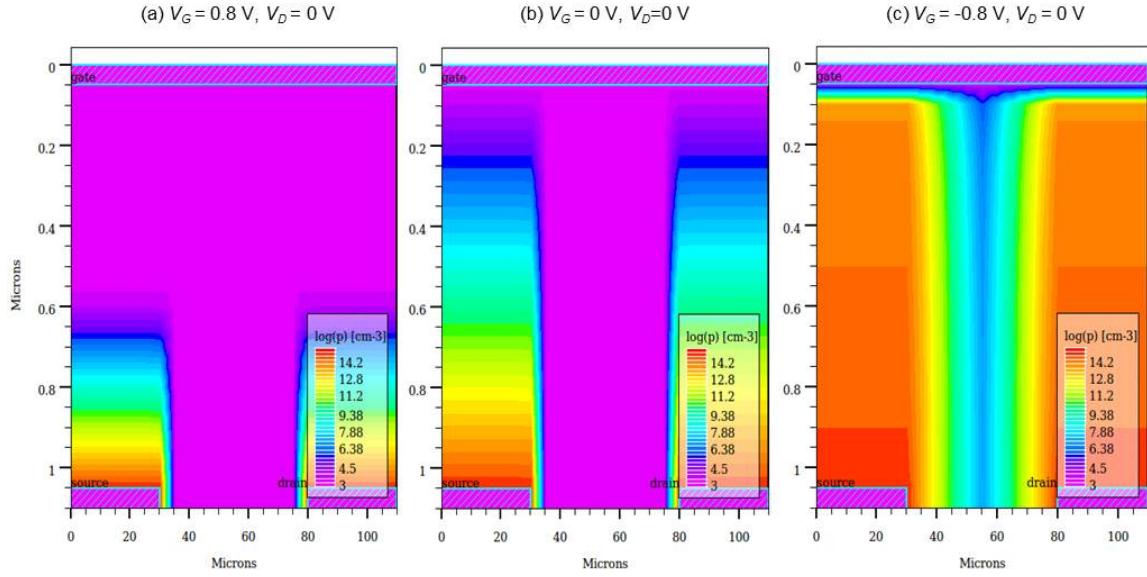
Figure 5.5: 2-D simulation results for the hole distribution inside the pentacene film at different biasing conditions.

on the current distribution. This result helps understand the transfer characteristics in Figure 5.4. The direction of the current vectors is to be noticed here, especially that in the gate-drain (G-D) diode region marked by a green box in each panel. First, when $V_G = -1$ V [Figure 5.6 (a)], because $|V_D| > |V_G|$, the G-D diode is reversely biased and the current vectors in the G-D zone points toward the drain. This situation corresponds to the normal operation regime, because the current mainly flows into the drain electrode, with the bulk conductivity modulated by small change in V_G. Next, with $V_G = -2$ V, now the effective voltage applied to the G-D diode is zero, which is confirmed by current vectors in both directions compensating each other. Finally when $|V_G| > |V_D|$ [Figure 5.6 (c)], the G-D diode is turned on (forward-biased) and all current vectors point upward. In this condition, the net current flows out of the drain, which corresponds to the positive drain current observed in Figure 5.4 when $|V_G|$ is too high. In other words, the gate leakage current I_G is too high because both G-S and G-D diodes provide large current toward the gate electrode, without no effective conduction between source and drain. Therefore, this regime is to be designated as 'I_G-dominant' regime.

5.1.3 Effect of the channel dimension

The simulation results indicate that the competition between I_D and I_G is a critical factor determining the operation mode and the order of each current component. At
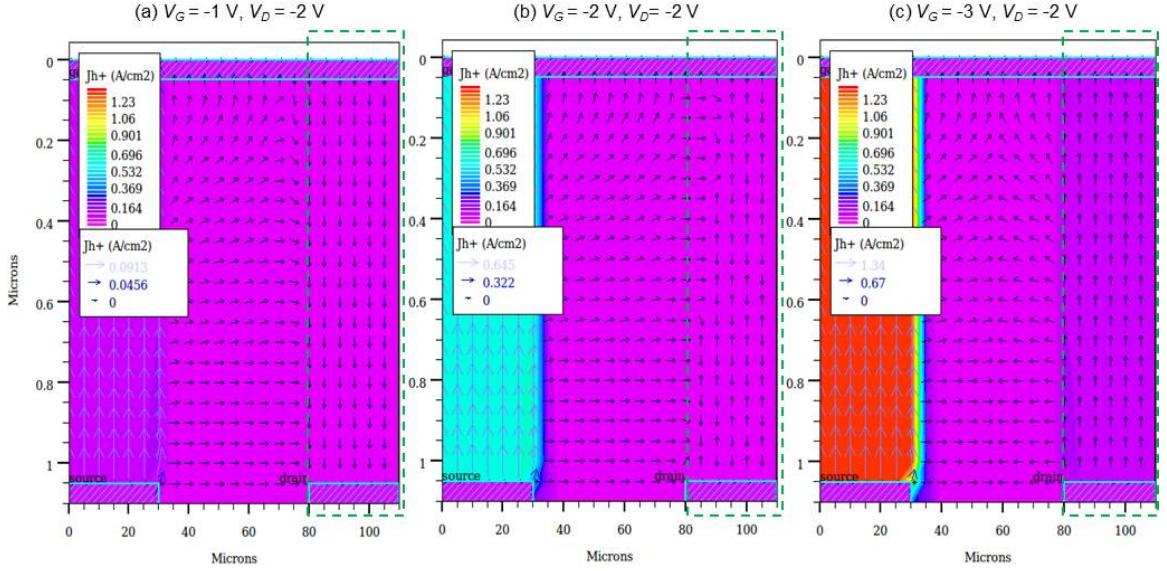
Figure 5.6: 2-D simulation results for the hole current density distribution (contours) and the local current vectors (arrows) at different biasing conditions. A green box (dashed lines) is located at the G-D diode region, in which the direction of the current vectors changes with V_G.

this point, we realize that the physical dimensions of the device, such as semiconductor thickness and channel dimensions (W and L), can influence this competition because the strength of the electric field created by V_G and V_D depends on these geometrical dimensions. In order to investigate the effect of the channel dimensions on the OMESFET current, a number of transistors with different W and L have been characterized.

Figure 5.7 (a) compares the output curves of the OMESFETs with four different L values. The fixed applied V_G is -0.4 V (normal-operation regime) and W is 400 μm in all four devices. At several V_D points on the output curves, the currents I_D were taken and plotted as a function of L in Figure 5.7 (b). Here, we see a monotonous decrease in I_D as L increases. This tendency is explained by the variation of the strength of the lateral source-drain electric field. Even with a fixed V_D, the later electric field becomes weaker when L is larger, which in turn results in a decreased I_D. Note that this scaling property by L is also expected in general MISFET-type devices such as MOSFETs and OFETs [21, 48].

Interestingly, a non-conventional effect of W is observed in OMESFETs analyzed here, which is likely to be a specific case related to the staggered transistor architecture. Figure 5.8 (a) shows the collected output curves of the OMESFETs with three different W values and the same L of 30 μm. If the role of I_G is totally excluded, I_D
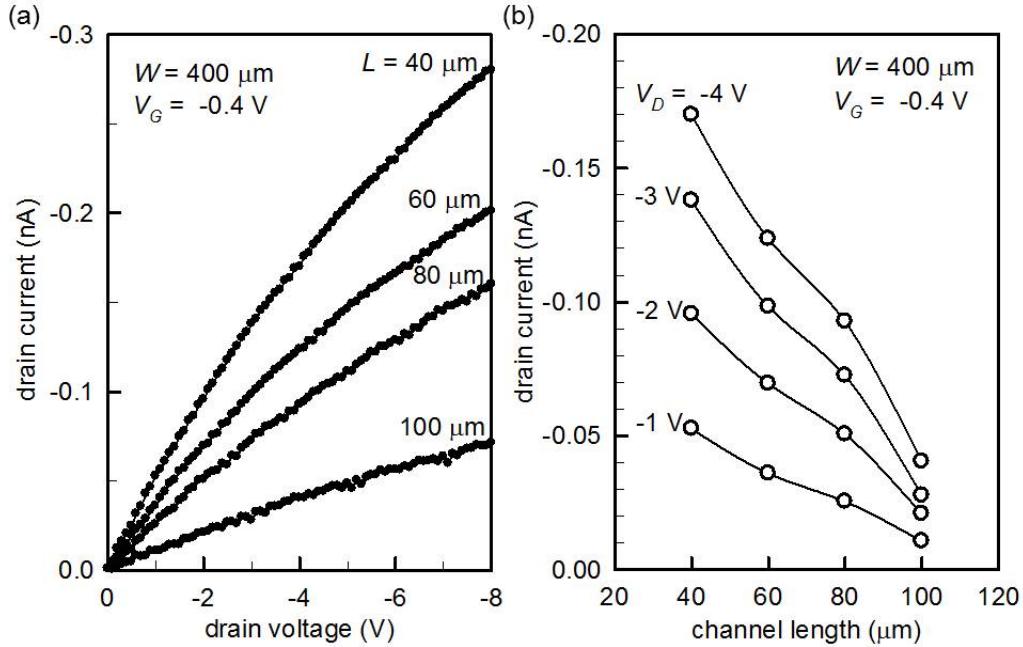
Figure 5.7: Effect of the channel length L on I_D. (a) Output characteristics of four OMESFETs with W=400 μm and different L values. (b) Variation of I_D as a function of L.

should increase with W, simply because the carrier injection cross-section is widened. Nonetheless, as shown in Figure 5.8 (b), our OMESFETs exhibit an opposite trend; rapidly decreasing I_D with increasing W. It is inferred that, with larger W, the increased active overlap area of the G-S and the G-D diode has a more significant effect than that of the increased lateral cross section. The enhancement of the I_G component by W prevents I_D benefiting from any effect of the increased geometrical area. Therefore, I_D shows a monotonous decrease with increasing W.

It should be note that, this undesired high gate leakage, which eventually disables the source-drain conduction, basically stems from the geometrical peculiarity of the staggered OMESFETs. The distance between the G-S electrodes and that of the G-D electrodes correspond to the semiconductor thickness (d =1 μm) and they are considerably lower than the S-D distance L. Under normal operation conditions where the applied V_G and V_D have similar magnitude, the vertical electric field is higher than the lateral source-drain field because $d < L$. This implies that I_G is always a dominating component over I_D, which can also be seen from the difference in order of the vertical diode current in Figure 5.2 and the lateral drain current in Figure 5.3. At variance with this situation, in coplanar MESFETs, the G-D or G-S spacing does not equals d, but is of the same order of the S-D spacing because all
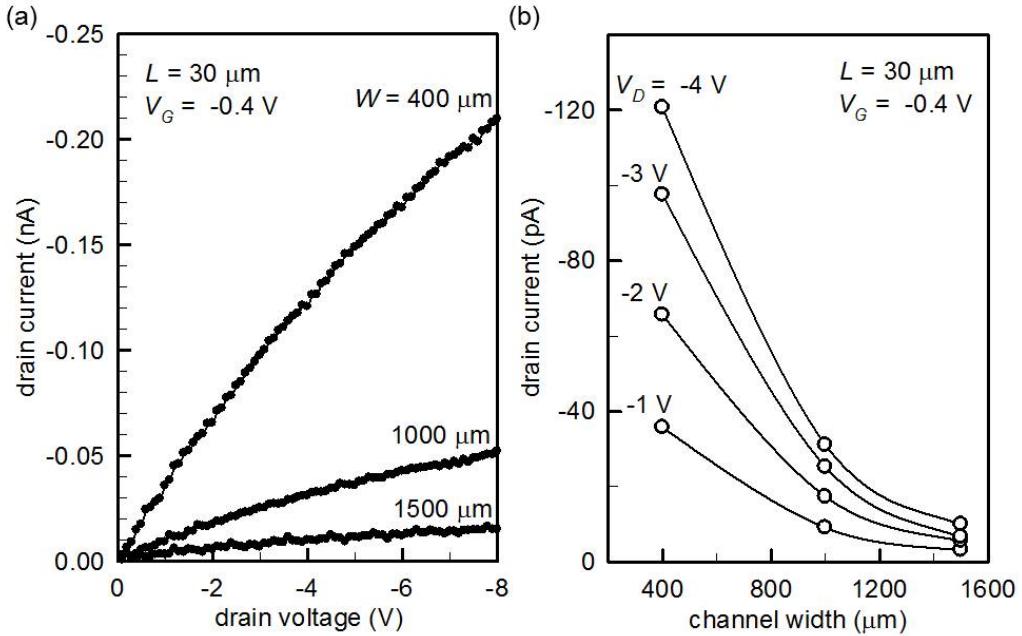
Figure 5.8: Effect of the channel length W on I_D. (a) Output characteristics of three OMESFETs with L=30 μm and different W values. (b) Variation of I_D as a function of W.

three electrodes are located on the same side of the semiconducting film. In other words, I_D can compete with the I_G with equal lateral scaling property, and generally higher lateral current is expected to flow.

5.2 OFETs

For OFET modeling, we first focused on the common geometrical variations, and addressed characteristic and critical features of each architecture in terms of their physical device behaviors. As briefly introduced in the beginning of the chapter, an OFET is composed of several functional layers. An organic semiconducting layer formed by evaporated small-molecules, solution-cast polymers, or a piece of organic single crystal constitutes the charge-transport medium through which the electrical current flows. A gate insulator makes a capacitor between the gate electrode and the conducting channel inside the semiconductor. A gate electrode controls the capacitor by accumulating or repelling the charge-carriers, which in turn switches on or off the transistor. A source electrode provides the charge carriers into the semiconductor and a drain electrode extracts them out of the semiconductor. The above-described 'function' of each layer remains the same, but there are different 'configurations' depending
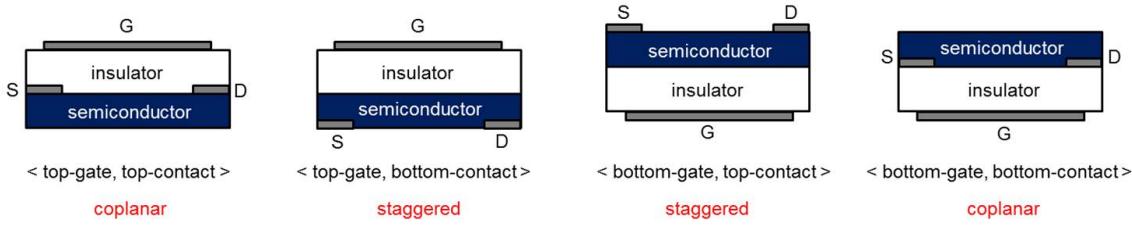
Figure 5.9: Four possible OFET geometries depending on the relative positions of the gate (G) and the source/drain (S/D) electrodes.

on their relative positions with respect to their physical support, the substrate.

Figure 5.9 shows the four possible OFET structures [37, 132, 133]. Traditionally, two criteria are applied for categorization; the position of the gate electrode with respect to the whole structure and the position of the source/drain electrodes with respect to the semiconductor. The four names given in Figure 5.9 are explicative for the corresponding structure. In addition, these four main structures can be grouped into staggered or coplanar geometry (see the red notations in Figure 5.9). By definition, in staggered geometry, the source/drain electrodes are separated from the conducting channel by the semiconductor. In contrast, the source/drain electrodes are on the same plane with the conducting channel in coplanar transistors [134, 135].

5.2.1   Staggered versus coplanar structure

Here, for simplicity, we restrict our discussion to the bottom gate configuration. In this case, the top-contact (TC) structure represents the staggered geometry and the bottom-contact (BC) structure is for the coplanar geometry. In the literature, many experimental studies on comparative analysis of the TC versus BC OFETs can be found [134, 136–138]. It has been generally observed that TC OFETs show superior electrical performance compared to the BC OFETs under the same fabrication condition, especially in terms of the field-effect mobility (μ) and the contact resistance (R_c).

Several factors have been addressed for explaining this tendency. For molecular semiconductors such as pentacene, the morphological factor is considered to be crucial. In BC geometry, the molecules evaporated on a highly reactive metal surface fail to form well-ordered region, but they are rather flat-lying or randomly oriented [136,139]. This leads to poor electrical transport property at the source/channel interface, whereas there is no such morphological discontinuity in TC OFETs [138].
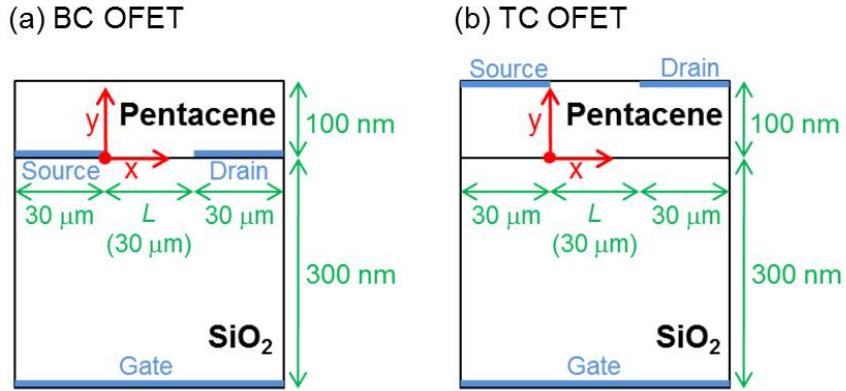
Figure 5.10: Device structure and physical dimensions used for the numerical 2-D simulations; (a) bottom-gate bottom-contact OFET, (b) bottom-gate top-contact OFET.

Another commonly accepted advantage of TC OFETs is related to the metal penetration into the organic film. Because of the fragility of organic molecular films, the metal cluster deposited on top of an organic layer can form more continuous interface, whereas, in BC OFETs, this interface should be mechanically sharp. As discussed in [132, 140], the penetrating metal particles in TC OFETs can eventually reach close the channel, substantially favoring charge-carrier injection to it.

Here, we present a numerical modeling of the TC and BC OFETs by 2-D finite element simulation (ATLAS). A particular interest is to understand the fundamental difference of each device structure. We are able to rule out any process-related or morphological effects on the device properties, because the semiconductor is considered as a continuous medium and all metal/organic interfaces are sharply defined in 2-D models. Therefore, the results provide a purely theoretical description of the physics of each device type.

Figure 5.10 shows the 2-D BC and TC OFETs defined in ATLAS. One hundred nanometers of pentacene is the organic semiconducting layer and 300 nm of SiO_2 is for the gate dielectric. The channel length L is fixed at 30 μm and the length of the source and drain electrodes is also 30 μm. All the three electrodes are assumed to be infinitely thin, thus no physical thickness value is inserted. Note that the origin of the geometrical coordinates (0, 0) is located at the starting point of the channel at the source side. Table 5.2 lists the basic setup parameters used for the numerical simulation. The predefined pentacene model in the ATLAS library was selected with a modification of the dielectric constant by the value estimated in Section 4.1. In order to analyze the effect of traps, a comparison of the trap-free case and

Table 5.2: List of the setup parameters used for the ATLAS simulation.

Parameter	Value
Temperature	300 K
Pentacene ionization potential	5.2 eV
Pentacene electron affinity	2.8 eV
Pentacene valence band effective DOS	10^{20} cm^{-3}
Pentacene p-doping concentration	0 cm^{-3}
Pentacene dielectric constant	3.6
Pentacene hole mobility	0.5 cm^2/V·s
SiO$_2$ dielectric constant	3.9
Gate work function (Al)	4.2 eV
Source/drain work function (Au)	4.9 eV

the exponential trap DOS was also made in addition to the geometrical comparison. The additionally used trap parameters are the total trap density (N_t) of 10^{18} cm^{-3} and the trap characteristic temperature (T_c) of 600 K.

We first extracted characteristic potential profiles of the simulated OFETs under the same operating condition of $V_G = -20$ V and $V_D = -2$ V. Linear-regime operation is expected because $|V_G| \gg |V_D|$. Figure 5.11 shows the calculated potential profiles along x direction from the four simulated structures; BC/TC OFETs with/without traps. Each panel contains two profiles, one estimated at the channel ($y = 0.001$ μm, solid line), and the other one at the top surface of the semiconductor ($y = 0.099$ μm, dotted line). Remarkably, it appears that there is a distinctive difference between BC and TC OFETs. We see a substantial voltage drop ($\sim$ -0.4 V) at the source edge in BC OFETs, whereas the whole -2 V of V_D is linearly distributed along the channel in TC OFETs. Note that the simulated potential profiles are in good agreement with the scanning Kelvin probe microscopy (SKPM) data in the literature, which also revealed a noticeable contact voltage drop in the case of BC OFETs [138, 141]. The contact voltage drop in the BC OFETs is evidence for the contact resistance R_c, as explained by Ohm's law. Another finding is that the channel potential profile is slightly lower than the surface potential profile in TC OFETs. This corresponds to a voltage drop along the y-axis, which is attributed to the bulk resistivity of the semiconductor. This is because in TC OFETs, charge injection occurs at the top surface, and charges carriers have to transport though the bulk film until they reach the channel. In both BC and TC OFETs, the effect of traps on the potential profiles is marginal even though trapped charges are supposed to influence the electrostatic distribution.
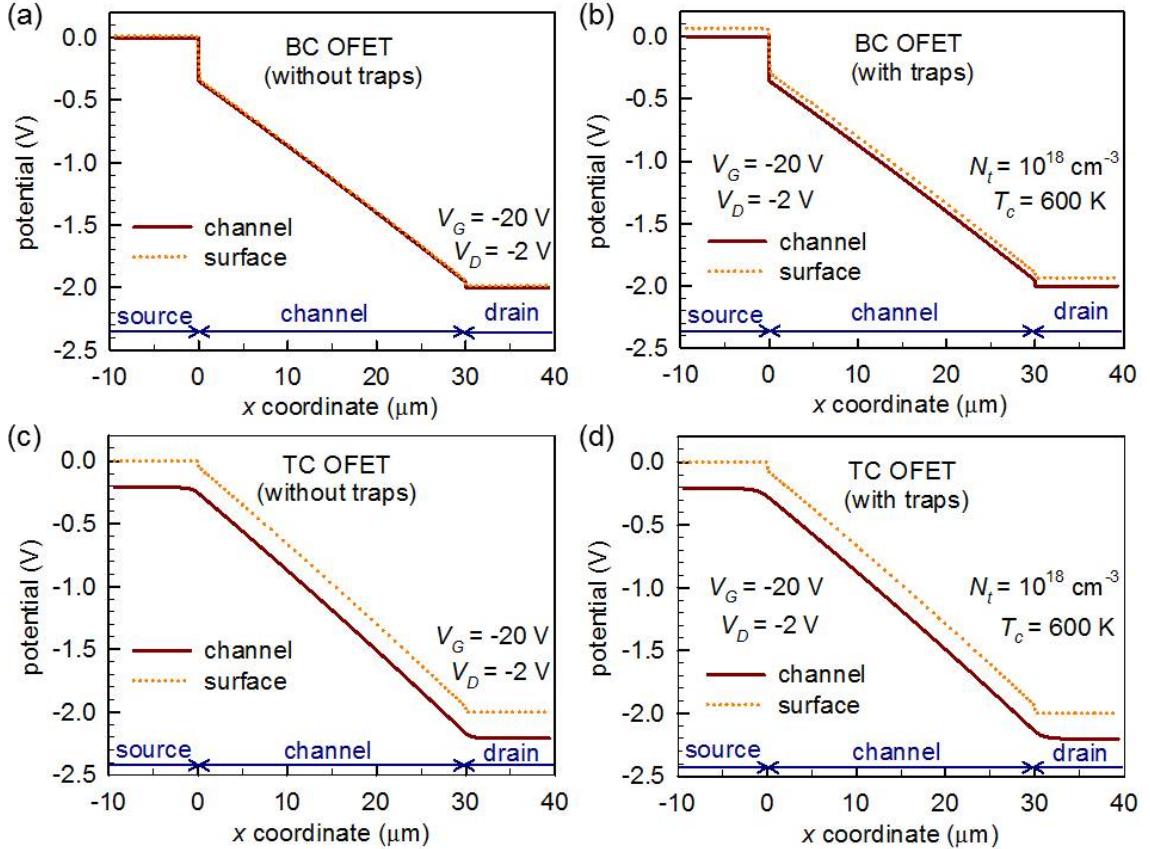
Figure 5.11: Simulated potential profiles in BC/TC OFETs with/without existence of trap states. Upon the assumption of the equipotential channel at $V_D = 0$ V, all extracted potential profiles are corrected with the reference profile at $V_D = 0$ V.

Our simulated potential profiles have significant importance because they clearly show that there should be a 'theoretical' reason that gives rise to a contact resistance, and corresponding contact voltage drop in BC OFETs. In order to understand the origin of this dissimilar contact feature in two geometries, we estimated the charge-carrier distribution inside the organic layer in the same operating condition ($V_G = -20$ V and $V_D = -2$ V). In Figure 5.12, the results are drawn as 3-D mesh plots, in which both the height and the color represent the hole concentration. For a proper interpretation, one should keep in mind that the carrier density at the metal/semiconductor interface is dictated by Boltzmann statistics so that the hole concentration at the source and drain electrodes (p_s and p_d) is expected to follow the equation

$$p_s = p_d = N_v \exp(-E_b/k_B T), \tag{5.1}$$

which is strongly dependent on the injection barrier E_b, but independent of V_G and V_D. We can calculate by Equation (5.1) using $E_b = 0.3$ eV and $N_V = 10^{20}$ cm^{-3} from
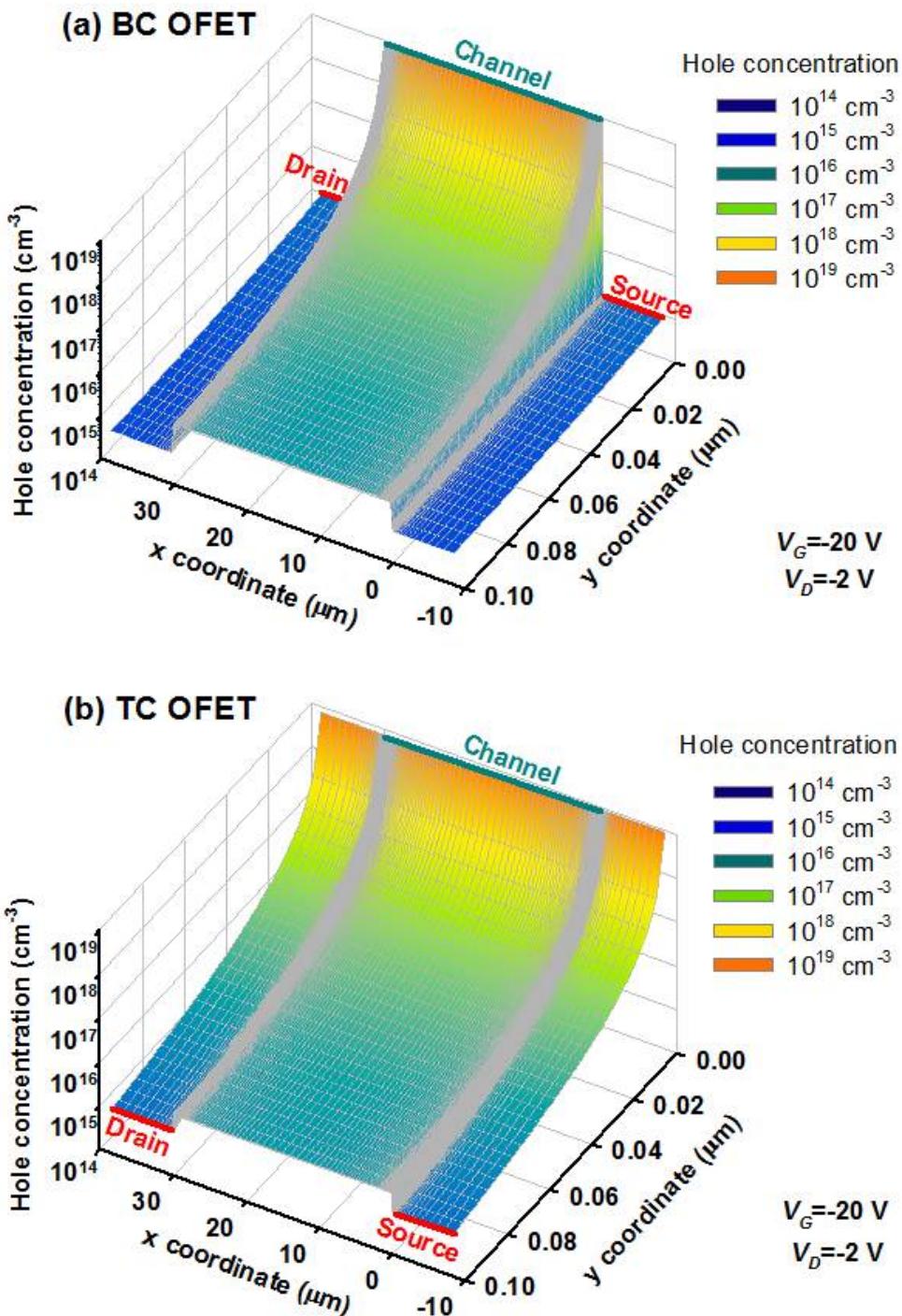
Figure 5.12: Charge-carrier distribution in the semiconductor xy plane of (a) BC OFET and (b) TC OFET (trap-free case).

Table 5.2. The result is $p_s = p_d = 9.7 \times 10^{14}$ cm^{-3}, which well matches the numerically simulated values at the electrode edges in both geometries in Figure 5.12. By contrast, the hole concentration along the channel p_{ch} is controlled by capacitive effect, and we can write its dependence on V_G as

$$p_{ch} = \frac{Q_{ch}}{qt_{ch}} = \frac{C_i|V_G - V_T|}{qt_{ch}}. \tag{5.2}$$

Here, Q_{ch} is the channel charge density per unit area, t_{ch} the effective channel thickness, C_i the insulator capacitance per unit area, and V_T the threshold voltage. It should be noted that Equation (5.2) is a rough approximation based on the assumption that the gate-induced charges are uniformly distributed over the accumulation layer defined by the thickness t_{ch}. At this point, the usefulness of this equation is to emphasize the strong dependence of p_{ch} on V_G and also to show that $p_{ch} \gg p_s$ under normal operation. The simulated p_{ch} is 8.0×10^{18} cm^{-3}, and the estimated t_{ch} is 1.6 nm, which is in accordance with other theoretical estimations [142].

Figure 5.12 shows that, in BC OFETs, the holes must be injected into the channel through a narrow transition zone where the hole density abruptly increases from p_s to p_{ch}. As the local conductivity is proportional to the carrier density , and because p_s is orders of magnitude lower than p_{ch}, this transition zone is highly resistive and gives rise to an R_c zone at the source contact. The situation is totally different in TC OFETs. Here, the semiconductor is always in contact with the insulator, so there is a nearly perfect continuity of the hole concentration at both ends of the channel. This is coherent with the channel potential profile in Figure 5.11 without any contact voltage drop in TC OFETs. With traps, the overall hole density is slightly reduced due to the trapped charges, but the same contrast between two structures is observed.

Finally, the calculated current-voltage characteristics are shown in Figure 5.13, which shows that the differentiated microscopic picture is in good agreement with the electrical performance of the devices. In Figure 5.13 (a), two E_b values were used to accentuate the contrast between BC and TC OFETs. TC OFETs follow nearly ideal I-V relationship where I_D is linearly modulated by V_G and E_b does not play any critical role. The current in BC OFETs, however, is strongly contact-limited, as indicated by the downward bending of the transfer curves. Moreover, only a slight increase in E_b results in a considerable reduction of the current. The shape of the two BC transfer curves is close to the results in [143], where a constant-R_c model is suggested;

$$I_D = \frac{-\frac{W}{L}\mu C_i(V_G - V_T)V_D}{1 - \frac{W}{L}\mu C_i(V_G - V_T)R_c}. \tag{5.3}$$
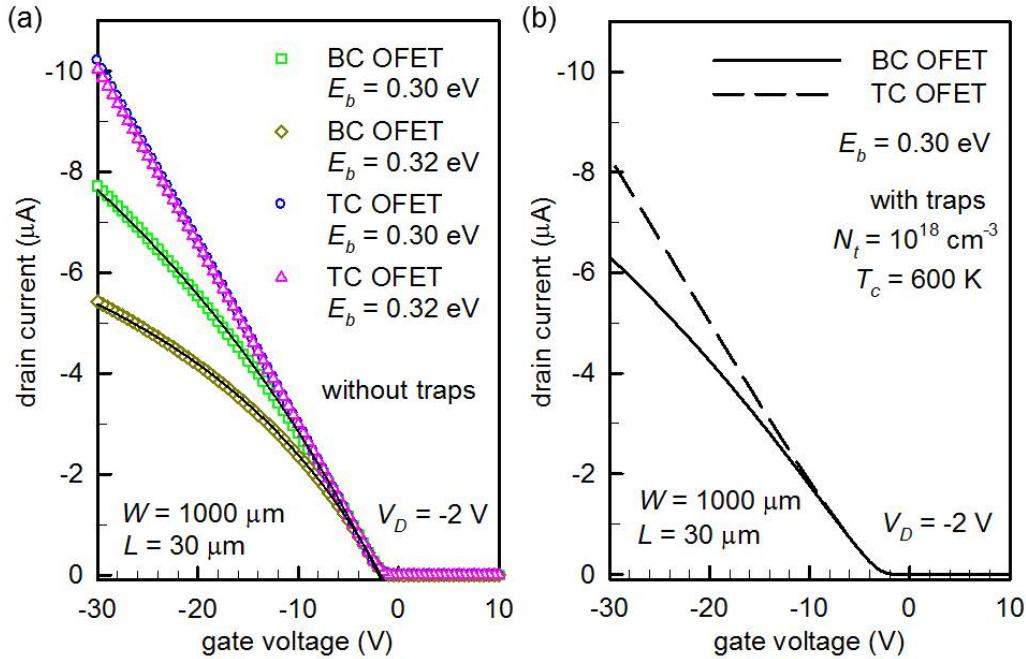
Figure 5.13: (a) Simulated transfer characteristics of the trap-free BC and TC OFETs with two different injection barrier heights. (b) Simulated transfer curves with exponential trap DOS.

The solid lines overlapped in Figure 5.13 (a) are fits to this model. From the fitting, the extracted R_c is 8.5×10^4 Ω for $E_b = 0.30$ eV and $R_c = 1.8 \times 10^5$ Ω for $E_b = 0.32$ eV. In comparison with Figure 5.13 (a), Figure 5.13 (b) shows that introducing traps results in a significant decrease of the field-effect mobility and a negative shift of the threshold voltage in both OFETs. Traps reduce the density of free charge carriers, and more negative V_G is required to induce a conductive channel [143,144]. Note that the TC architecture keeps its advantage over the BC OFET even with traps, because the channel hole distribution remains continuous.

5.2.2   Coplanar OFET model: Charge distribution

The above simulation study addressed the fundamental difference between the staggered and the coplanar geometries. After this first step, we focused on the modeling of the coplanar OFETs. There are already several theoretical models for the contact resistance in staggered OFETs, which are generally based on the current crowding mechanism [145] that describes the bulk film resistance as the access or contact resistance [135, 146–148]. However, a specific model is necessary for coplanar OFETs, in which R_c does not stem from the bulk resistance, but rather from the carrier-density
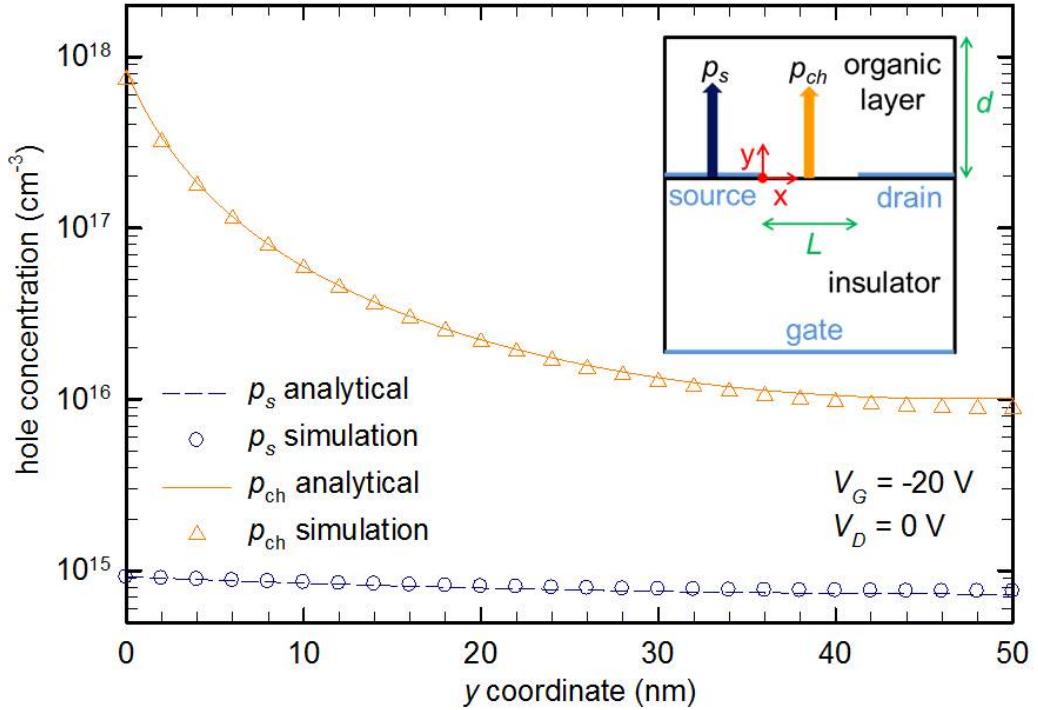
Figure 5.14: Charge distribution inside the organic semiconductor of the model transistor. Inset shows the 2-D device structure with the notations for the geometrical dimensions, mathematical coordinates, and conventions for the distribution functions (p_s and p_{ch}).

bottleneck zone due to the direct influence of the finite injection barrier.

A cross-sectional view of the coplanar model OFET is shown in Figure 5.14. Based on the simulation result in Figure 5.12 (a), we denote the characteristic charge distribution function at the source p_s and the channel p_{ch} along the thickness direction y. Here, we develop analytical expressions for $p_s(y)$ and $p_{\text{ch}}(y)$. From the absence of thermal carriers in the organic semiconductor (Section 4.1), we make the basic assumption that the OFET current is entirely due to the injected charge. We first revisit the classical theories on the metal/insulator junction and suggest an approximate solution for analytical development.

At this point, for simplicity, we do not refer to the OFET geometry but only imagine a 1-D insulator (or undoped semiconductor) in contact with a charge reservoir at $y = 0$. It extends toward the positive y-direction up to $y = d$. The electrostatic distribution can be estimated using the same approach as that was proposed for the analytical modeling of the organic diode in Section 4.1. Here, we only change the direction of interest to y and rewrite the merged one dimensional Poisson's and

drift-diffusion equation [Equation (4.5)] as

$$J = \epsilon_s \mu \left(F \frac{\mathrm{d}F}{\mathrm{d}y} - \frac{k_B T}{q} \frac{\mathrm{d}^2 F}{\mathrm{d}y^2} \right), \tag{5.4}$$

which is the fundamental equation of the given physical system to be solved. At thermal equilibrium, the net current is zero (the drift current and the diffusion current compensate each other) so that

$$F \frac{\mathrm{d}F}{\mathrm{d}y} - \frac{k_B T}{q} \frac{\mathrm{d}^2 F}{\mathrm{d}y^2} = 0. \tag{5.5}$$

This can be integrated once to

$$\left(\frac{q}{2k_B T} \right)^2 F^2 - \frac{q}{2k_B T} \frac{\mathrm{d}F}{\mathrm{d}y} = -g^2, \tag{5.6}$$

where g is an integration constant.

Mott and Gurney first derived the solution of Equation (5.6) for a semi-infinite semiconductor ($d \to \infty$) [98]. In this case, both $F(y)$ and $\mathrm{d}F/\mathrm{d}y$ go to zero when $y \to \infty$, so that $g = 0$ and Equation (5.6) reduces to

$$F^2 - \frac{2k_B T}{q} \frac{\mathrm{d}F}{\mathrm{d}y} = 0. \tag{5.7}$$

The solution for the electric field is reached by separating variables,

$$F(y) = \left(-\frac{2k_B T}{q y_0} \right) \left(\frac{1}{1 + y/y_0} \right) = \frac{F_0}{1 + y/y_0}, \tag{5.8}$$

where y_0 is another integration constant. The hole distribution $p(y)$ is given by the first derivative of $F(y)$;

$$p(y) = \left(\frac{2\epsilon_s k_B T}{q^2 y_0^2} \right) \left(\frac{1}{1 + y/y_0} \right)^2 = \frac{p_0}{(1 + y/y_0)^2}. \tag{5.9}$$

F_0 and p_0 are the electric field and the hole concentration at the junction ($y = 0$), respectively. Equations (5.8) and (5.9) are intended to underline the physical meaning of y_0, which is viewed as a characteristic length over which the boundary value (F_0 or p_0) is distributed from the junction interface. The value of y_0 can be determined from the boundary value of either F_0 or p_0. For the following discussion, a relationship between y_0 and p_0 is particularly useful. From Equation (5.9), we have

$$y_0 = \sqrt{\frac{2\epsilon_s k_B T}{q^2 p_0}} \tag{5.10}$$

meaning that, the higher the initial carrier density p_0 is, the smaller y_0. If y_0 is small, the carriers are densely concentrated at the junction and do not spread far away from the injecting surface. Even though the Mott-Gurney model provides meaningful insight into the charge distribution, its usage should be limited to very thick organic crystals and this model cannot be safely applied to thin organic films.

Skinner stepped forward and developed more general solutions to Equation (5.6) [100]. It means that one can challenge the 'finite' junction without forcing g to zero. The author actually separated the cases by the sign of the integration constant and obtained separate sets of solutions depending on this sign. An essential boundary condition for the finite semiconductor is $F(d) = 0$ because there cannot be any current flowing into or out of the semiconductor at the surface $y = d$. The injected holes (positive charges) make the only contribution to the space charge in Poisson's equation. Consequently, the sign of dF/dy is always positive through the whole semiconductor thickness. In other words, $F(0)$ is negative and $F(y)$ approaches zero from $y = 0$ to $y = d$. At $y = d$, F becomes zero by the boundary condition and dF/dy remains positive. Therefore, the right-hand term in Equation (5.6) is negative and the corresponding solution is a trigonometric function, which can be written as

$$F(y) = -\frac{q p_0 g y_0^2}{\epsilon_s} \cot(gy + \arcsin gy_0), \qquad (5.11)$$

$$p(y) = \frac{p_0 g^2 y_0^2}{\sin^2(gy + \arcsin gy_0)}. \qquad (5.12)$$

Here, p_0 always represents the hole concentration at $y = 0$ and Equation (5.10) remains valid. In order to estimate the constant g, we introduce the boundary condition $F(d) = 0$. From Equation (5.11), this gives

$$\cot(gd + \arcsin gy_0) = 0, \qquad (5.13)$$

which can be further simplified by using trigonometric identities, resulting in

$$gy_0 = \cos gd. \qquad (5.14)$$

By putting Equation (5.14) into Equation (5.12), we can write

$$p(y) = \frac{p_0 \cos^2 gd}{\cos^2 g(d-y)}, \qquad (5.15)$$

where $0 \leq y \leq d$.

A limitation to Skinner's approach emerges at this point. Although this model gives exact solutions for thin-film cases, Equation (5.14) does not lead to an analytical expression for g and, consequently, the final solution requires numerical computation.

Now, we return to the OFET structure in Figure 5.14 and define the boundary condition for p_s and p_{ch}. The carrier density at a metal/semiconductor interface is dictated by Boltzmann's statistics so that p_{s0} (the source carrier density at $y = 0$) is strongly injection-limited following

$$p_{s0} = N_v \exp\left(-\frac{E_b}{k_B T}\right),\tag{5.16}$$

where N_v is the effective density of states at the HOMO edge. The hole barrier height E_b corresponds to the energy difference between the electrode Fermi level and the semiconductor HOMO level. The channel carriers, on the other hand, are induced by the gate capacitance and can be estimated by

$$Q_{ch} = C_i |V_G - V_T| = q \int_0^d p_{ch}(y)\mathrm{d}y,\tag{5.17}$$

where Q_{ch} is the total channel charge per unit area, C_i the insulator capacitance per unit area, and V_T the threshold voltage. The functional form of $p_{ch}(y)$ will be derived below but it is helpful to know the boundary value already here. The channel hole concentration at $y = 0$ is approximate to

$$p_{ch0} \approx \frac{Q_{ch}^2}{2\epsilon_s k_B T} = \frac{C_i^2 |V_G - V_T|^2}{2\epsilon_s k_B T}.\tag{5.18}$$

The characteristic distribution lengths for the source and the channel charges are defined by Equation (5.10), thus $y_{s0} = \sqrt{2\epsilon_s k_B T/q^2 p_{s0}}$ and $y_{ch0} = \sqrt{2\epsilon_s k_B T/q^2 p_{ch0}}$ respectively.

We can infer from Equations (5.16) and (5.18) that E_b and V_G are the principal parameters for the source and channel distribution of charges. The results presented in Figure 5.15 support this statement and give another important implication for the model. Figure 5.15 shows the results calculated by Equations (5.16) and (5.18) with $N_v = 10^{20}$ cm^{-3}, $T = 300$ K, $\epsilon_s = 3.6 \times \epsilon_0$, $C_i = 2.3$ nF/cm^2, and $V_T = 0$ V (ϵ_0 is the permittivity of vacuum). At variance with the charge distribution in staggered OFETs in which the gate-induced charges are evenly distributed over the whole semiconductor/insulator interface, here p_{s0} is much lower than p_{ch0} due to the high injection barrier. Another key feature of Figure 5.15 is that y_{s0} normally exceeds the thickness of an organic thin-film, whereas y_{ch0} is far smaller than the film thickness. This finding enables an independent modeling of $p_s(y)$ and $p_{ch}(y)$ by means of an approximation method.
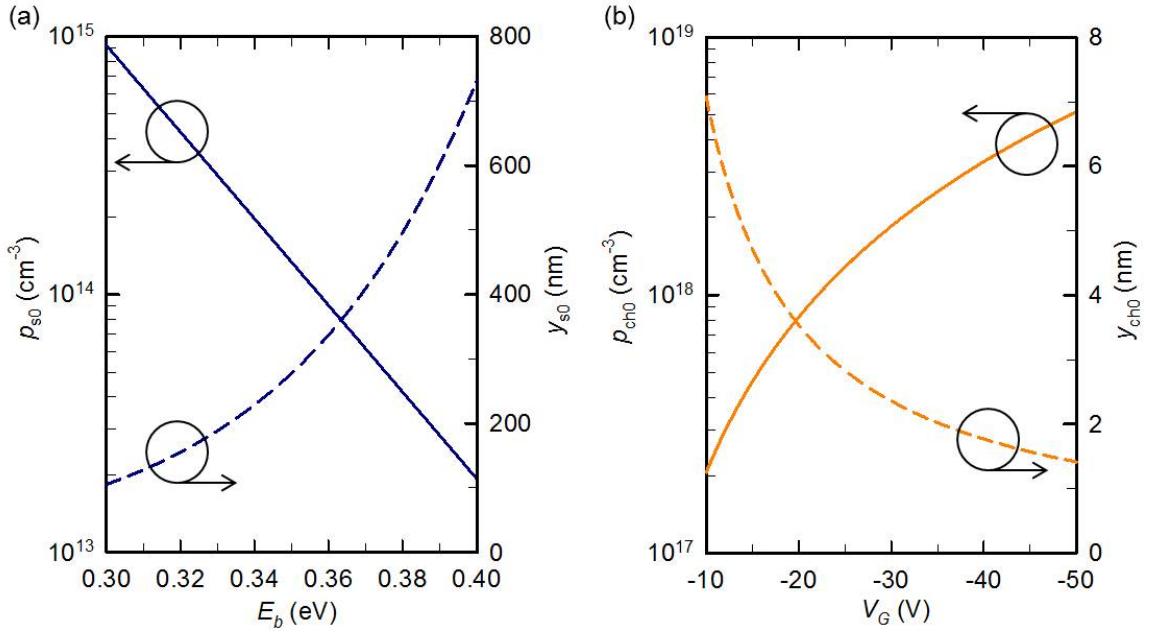
Figure 5.15: (a) Source distribution factors (p_{s0} and y_{s0}) as a function of E_b and (b) channel distribution factors (p_{ch0} and y_{ch0}) as a function of V_G. The solid lines indicate the initial hole concentrations and the dashed lines correspond to the distribution lengths.

The main idea is to develop an analytical form of Equation (5.15) by approximating the cosine function in Equation (5.14). A linear (or a first-order) approximation of any given function $f(z)$ is defined at the vicinity of $z = a$ by

$$f(z) \approx f(a) + f'(a)(z - a). \tag{5.19}$$

If $f(z) = \cos z$, we get

$$\cos z \approx \cos a + (-\sin a)(z - a). \tag{5.20}$$

First, for the source carriers $p_s(y)$, we rewrite Equation (5.14) as

$$g_s y_{s0} = \cos g_s d, \tag{5.21}$$

where the subscript 's' refers to the 'source'. Because $y_{s0} \gg d$, we can approximate $\cos g_s d$ where $g_s d$ is close to zero. Under this condition, we can say

$$g_s y_{s0} = \cos g_s d \approx 1, \tag{5.22}$$

and therefore

$$g_s \approx \frac{1}{y_{s0}}. \tag{5.23}$$

Then if we use Equation (5.23) to replace g, Equation (5.15) finally changes into

$$p_s(y) = p_{s0} \frac{\cos^2\left(\frac{d}{y_{s0}}\right)}{\cos^2\left(\frac{d-y}{y_{s0}}\right)}. \tag{5.24}$$

Next, another approximation is needed for the channel carriers $p_{ch}(y)$. Starting again from Equation (5.14),

$$g_{ch} y_{ch0} = \cos g_{ch} d, \tag{5.25}$$

where the subsrcipt 'ch' refers to the 'channel'. This time, $y_{ch0} \ll d$ so that $\cos g_{ch} d$ should be developed near $g_{ch} d = \pi/2$. Referring to Equation (5.20), we get

$$g_{ch} y_{ch0} = \cos g_{ch} d \approx \frac{\pi}{2} - g_{ch} d, \tag{5.26}$$

and

$$g_{ch} \approx \frac{\pi}{2(d + y_{ch0})}. \tag{5.27}$$

The channel carrier distribution function $p_{ch}(y)$ is now given from Equations (5.15) and (5.27), after some manipulation steps, by

$$p_{ch}(y) = p_{ch0} \frac{\sin^2\left(\frac{\pi}{2}\frac{y_{ch0}}{d}\right)}{\sin^2\left(\frac{\pi}{2}\frac{y_{ch0}+y}{d}\right)}. \tag{5.28}$$

Now one can reexamine the integration in Equation (5.17) and see that Equation (5.18) is correct under the condition that $y_{ch0} \ll d$.

It is worth emphasizing here that our approximate model [Equations (5.24) and (5.28) with Equations (5.16) and (5.18)] provides analytical expressions that explicitly contain the thickness parameter d. It means that this strategical development overcomes the limitation of the two classical models and assures its general applicability to the thin film-based OFETs. Figure 5.14 shows the reliability of the approximate solutions. The parameters used here in both the analysis and the simulation are those listed above for Figure 5.15 with $d = 50$ nm, $E_b = 0.3$ eV, and $V_G = -20$ V. It is shown that the analytical model predicts the numerical simulation results with satisfying precision.

5.2.3 Coplanar OFET model: Contact resistance

Here we propose a charge-based contact resistance model for coplanar OFETs. The model stems from the fact that there is an abrupt transition of the hole concentration at $x = 0$ due to the huge difference between $p_s(y)$ and $p_{ch}(y)$. It is this carrier-density transition zone that accounts for the physical origin of R_c because the mean
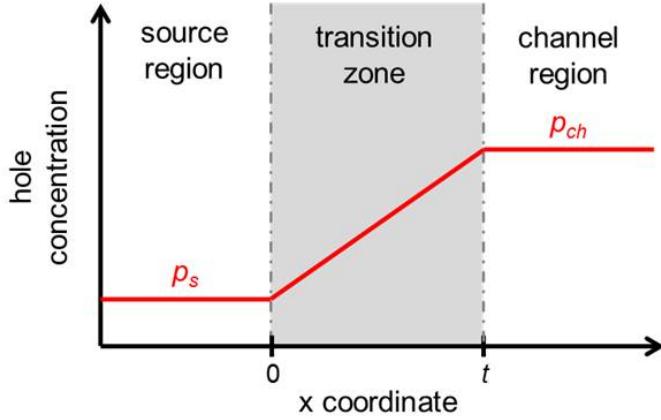
Figure 5.16: Conceptual representation of the hole concentration near the transition zone that is located from $x = 0$ to $x = t$, which accounts for the contact resistance in coplanar OFETs.

hole concentration in this zone is much lower than that in the conducting channel, due to the effect of p_s penetrating into the channel region. Figure 5.16 shows this source/channel interface where two independent distribution functions overlap. There exist concentration tails along the x-direction characterized by the Debye length of the channel carriers (x_{ch}) and that of the source carriers (x_s). They are defined by $x_{ch} = \sqrt{\epsilon_s k_B T / q^2 p_{ch}}$ and $x_s = \sqrt{\epsilon_s k_B T / q^2 p_s}$. Because $p_{ch} \gg p_s$, $x_{ch} \ll x_s$ and we can neglect the contribution of x_{ch} so that the the transition from p_s to p_{ch} can be simplified to a single exponential function

$$p(x) = p_s \exp\left(\frac{x}{x_s}\right), \tag{5.29}$$

Then the thickness t of the transition zone in Figure 5.16 is estimated by

$$p(t) = p_s \exp\left(\frac{t}{x_s}\right) = p_{ch}, \tag{5.30}$$

$$t = x_s \ln\left(\frac{p_{ch}}{p_s}\right). \tag{5.31}$$

The contact resistance R_c is calculated from an estimation of the average hole concentration in the transition zone (or R_c zone), done by integrating the local conductivity over the entire thickness. Keeping this approach in mind, the mean hole concentration p_m throughout the R_c zone can be defined by

$$p_m = \frac{1}{t} \int_0^t p(x) \mathrm{d}x = \frac{p_s}{t} \int_0^t \exp\left(\frac{x}{x_s}\right) \mathrm{d}x, \tag{5.32}$$

where Equation (5.29) is used. By inserting Equations (5.30) and (5.31) and using $p_{ch} \gg p_s$, we get

$$p_m = \frac{p_{ch} - p_s}{\ln(p_{ch}/p_s)} \approx \frac{p_{ch}}{\ln(p_{ch}/p_s)}, \tag{5.33}$$

which shows that the balance between p_s and p_{ch} determines the average concentration and p_m is also y-dependent. Now we can calculate the elemental conductance $\mathrm{d}G_c$ of the volume element delimited by W (channel width), $t(y)$, and $\mathrm{d}y$

$$\mathrm{d}G_c = q\mu W \frac{p_m(y)}{t(y)} \mathrm{d}y, \tag{5.34}$$

where the hole mobility μ is assumed to be constant at this moment. R_c is finally obtained, by replacing $t(y)$ and $p_m(y)$ using Equations (5.31) and (5.33),

$$R_c = \frac{1}{G_c} = \frac{\sqrt{\epsilon_s k_B T}}{q^2 \mu W} \left[\int_0^d \frac{p_{ch}(y)\sqrt{p_s(y)}}{[\ln(p_{ch}(y)/p_s(y))]^2} \mathrm{d}y \right]^{-1}. \tag{5.35}$$

Note that, by Equation (5.35), it is possible to predict the exact value of R_c when the distribution functions for $p_s(y)$ and $p_{ch}(y)$ are known.

Numerically calculated R_c values are plotted in Figure 5.17 with varying V_G and E_b. The charge-distribution functions [$p_s(y)$ and $p_{ch}(y)$] developed in Section 5.2.2 were inserted in Equation (5.35). All fixed parameters are summarized in the caption to Figure 5.17. We can state, from this result, that the theoretical charge-based model well predicts the decrease of R_c with increasing $|V_G|$, which is often experimentally observed, though not readily understood in the case of coplanar OFETs [149–152]. Furthermore, it can be inferred that the degree of dependency between V_G and R_c is accentuated with higher injection barriers. Finally, it should be noted that the hole mobility μ is considered constant here, which restricts the analysis to defect-free, highly pure crystalline semiconductors [153]. When trap states exist, μ should be regarded as the 'effective' mobility determined by the ratio of free to total carrier density. This results in a dependence of the measured mobility on the gate voltage as will be discussed below.

5.2.4   Coplanar OFET model: Experimental analysis

In order to investigate the validity of the R_c model, we analyzed experimental data from the fabricated pentacene coplanar OFETs. Figure 5.18 shows the electrical performance of a representative transistor with the corresponding device structure.
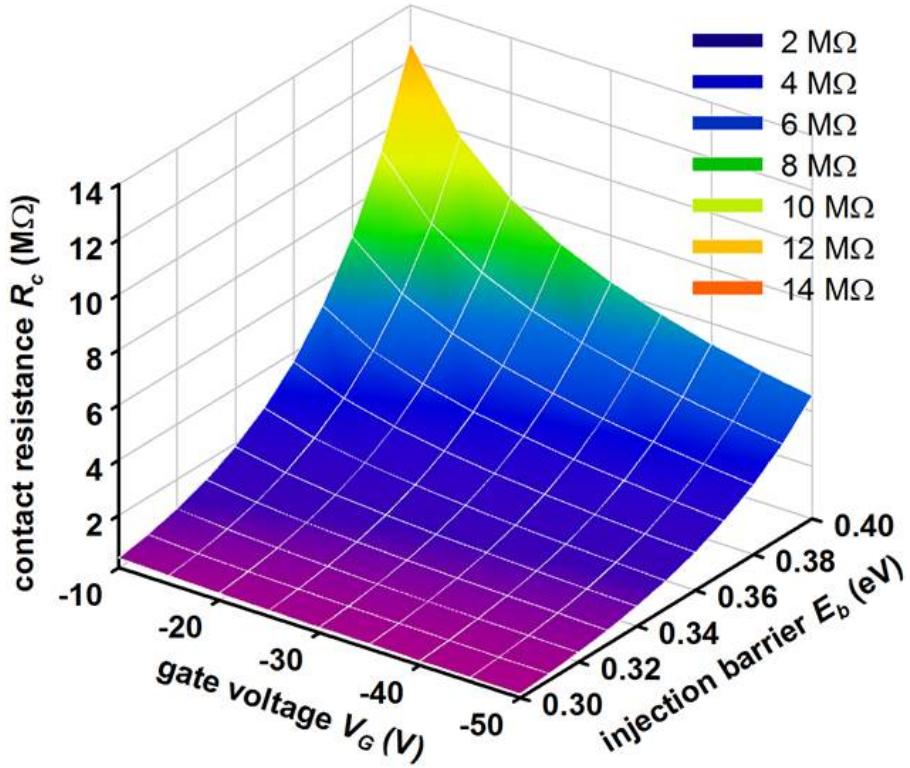
Figure 5.17: R_c determined by Equation (5.35) with a variation of V_G and E_b. The fixed parameters are as follows; $N_v = 10^{20}$ cm^{-3}, $T = 300$ K, $\epsilon_s = 3.6 \times \epsilon_0$, $C_i = 2.3$ nF/cm^2, $V_T = 0$ V, $d = 50$ nm, $W = 500$ μm, and $\mu = 0.2$ cm^2/V·s.

Especially, the slight upward bending of the output curves at low $|V_D|$ is direct evidence for a nonlinear parasitic contact effect [150]. Hence, it is predicted that R_c actually contribute to the current in the fabricated device.

The transmission-line method (TLM) is a widely-used technique for the extraction of R_c from I-V data [154–156]. It is assumed that the source-to-drain current path is equivalent to a series combination of contact resistance R_c and channel resistance R_{ch} (inset in Figure 5.19). The TLM is also strongly based on the assumption that R_c is not a function of L but R_{ch} is proportional to L [157]. At low $|V_D|$ (linear regime), the relationship between I_D and V_D of this circuit can be expressed as

$$I_D = \frac{V_D}{R_{on}} = \frac{V_D}{R_c + R_{ch}} = \frac{V_D}{R_c + \left[\frac{W}{L}\mu C_i |V_G - V_T|\right]^{-1}}, \tag{5.36}$$

where the linear-regime channel conductance is used to estimate R_{ch}. R_{on} is the on-state resistance that can be directly obtained from measured V_D and I_D by

$$R_{on} = \frac{V_D}{I_D} = R_c + \frac{L}{W \mu C_i |V_G - V_T|}. \tag{5.37}$$
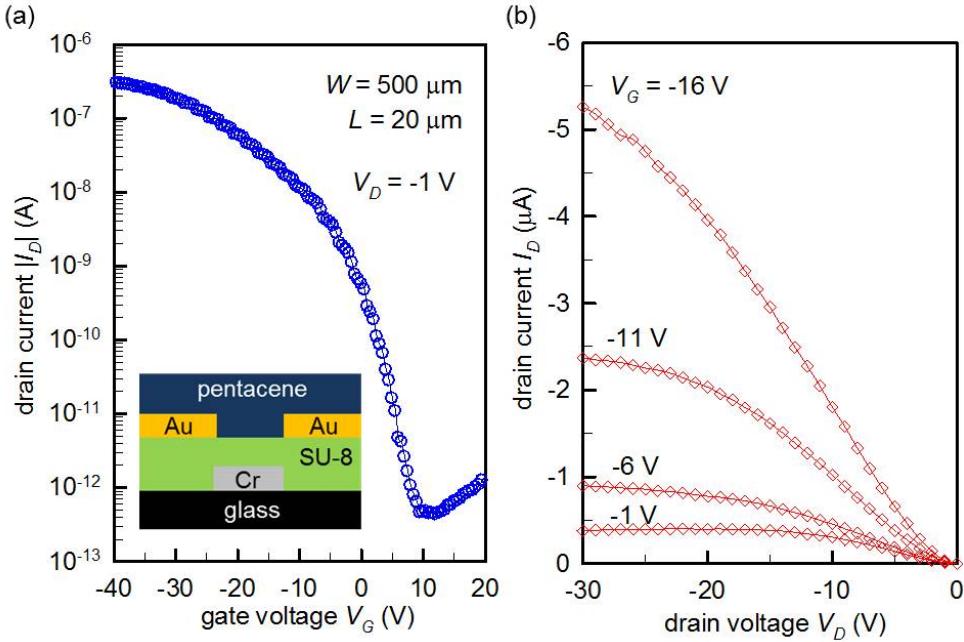
Figure 5.18: Measured electrical performance of a pentacene transistor fabricated with the bottom-gate bottom-contact geometry. (a) Transfer characteristic and (b) output characteristics. The inset of (a) is the device structure.
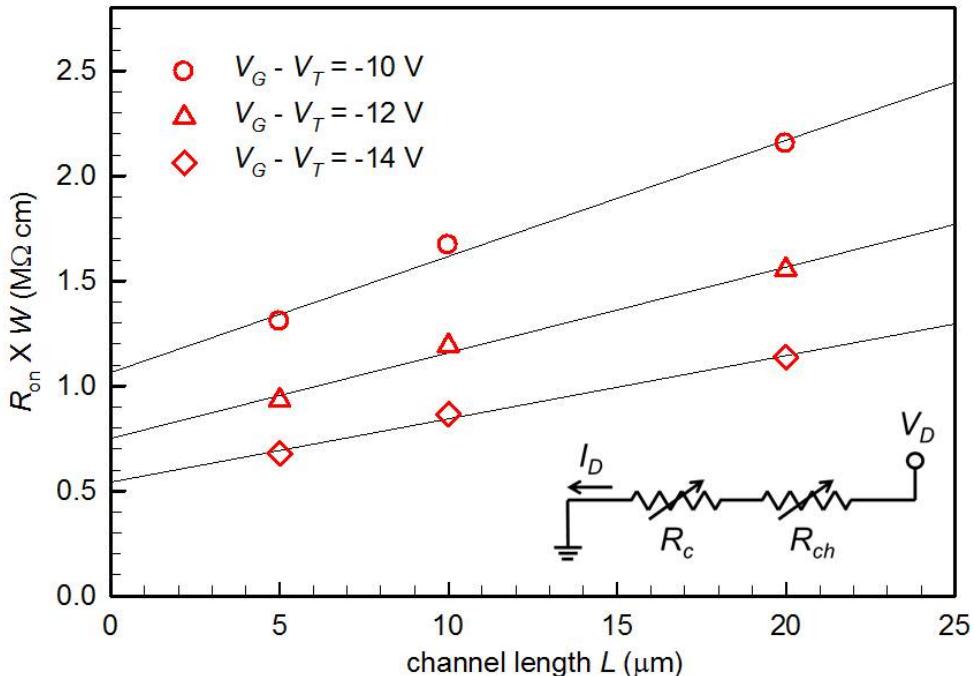
Figure 5.19: $R_{on}W$ versus L plot for the transmission-line method (TLM). The inset is the equivalent circuit of the on-state conduction path that consists of a series connection of the contact and channel resistances. Note that R_c and R_{ch} are drawn as variable resistors because both of them are supposed to be V_G-controlled.
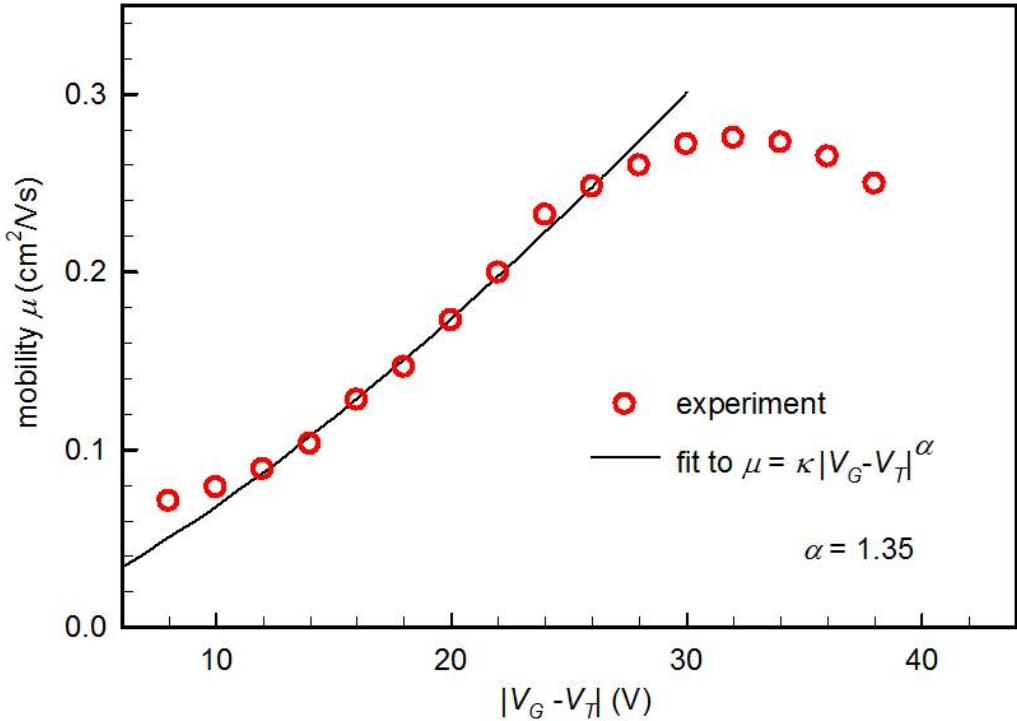
Figure 5.20: Hole mobility as a function of $|V_G - V_T|$ extracted by the TLM. The solid line is a fit to the trap-filling model at low $|V_G|$. The decrease in the mobility at higher $|V_G|$ can be attributed to the field-induced mobility degradation.

Width-normalized resistance is more practical for the purpose of comparing device sets with different W so it is useful to multiply Equation (5.37) by W and get

$$R_{on} \times W = R_c \times W + \frac{L}{\mu C_i |V_G - V_T|}. \tag{5.38}$$

To apply the TLM, we first draw $R_{on}W$ versus L and extrapolate the linear regression line to zero L to read the $R_c W$ value. Figure 5.19 shows the experimental data on pentacene OFETs. The deviation of the data points from the regression lines is minimal and it makes sure that the fabricated OFETs well satisfy the basic assumptions of the TLM. It is clear that R_c decreases with increasing $|V_G - V_T|$ as the intercept to the vertical axis moves downward. V_T for those three transistors were evaluated from the saturation current and no significant variation was observed so that we can use an average V_T of -4 V. Although not often mentioned, it is important to note here that the TLM can also be used to estimate μ as a function of $|V_G - V_T|$ because the 'slope' of the regression line usually varies with V_G and this slope contains the parameter μ by Equation (5.38).

The extracted hole mobility μ as a function of $|V_G - V_T|$ is shown in Figure 5.20, which indicates that the variation of μ is significant and does not follow a simple monotonous behavior. We infer that the two distinct regimes are dominated by two different mechanisms. First, the rise in μ at low $|V_G|$ can be adequately described by the gradual filling of trap states as the Fermi level at the semiconductor/insulator interface approaches the transport orbital (HOMO in the case of p-type materials). This is reasonable because a polycrystalline pentacene film contains a substantial number of trapping sites, most of which located at grain boundaries [158, 159]. We refer to the model in [53, 157] and fit the mobility in this regime ($|V_G - V_T| < 30$ V) to the equation

$$\mu = \kappa |V_G - V_T|^{\alpha}. \tag{5.39}$$

This model is based on the MTR (multiple trapping and release) process with an exponential density of states (DOS) near the band edge. The parameters κ and α are then related to the trap DOS. The exponent α is directly linked to the trap characteristic temperature T_c by $\alpha + 1 = (T_c/T)$. The extracted α is 1.35 in Figure 5.20 and the corresponding T_c is 705 K. If we convert this value into energy scale, the trap distribution width $E_t = kT_c$ is 61 meV, which is in good agreement with a recent review on the trap DOS in pentacene field-effect transistors [160]. Next, the slight decrease in μ at higher $|V_G - V_T|$ can be interpreted by the field-induced mobility degradation [130]. It is likely that the mobility near the insulator surface is lower than that at the bulk region due to various surface scattering agents. When $|V_G|$ becomes high enough, field-induced holes are more concentrated at this low-mobility near-insulator region so that the effective mobility through the conduction path is reduced.

Figure 5.21 shows how seriously the V_G-dependent mobility affects the charge-based R_c model. Here, the TLM-extracted R_c values are plotted as a function of $|V_G - V_T|$. As expected, R_c decreases rapidly with increasing $|V_G - V_T|$. We simply replaced μ in Equation (5.35) by Equation (5.39) and calculated R_c to compare with the experimental curve. Note that the entire curve in Figure 5.20 cannot be modeled by a simple analytical expression, so we only took the trap-dominated regime ($|V_G - V_T| < 30$ V) for the analysis in Figure 5.21. As mentioned above, V_G and E_b are the foremost parameters that govern R_c. Therefore, by optimizing the TLM-extracted curve with the model, we can successfully estimate the injection barrier E_b at the Au/pentacene interface in the fabricated OFETs. One can see that the model-calculated curve is in very good agreement with the experimental curve with E_b of 0.38 eV. When we
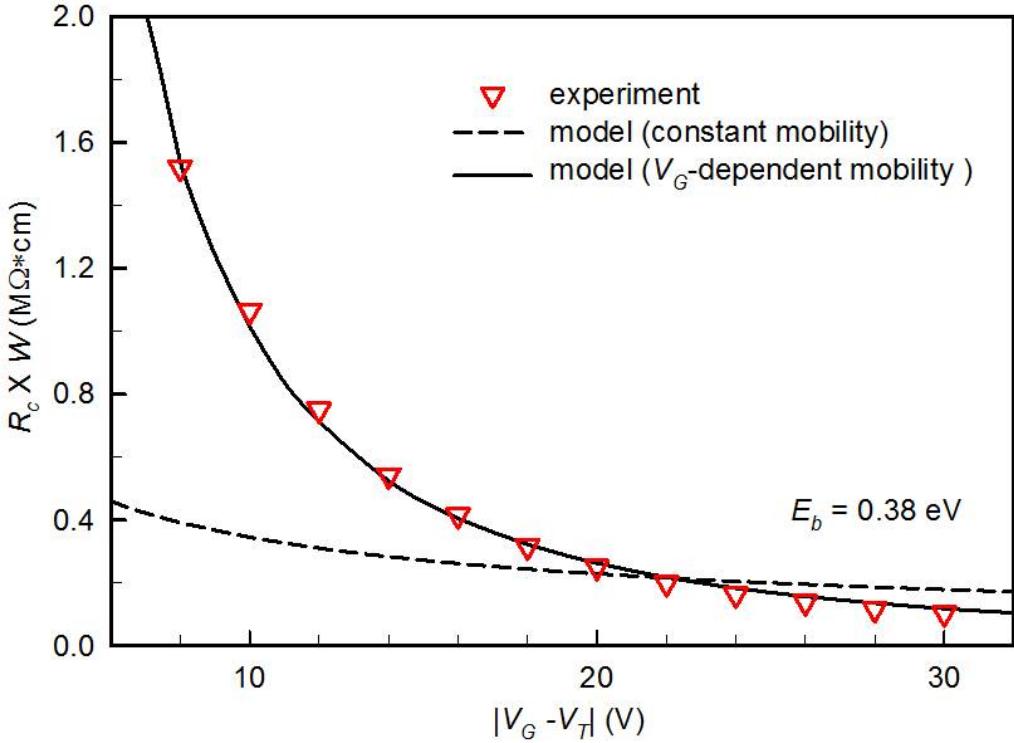
Figure 5.21: TLM-extracted $R_c W$ as a function of $|V_G - V_T|$ in comparison to the charge-based R_c model. Note that, if a constant mobility is assumed (here 0.2 cm^2/V·s), the V_G-dependence of R_c is underestimated. When we take the V_G-dependent mobility into account, the experimental results could be well fitted by the model.

calculated R_c with a constant mobility of 0.2 cm^2/V·s, however, the model cannot accurately predict the experimental results.

In the literature, there has been a question about how sometimes R_c is less sensitive to V_G or even assumed to be constant [143] while more often R_c is strongly dependent on V_G. For coplanar OFETs, our results can suggest two answers: First, the injection barrier E_b plays an important role on the dependence of R_c on V_G (Figure 5.17) thus the material combination of the metal and the semiconductor is basically crucial [57]. Second, V_G-dependent mobility can either intensify or diminish the slope of an R_c versus V_G curve, because μ can either increase or decrease (or even remain stable) with V_G, depending on various geometrical and/or electrical mechanisms [53, 130, 161, 162].

5.2.5 Compact modeling approach for OFETs

In this last part, we develop a compact modeling approach for compatibility with SPICE-based circuit simulation. The main focus is to describe a single analytical

expression that covers all operation regimes of OFETs. For the maximum universality, any geometry- or material specific consideration is given less importance at this stage. The following results have been obtained during the research visit at Tarragona, Spain, as a collaboration project with the group of Prof. Benjamin Iñiguez at Universitat Rovira i Virgili.

Here, we propose an improved model based on the unified model and parameter extraction method (UMEM) framework, which has been developed and applied to various thin-film transistor (TFT) technologies over the past years [163–166]. This new model features three major improvements: 1) A modified asymptotic function for the saturation behavior that also improves the output conductance in the linear regime, 2) a new subthreshold-current model, and 3) an extended range of application with the symmetry of source and drain electrodes. This model covers all operation regimes of OFETs from off- to on- state with a reasonable number of parameters and with smooth transition between the different regimes.

Figure 5.22(a) illustrates the concept of output asymptotes. In the ideal case, the drain current I_{DS} linearly increases at low drain voltage V_{DS} and becomes saturated at a constant level. I_{lin} and I_{sat} respectively denote linear and saturation current and V_{sat} indicates the saturation voltage. For realistic devices, however, output curves are not perfectly flat at high V_{DS}.

This imperfect saturation is usually taken into account through a saturation coefficient λ, the physical origin of which can be attributed to several mechanisms. Channel length modulation is the most relevant; it correlates λ to the dependence of the channel length reduction ΔL on V_{DS} [76]. The space-charge limited conduction through the depleted semiconductor bulk can be another reason as explained in [167]. In this case, λ would mirror the dielectric property of the organic semiconductor. We infer that the electric-field dependence of mobility, which is characteristic of disordered organic materials, can also have an effect on λ in connection with the degree of disorder in the distribution of states [168].

A standard way to model the finite output conductance behavior is to multiply the total current by $(1 + \lambda V_{DS})$ [76]. The asymptotic equation by this conventional method is $I_{a1} = I_{sat}(1 + \lambda V_{DS})$. A notable drawback is that I_{a1} is not sufficiently close to real I_{DS} and this generally gives rise to inaccurate prediction of the low-voltage output conductance as pointed out in [169]. To overcome this issue, we propose $[1 + \lambda(V_{DS} - V_{sat})]$ as the multiplicative factor that leads to the shifted asymptote $I_{a2} = I_{sat}[1 + \lambda(V_{DS} - V_{sat})]$. As clearly shown in Figure 5.22(a), I_{a2} draws nearer to I_{DS} and meets I_{DS} at (V_{sat}, I_{sat}) point. This significantly raises the accuracy of the
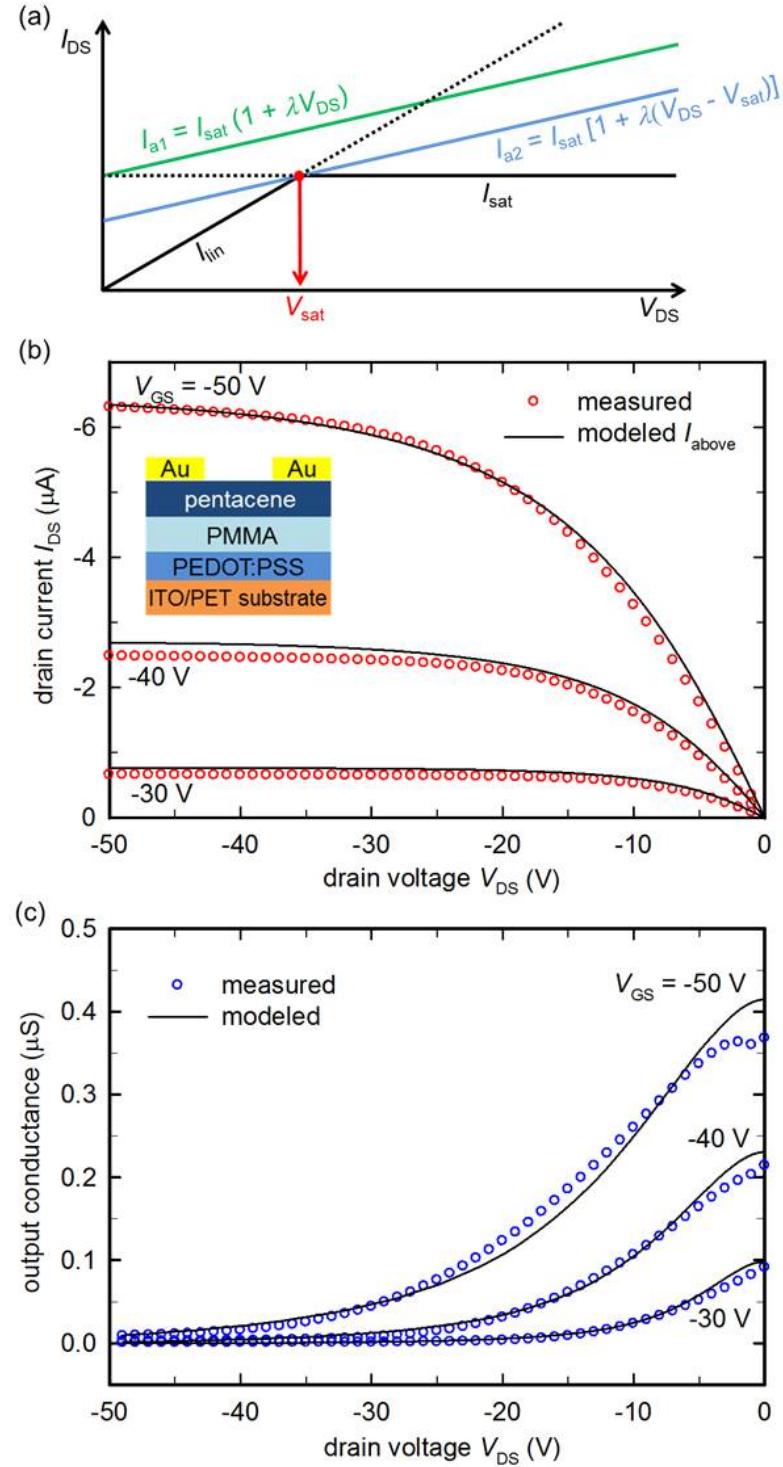
Figure 5.22: (a) Conceptual representation of the asymptotic saturation behavior. (b) Measured output curves with modeled above-threshold currents (Inset: the device structure of a pentacene OFET). (c) Output conductance from the measured data and the model calculations.

global fitting, not only for the current I_{DS} but also for the output conductance, which is an important requirement in analog circuit simulations.

We express the above-threshold drain current I_{above} as multiplication of the channel conductance g_{ch}, the effective drain voltage V_{DSe}, and the new saturation asymptotic term $[1 + \lambda(V_{DS} - V_{sat})]$. g_{ch} embraces a contact voltage drop and is written as

$$g_{ch} = \frac{-K\mu_{FET}(V_{GS} - V_T)}{[1 - R_c K\mu_{FET}(V_{GS} - V_T)]}, \tag{5.40}$$

with the dependence of field-effect mobility μ_{FET} on gate voltage V_{GS} as

$$\mu_{FET} = \frac{\mu_0}{V_{aa}^{\gamma}}|V_{GS} - V_T|^{\gamma}, \tag{5.41}$$

where K is $\frac{W}{L}C_i$, W the channel width, L the channel length, C_i the insulator capacitance per unit area, V_T the threshold voltage, R_c the contact resistance, γ the characteristic mobility exponent, V_{aa} the mobility enhancement voltage, and μ_0 the conversion mobility set to 1 cm^2/V·s. Equations (5.40) and (5.41) are written for a p-type operation, where $V_{GS} - V_T < 0$ in the above-threshold regime. V_{DSe} enables a smooth linear-to-saturation transition by the transition parameter m, and is defined as

$$V_{DSe} = V_{DS} \times \left[1 + \left(\frac{V_{DS}}{V_{sat}}\right)^m\right]^{-\frac{1}{m}}, \tag{5.42}$$

which simply approximates to V_{DS} when $|V_{DS}| \ll |V_{sat}|$ and to V_{sat} when $|V_{DS}| \gg |V_{sat}|$. Now we introduce the saturation modulation parameter α_s for using $V_{sat} = \alpha_s(V_{GS} - V_T)$ and position the absolute-valued terms to write the complete above-threshold equation as

$$I_{above} = \frac{-K\mu_{FET}(V_{GS} - V_T)V_{DS}[1 + \lambda(|V_{DS}| - \alpha_s|V_{GS} - V_T|)]}{[1 - R_c K\mu_{FET}(V_{GS} - V_T)]\left[1 + \left|\frac{V_{DS}}{\alpha_s(V_{GS} - V_T)}\right|^m\right]^{\frac{1}{m}}}. \tag{5.43}$$

Here we take the absolute values of V_{DS} and V_{sat} terms in two brackets in order to extend the range of application to both signs of V_{DS}. This allows properly equal contributions of the transition term (grouped by m) and the asymptotic term (grouped by λ) to both positive and negative V_{DS}.

The mobility model in Equation (5.41) has the same voltage dependence as the physical mobility model for OFETs based on the hopping charge transport between localized states in an exponential density of states (DOS) [170, 171]. Identifying parameters between this physical mobility model and the mobility expression given

Table 5.3: Extracted parameters from the modeled pentacene field-effect transistor

Parameter	Symbol	Value
Characteristic mobility exponent	γ	0.91
Threshold voltage	V_T	-12 V
High-voltage mobility (at $V_{\mathrm{GS}} = -50$ V)	μ_{FETHV}	0.13 cm²/V·s
Characteristic DOS temperature	T_0	440 K
Density of localized states	g_{d0}	5.7×10^{21} cm⁻³/eV
Saturation modulation parameter	α_s	0.46
Contact resistance	R_c	24 kΩ
Linear-to-saturation transition parameter	m	1.8
Saturation coefficient	λ	-1.2×10^{-3} V⁻¹
Onset voltage	V_0	-4.3 V
Off current	I_0	-66 pA
Subthreshold swing	S	4.1 V/dec
Deep trap density	N_t	1.4×10^{13} cm⁻²/eV
Transition voltage	V_B	-15 V
Below-to-above threshold transition parameter	B	0.36 V⁻¹

in Equation (5.41), we can extract the characteristic DOS temperature T_0 and the density of localized states g_{d0}.

The above-threshold parameters of a fabricated pentacene transistor were extracted according to the conventional UMEM procedure detailed in [170–172] with $W = 1000$ μm, $L = 40$ μm, and $C_i = 3.3$ nF/cm². For λ, taking into account the modification made in this study, we calculated by rearranging Equation (5.43) with respect to λ. As shown in Figure 5.22(b), the model well fits the measured output curves with the parameters listed in Table 5.3. The output differential conductance from the modeled current was also in good agreement with the experimental data as shown in Figure 5.22(c) with correct monotonous decrease at low $|V_{\mathrm{DS}}|$.

Next, subthreshold current I_{sub} of OFETs is considered to have a similar mechanism to that in MOSFETs, which describes I_{sub} as the diffusion current arising from the carrier concentration gradient between source and drain [22]. The carrier concentration exponentially varies with the surface potential and this predicts the exponential dependence of I_{sub} on V_{GS}.

Here, we propose a simplified exponential model for I_{sub} with the advantage of explicit appearance of the subthreshold swing S;

$$I_{\mathrm{sub}} = I_0 \exp\left[-\frac{\ln 10}{S}(V_{\mathrm{GS}} - V_0)\right], \tag{5.44}$$

where, I_0 is the off-current and V_0 is the onset voltage. Equation (5.44) is devised to provide an easy parameter estimation as illustrated in Figure 5.23(a). V_0 and I_0 can
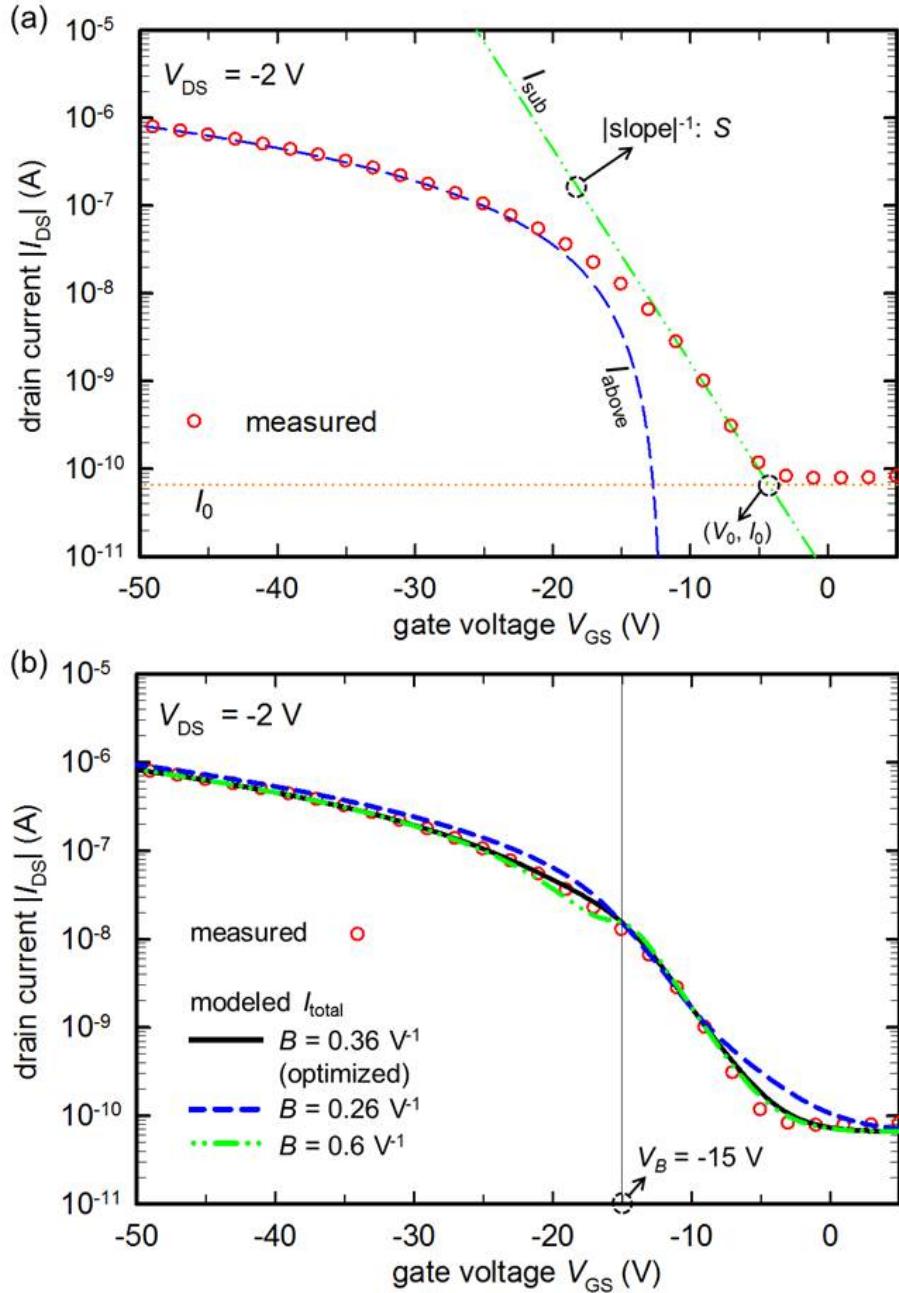
Figure 5.23: (a) A measured linear-regime transfer curve on a semi-logarithmic plot with graphical instructions on the subthreshold parameters. (b) The effect of the transition parameter B on the final model including below-to-above threshold transition.

be read in a transfer curve drawn on a semi-logarithmic plot and the inverse slope of a regression line on the exponential part directly gives S.

The existence of deep traps can significantly lower the exponential slope because they act as an additional capacitance that needs to be filled when the Fermi level moves toward the transport band edge. On that account, a physical correlation can be incorporated into Equation (5.44) referring to the method in [160, 173], by writing

$$S = \frac{k_B T \ln 10}{q} \left(\frac{q^2 N_t}{C_i} + 1 \right), \quad (5.45)$$

where N_t is the deep trap density comprising interface and bulk traps. The extracted subthreshold parameters are listed in Table 5.3.

Because of its diffusion nature, subthreshold current is practically independent of V_{DS} as long as V_{DS} is higher than a few $k_B T/q$ [22]. Equation (5.44) is based on this assumption and applicable to most unintentionally-doped organic semiconductors that are characterized by low thermal carrier density of the order of $\sim 10^{14}$ cm^{-3} (Section 4.1). Another situation might occur in polymeric OFETs, where the unintentional doping concentration can be much higher [174]. In this case, the subthreshold current can be influenced by the drift contribution of bulk dopant-induced carriers, which accompanies the V_{DS}-dependence as exemplified by the data in [175]. For modeling this type of experimental results, it is possible to further extend Equation (5.44) to include doping concentration and/or empirical V_{DS}-dependence.

Finally, a single compact expression for all regimes of OFETs is proposed. As depicted in Figure 5.23(a), modeled I_{above} and I_{sub} can only describe its corresponding regime. A traditional method used for silicon TFTs is to take $[(1/I_{\mathrm{above}}) + (1/I_{\mathrm{sub}})]^{-1}$ as the combined equation [50]. It is found that this convention lacks the general applicability to OFETs, especially when the below-to-above transition zone is spread over a wide voltage range. An alternative approach introduced in [167] makes use of a transition function for effective gate voltage, which is not compatible with our model with an independent model for I_{sub} being defined. Therefore, we propose a hyperbolic tangent transition function as the suitable method for OFETs with a tunability of the position and the degree of transition. Another advantage is the mathematical continuity at the transition point of both the hyperbolic tangent function and its first derivative.

We define the total drain current I_{total} model as

$$I_{\mathrm{total}} = I_{\mathrm{above}} \times \frac{1}{2} \Big[1 - \tanh[B(V_{\mathrm{GS}} - V_B)] \Big]$$
$$+ I_{\mathrm{sub}} \times \frac{1}{2} \Big[1 + \tanh[B(V_{\mathrm{GS}} - V_B)] \Big] + I_0, \quad (5.46)$$
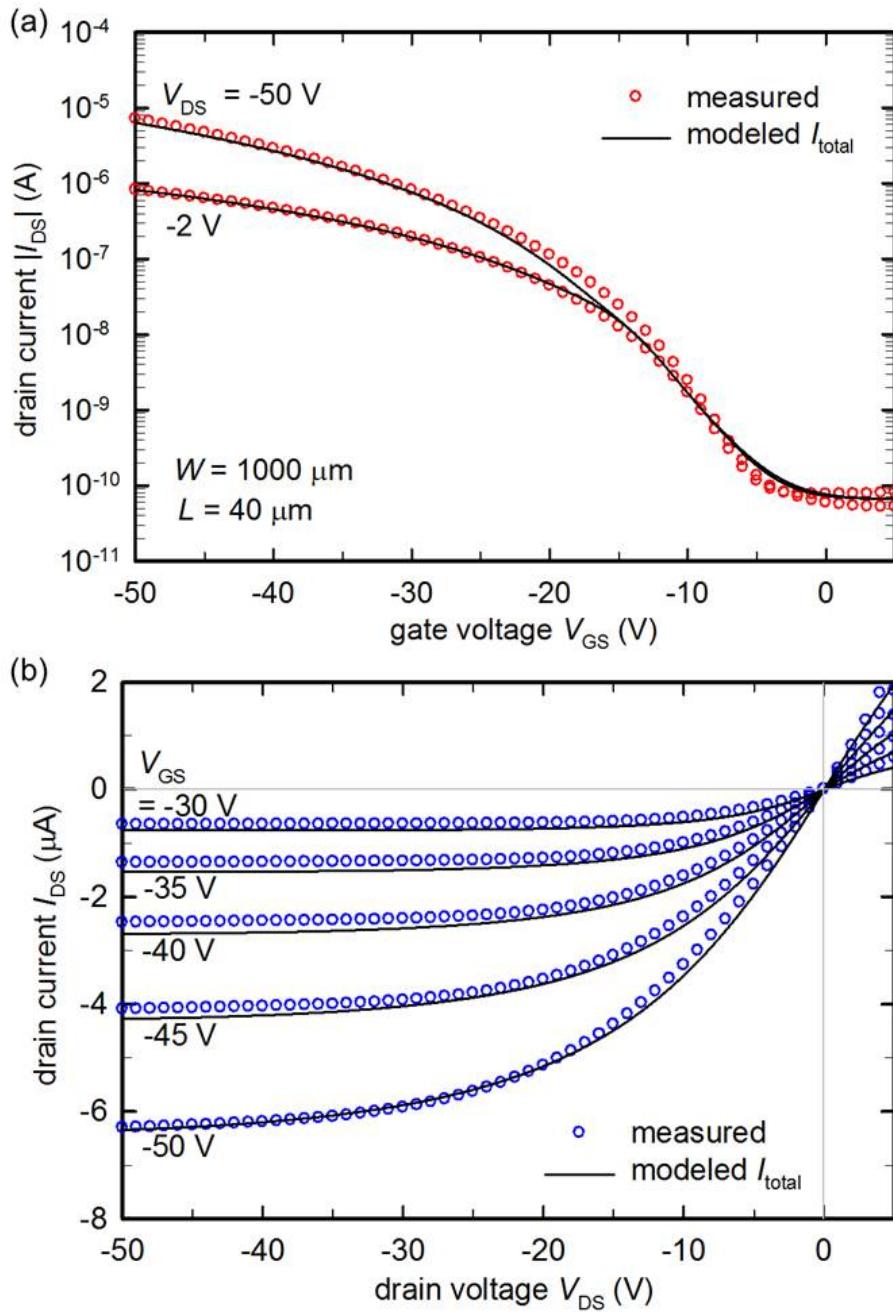
Figure 5.24: Final comparison of the model and the experimental data on (a) transfer characteristics and (b) output characteristics.

in which two additional parameters, namely the transition voltage V_B and the transition parameter B, are introduced. V_B fixes the center of transition in two hyperbolic tangent functions. A practical way is to select the voltage at which the vertical distance between I_{above} and I_{sub} is minimum [see Figure 5.23(a)]. This generally requires a V_B shifted from V_T by a few volts toward the above-threshold direction. It is because, approaching V_T, I_{above} drops down too quickly and as a consequence, choosing V_T as V_B cannot give a sufficiently smooth transition. The last parameter B dictates the degree of abruptness of the transition around V_B. B is best determined by iterative calculation and comparison to the experimental data as shown in Figure 5.23(b).

Figure 5.24 shows the final comparison of the new compact model with the experimental data over a wide bias range. The proposed model precisely reproduces measured current-voltage characteristics over off, subthreshold, linear, and saturation regimes with a single set of the extracted parameters collected in Table 5.3. The output curves in Figure 5.23(b) also show that the model correctly predicts the continuous change of current at $V_{\text{DS}} = 0$ V.

Chapter 6

Conclusion and outlook

In this thesis, results on physics-based compact modeling of organic electronic devices have been presented. Three diode structures and two transistor geometries have been investigated with multiple approaches. Here, the major findings and related conclusions are summarized and some ideas on further works are suggested.

Single-layer organic rectifying diodes in vertical configuration were fabricated with the Au/pentacene/Al stack. By combined current and impedance measurement, we found that thick pentacene layers up to ~ 1 μm were fully depleted due to an unintentional acceptor doping concentration lower than $\sim 10^{14}$ cm^{-3}. Impedance spectroscopy on a forward-biased diode showed a parallel RC circuit, which featured decreasing R and constant C with increasing V_a. Dielectric properties of pentacene were analyzed by reverse-bias measurement. An average quasistatic dielectric constant of 3.6 and a dielectric strength of 1.0 MV/cm were found. Based on the MIM energy diagram, an analytical model for the low-voltage regime was developed. The proposed I-V model predicts a significance of the blocking contact and a slight dependence of the reverse current on V_a. We found that an emergence of ideality factor can be attributed to exponential trap DOS that change voltage-dependence of the effective injection barrier.

Impedance modeling of an illuminated vertical symmetrical diode has been carried out. The device had the Au/P3HT/Au structure. Current-voltage curves at low voltage showed ohmic behavior with higher conductivity at ambient air compared to that in vacuum, which is explained by oxygen doping. The suitable equivalent circuit included a constant-phase element that might account for the rough mechanical contact interface. Persistent photoexication effect was observed from recovery data. The time-varying photoconductivity of P3HT was well fitted to an exponential function that has a decay lifetime of 110 minutes.

Organic gap-type diodes were fabricated with pentacene and TIPS-pentacene thin films and Au coplanar contacts. Transition from ohmic to SCLC current was observed for both semiconductors. Parameter extraction method based on Geurst's analytical model for 2-D SCLC was employed for simultaneously obtaining mobility and doping concentration. The extracted 2-D bulk mobility was 2.3 cm^2/V·s for pentacene and 0.023 cm^2/V·s for TIPS-pentacene. A compact model for including gap-type diodes in circuit simulation was proposed by using a conventional power-mean method for linking two physical regimes.

Pentacene OMESFETs were fabricated by using an Al gate and Au source/drain electrodes. Numerical simulation models were presented for elaborating measured current-voltage characteristics, which visualized gate-controlled distribution of injected charges. By combining measured data and simulation results, it was found that a large geometrical overlap between the gate and source/drain electrodes seriously limits the effective source-drain conduction. Electrical characteristics of several OMESFETs with different channel dimensions (W and L) were compared. A dramatic decrease in drain current with increasing W was noticed and this observation was attributed to the enhanced gate leakage with increasing overlap area that in turn frustrates lateral current flow.

OFET modeling started by comparing coplanar and staggered contact geometries in 2-D numerical simulation. We found a discontinuous channel carrier distribution in the coplanar structure, which accounted for contact-limited I-V characteristics and contact voltage drop in the calculated potential profiles. An analytical model for charge carrier distribution in coplanar OFETs was proposed by approximating Skinner's development of the electrostatic distribution for a metal/insulator junction. By integrating local conductivity in a low-carrier-density zone at the source/channel edge, we proposed a semianalytical R_c model. This model explained the V_G-dependence of R_c and also revealed a direct impact of μ on R_c. An experimentally extracted R_c-V_G curve from pentacene OFETs was well fitted by this model only when the empirical V_G-dependence of μ was taken into account. The optimized model curve gave E_b of 0.38 eV for the Au/pentacene interface. Finally, a compact modeling approach for all regimes of OFETs was proposed. The new model featured improved output asymptotic behaviors and below-to-above threshold transition by hyperbolic tangent functions. A full list of model parameters for a pentacene OFETs was provided, and the corresponding model curves show good agreement with the experimental data.

Lastly, we would like to suggest a few points for continuing modeling works on the two most application-oriented devices; rectifying diodes and OFETs. A common

interest for both devices might be in tackling the GDM so that it could be incorporated into an analytical current-voltage model. This approach will allow to extend the applicability of a model to more disordered systems. As pointed out in the work by Coehoorn and co-workers [176], there is no exact analytical solution for mobility, but there exists possibility of arriving at an approximate compact expression. Especially for OFETs where high carrier density regime might be achieved, the carrier-density-dependence of the mobility in a Gaussian DOS should be taken into account as well [127]. This task will be possibly done by converting the carrier-density dependence into the gate-voltage dependence.

For rectifying diodes, we infer that an analytical correlation between ideality factor and physical parameters might be achieved by appropriate approximation and/or empirical methods. Note that we could only numerically model the experimental data of a pentacene diode where a significant ideality factor n of 2.1 was observed (Section 4.1.5). More specifically, there is a need to correlate the barrier reduction ΔV to the trap parameters and injection barriers. If it can be successfully done, probably by means of numerical simulation, we will be able to express n as a function of N_t, T_c in addition to the other existing parameters in Equation (4.20). An interesting direction is toward OPV modeling. Bilayer or bulk-heterojunction OPVs are basically thin-film rectifying diodes. Our observation of full depletion and MIM model are believed to be applied to OPVs, and the corresponding I-V description seems to be also relevant. We can start by considering both electron and hole conduction for dark characteristics and then additionally take into account optical process for photocurrent.

For OFETs, an interesting step forward is to make an additional approximation for a fully analytical R_c model. Note that the presented model Equation (5.35) is semi-analytical because a numerical integration is involved for final calculation. For this purpose, we might be able to confine the R_c zone to the thin effective accumulation layer and get an average conductivity in that zone to calculate R_c by multiplication rather than integration. This approach will inevitably lose some degree of physical correctness, thus it should be compared to the numerical results for justifying the approximation. Another point that we are interested in is threshold voltage modeling. It should be noted the concept of 'strong inversion' in MOSFETs cannot be applied to OFETs that work in accumulation regime. We infer that V_T in OFETs might be dependent on the contact geometry as R_c does and the injection barrier plays a crucial role. The physical explanation on V_T is of great importance because it determines the so-called gate overdrive voltage $|V_G - V_T|$ on which other parameters such as μ and R_c are dependent.

Appendix A

Publications

Journal articles

(1) Chang Hyun Kim, Yvan Bonnassieux, and Gilles Horowitz, *Compact DC modeling of organic field-effect transistors: Review and perspectives*, IEEE Transactions on Electron Devices, **submitted**.

(2) Chang Hyun Kim, Htay Hlaing, Fabio Carta, Yvan Bonnassieux, Gilles Horowitz, and Ioannis Kymissis, *Templating and charge injection from copper electrodes into solution-processed organic field-effect transistors*, ACS Applied Materials & Interfaces, **5**, 3716 (2013).

(3) Chang Hyun Kim, Alejandra Castro-Carranza, Magali Estrada, Antonio Cerdeira, Yvan Bonnassieux, Gilles Horowitz, and Benjamin Iñiguez, *A compact model for organic field-effect transistors with improved output asymptotic behaviors*, IEEE Transactions on Electron Devices, **60**, 1136 (2013).

(4) Chang Hyun Kim, Yvan Bonnassieux, and Gilles Horowitz, *Charge distribution and contact resistance model for coplanar organic field-effect transistors*, IEEE Transactions on Electron Devices, **60**, 280 (2013).

(5) Chang Hyun Kim, Krzysztof Kisiel, Jaroslaw Jung, Jacek Ulanski, Denis Tondelier, Bernard Geffroy, Yvan Bonnassieux, and Gilles Horowitz, *Persistent photoexcitation effect on the poly(3-hexylthiophene) film: Impedance measurement and modeling*, Synthetic Metals, **162**, 460 (2012).

(6) Chang Hyun Kim, Denis Tondelier, Bernard Geffroy, Yvan Bonnassieux, and

Gilles Horowitz, *Characterization of the pentacene thin-film transistors with an epoxy resin-based polymeric gate insulator*, European Physical Journal-Applied Physics, **57**, 20201 (2012).

(7) Chang Hyun Kim, Denis Tondelier, Bernard Geffroy, Yvan Bonnassieux, and Gilles Horowitz, *Operating mechanism of the organic metal-semiconductor field-effect transistor (OMESFET)*, European Physical Journal-Applied Physics, **56**, 34105 (2011).

(8) Chang Hyun Kim, Omid Yaghmazadeh, Yvan Bonnassieux, and Gilles Horowitz, *Modeling the low-voltage regime of organic diodes: Origin of the ideality factor*, Journal of Applied Physics, **110**, 093722 (2011).

(9) Chang Hyun Kim, Yvan Bonnassieux, and Gilles Horowitz, *Fundamental benefits of the staggered geometry for organic field-effect transistors*, IEEE Electron Device Letters, **32**, 1302 (2011).

(10) Chang Hyun Kim, Omid Yaghmazadeh, Denis Tondelier, Yong Bin Jeong, Yvan Bonnassieux, and Gilles Horowitz, *Capacitive behavior of pentacene-based diodes: Quasistatic dielectric constant and dielectric strength*, Journal of Applied Physics, **109**, 083710 (2011).

Conference presentations

*presenting author underlined

(1) Chang Hyun Kim, Alejandra Castro-Carranza, Magali Estrada, Antonio Cerdeira, Yvan Bonnassieux, Gilles Horowitz, and Benjamin Iñiguez, *A compact model for organic field-effect transistors with improved output asymptotic behaviors*, International Symposium on Flexible Organic Electronics (ISFOE), Thessaloniki, Greece, July 8-11 (2013). **Oral**

(2) Sungyeop Jung, Chang Hyun Kim, Yvan Bonnassieux, and Gilles Horowitz, *Extraction and modeling of threshold voltage in organic field-effect transistors*, International Workshop on Compact Thin-Film Transistor Modeling for Circuit Simulation (CTFT), Grenoble, France, June 21 (2013). **Oral**

(3) <u>Chang Hyun Kim</u>, Sungyeop Jung, Yvan Bonnassieux, and Gilles Horowitz, *Analytical modeling for the contact resistance in organic field-effect transistors*, International Conference on Organic Electronics (ICOE), Grenoble, France, June 17-20 (2013). **Oral**

(4) <u>Chang Hyun Kim</u>, Htay Hlaing, Fabio Carta, Yvan Bonnassieux, Gilles Horowitz, and Ioannis Kymissis, *Solution-processed organic transistors with chemically modified copper electrodes*, International Symposium on Functional Pi-Electron Systems (F-Pi), Arcachon, France, June 2-7 (2013). **Oral**

(5) <u>Chang Hyun Kim</u>, Denis Tondelier, Bernard Geffroy, Gaël Zucchi, Abderrahim Yassar, Yvan Bonnassieux, and Gilles Horowitz, *Anisotropic charge carrier transport in TIPS-pentacene thin films*, Materials Research Society (MRS) Fall Meeting, Boston, USA, November 25-30 (2012). **Poster**

(6) <u>Chang Hyun Kim</u>, Yvan Bonnassieux, and Gilles Horowitz, *Comparison between surface and bulk charge transport in an organic semiconductor film*, International Conference on Organic Electronics (ICOE), Tarragona, Spain, June 25-27 (2012). **Oral**

(7) <u>Nikola Peřinka</u>, Chang Hyun Kim, and Yvan Bonnassieux, *Preparation and characterization of thin conductive polymer films on the base of PEDOT:PSS by inkjet printing*, International Conference Solid State Chemistry, Pardubice, Czech Republic, June 10-14 (2012). **Oral**

(8) <u>Chang Hyun Kim</u>, Denis Tondelier, Bernard Geffroy, Yvan Bonnassieux, and Gilles Horowitz, *Modeling the charge distribution and the contact resistance in coplanar organic field-effect transistors*, European Materials Research Society (E-MRS) Spring meeting, Strasbourg, France, May 14-18 (2012). **Oral**

(9) <u>Chang Hyun Kim</u>, Yvan Bonnassieux, and Gilles Horowitz, *Charge-based contact resistance modelling for coplanar organic field-effect transistors*, International Thin-film transistor Conference (ITC), Lisbon, Portugal, January 30-31 (2012). **Oral**

(10) <u>Chang Hyun Kim</u>, Denis Tondelier, Bernard Geffroy, Yvan Bonnassieux, and

Gilles Horowitz, *Modélisation physique du régime basse-tension de la diode organique : Origine du facteur d'idéalité*, Matériaux et Nanostructures Pi-Conjugués (MNPC), Obernai, France, October 03-07 (2011). **Oral**

(11) Tae-Ha Hwang, Chang Hyun Kim, Denis Tondelier, Bernard Geffroy, Yvan Bonnassieux, and Gilles Horowitz, *Analysis of organic diodes for organic photovoltaic device modeling*, Matériaux et Nanostructures Pi-Conjugués (MNPC), Obernai, France, October 03-07 (2011). **Poster**

(12) Chang Hyun Kim, Yvan Bonnassieux, and Gilles Horowitz, *Effect of the device geometry on the contact characteristics of organic field-effect transistors*, EuroDisplay, Arcachon, France, September 19-22 (2011). **Oral**

(13) Chang Hyun Kim, Denis Tondelier, Yvan Bonnassieux, and Gilles Horowitz, *Modelling the current in organic diodes*, International Conference on Organic Electronics (ICOE), Rome, Italy, June 22-24 (2011). **Oral**

(14) Chang Hyun Kim, Omid Yaghmazadeh, Denis Tondelier, Yong Bin Jeong, Bernard Geffroy, Yvan Bonnassieux, and Gilles Horowitz, *Operation mechanism of organic metal-semiconductor field-effect transistor (OMESFET) based on pentacene*, International Thin-film transistor Conference (ITC), Cambridge, UK, March 3-4 (2011). **Oral**

(15) Chang Hyun Kim, Omid Yaghmazadeh, Denis Tondelier, Jean-Charles Vanel, Bernard Geffroy, Gilles Horowitz, and Yvan Bonnassieux, *Pentacene organic metal-semiconductor field-effect transistor (OMESFET)*, Dispositifs Electroniques Organiques (DIELOR), Giens, France, October 11-13 (2010). **Oral**

Appendix B

Activities

Research visits

(1) Columbia University, New York, USA
September-November 2012
Hosting supervisor: Prof. Ioannis Kymissis

(2) Universitat Rovira i Virgili, Tarragona, Spain
June-July 2012
Hosting supervisor: Prof. Benjamin Iñiguez

Training

2nd International Training Course on Compact Modelling (TCCM 2012)
June 28-29, 2012, Tarragona, Spain

Teaching

Tutoring lecture at Ecole Polytechnique
PHY559 Circuits Intégrés Numériques & Analogiques
(Digital & Analog Integrated Circuits)
2012-2013

Journal peer-reviewing

European Physical Journal-Applied Physics
Since 2013

Appendix C

Experimental details

Vertical rectifying diodes & OMESFETs

Vertical rectifying diodes in Section 4.1 and OMESFETs in Section 5.1 were fabricated by the same process run. They are based on the Au/pentacene/Al structure and fabricated using the following procedure. With 10 nm of adhesion layer of Al, 50 nm of Au bottom electrode was vacuum-evaporated on a cleaned glass substrate. Pentacene (Sigma Aldrich) was subsequently evaporated with controlled final thicknesses. Several samples with the nominal pentacene thickness of 200 nm, 500 nm, and 1000 nm were prepared. The devices were finished by evaporating Al top electrode, of which the thickness was 50, 80, and 150 nm for each pentacene thickness, to make sure of the step coverage. All evaporation processes were done under a base pressure of 2×10^{-7} mbar and the substrate was kept at room temperature. The average evaporation rate of pentacene was 0.1 nm/s.

All the fabrication steps were conducted in a nitrogen-filled globe box and the measurements are done in the ambient atmosphere. Current-voltage characteristics were recorded using a Keithley 4200 semiconductor characterization system and impedance measurements were conducted using a HP 4192A LF impedance analyzer. For thickness variation study, more precise values were obtained by a Dektak 150 (Veeco) surface profiler.

Vertical symmetrical diodes

The Au/P3HT/Au devices described in Section 4.2 were fabricated on a Cr-coated steel substrate. After ultrasonication cleaning in chloroform, 150 nm of Au bottom electrode was vacuum evaporated. P3HT (American Dye Source) was dissolved in

chloroform at a concentration of 8 mg/mL and drop-cast. The film was dried at 50 °C for 24 hours in a vacuum oven. This process led to the relatively thick P3HT films of ~ 10 μm. One hundred fifty nanometers of Au top electrode was finally deposited by vacuum evaporation and it defined the circular active area of 0.78 cm^2.

UV-VIS absorption spectrum of a P3HT film was measured using a double beam UV-VIS-NIR Varian spectrometer model Carry 5000. Current-voltage measurements were carried out using a Keithley 2400 source meter. Impedance data were obtained using Novocontrol broadband dielectric spectroscopy system including high resolution dielectric analyzer ALPHA-ANB. For photoexcitation study, the sample was illuminated by a white fluorescent lamp.

Gap-type diodes

The gap-type diodes in Section 4.3 were fabricated with the top-contact configuration. For the pentacene diodes, 150 nm of pentacene (Sigma Aldrich) was vacuum evaporated on a glass substrate at the deposition rate of 0.2 nm/s without substrate heating. For the TIPS-pentacene samples, TIPS-pentacene (Sigma Aldrich) was first dissolved in 1,2-dichlorobenzene at a concentration of 30 mg/mL. The solution was then spin-coated on a glass substrate with a spin speed of 1500 rpm for 30 seconds. The film was immediately annealed on a hot plate at 100 °C for 1 hour in a nitrogen glove box. The thickness of the TIPS-pentacene film measured by a Dektak 150 (Veeco) surface profiler was 150 nm. For both pentacene and TIPS-pentacene diodes, 60 nm of Au top contact was evaporated through a shadow mask, which defined the electrode spacing of 30 μm and the width of 1000 μm. Current-voltage characteristics of the final devices were obtained using a Keithley 4200 semiconductor characterization system.

OFETs 1: SU-8 dielectric

The experimental results shown in Section 5.2.4 for coplanar OFET modeling were obtained from the characterization of the pentacene OFETs with the bottom-gate, bottom-contact configuration. The gate electrode was prepared by a deposition of Cr on a glass substrate. An epoxy-based photoresist SU-8 was used as a gate dielectric. A diluted SU-8 solution (SU-8 2050 product of MicroChem) was spin-coated and UV

exposed to activate the cross-linking reaction. The processed film was baked at 200 °C for 2 minutes. This method gave a 950-nm-thick polymeric film with a gate capacitance of 2.3 nF/cm^2. The source/drain electrodes were formed by depositing Au, followed by a photolithographical patterning steps. Pentacene (Sigma Aldrich) was vacuum evaporated to finish the device fabrication. During the thermal evaporation of pentacene, the substrate was heated at 50 °C, and the deposition rate was kept at 0.1 nm/s with a final thickness of 50 nm. Current-voltage measurements were conducted using a Keithley 4200 semiconductor characterization system.

OFETs 2: PMMA dielectric

The experimental data in Section 5.2.5 for compact modeling were from the flexible pentacene OFETs with the bottom-gate, top-contact configuration. An indium-tin-oxide (ITO) coated poly(ethylene terephthalate) (PET) film (Sigma Aldrich, 60 $\Omega/\square$ product) was used as a substrate and a common gate electrode. The substrate was ultrasonically cleaned in isopropanol and treated with UV/ozone. A thin poly(3,4-ethylenedioxythiophene):poly(styrenesulfonate) (PEDOT:PSS) (Ossila) layer was spin coated and annealed at 100 °C for 10 minutes as a buffer layer for reduced gate leakage. Poly(methylmethacrylate) (PMMA) (Sigma Aldrich) dissolved in toluene at a concentration of 80 mg/mL was spin coated and cured at 120 °C for 1 hour as a polymeric gate insulator (970 nm). One hundred nanometers of pentacene (Sigma Aldrich) was vacuum evaporated for the active layer at 0.05 nm/s under the base pressure of 2×10^{-6} mbar, without substrate heating. Finally, 60 nm of Au was evaporated to defined the source/drain electrodes. Current-voltage measurements were conducted using a Keithley 4200 semiconductor characterization system.

Bibliography

[1] W. H. Brown and T. Poon, *Introduction to Organic Chemistry*, 2nd ed. New York: Wiley, 2004.

[2] H. Shirakawa, E. J. Louis, A. G. MacDiarmid, C. K. Chiang, and A. J. Heeger, "Synthesis of electrically conducting organic polymers: halogen derivatives of polyacetylene, $(CH)_x$," *J. Chem. Soc. Chem. Commun.*, pp. 578–580, 1977.

[3] C. W. Tang, "Two-layer organic photovoltaic cell," *Appl. Phys. Lett.*, vol. 48, pp. 183–185, 1986.

[4] A. Tsumura, H. Koezuka, and T. Ando, "Macromolecular electronic device: Field-effect transistor with a polythiophene thin film," *Appl. Phys. Lett.*, vol. 49, pp. 1210–1212, 1986.

[5] C. W. Tang and S. A. VanSlyke, "Organic electroluminescent diodes," *Appl. Phys. Lett.*, vol. 51, pp. 913–915, 1987.

[6] CES 2013: Samsung shows off new flexible display technology; Bill Clinton appears as guest. [Online]. Available: http://articles.washingtonpost.com/2013/jan/09

[7] B. W. D'Andrade and S. R. Forrest, "White organic light-emitting devices for solid-state lighting," *Adv. Mater.*, vol. 16, pp. 1585–1595, 2004.

[8] S. Reineke, F. Lindner, G. Schwartz, N. Seidler, K. Walzer, B. Lussem, and K. Leo, "White organic light-emitting diodes with fluorescent tube efficiency," *Nature*, vol. 459, pp. 234–238, 2009.

[9] Y. Nakajima, Y. Fujisaki, T. Takei, H. Sato, M. Nakata, M. Suzuki, H. Fukagawa, G. Motomura, T. Shimizu, Y. Isogai, K. Sugitani, T. Katoh, S. Tokito, T. Yamamoto, and H. Fujikake, "Low-temperature fabrication of 5-in. QVGA flexible AMOLED display driven by OTFTs using olefin polymer as the gate insulator," *J. Soc. Inf. Disp.*, vol. 19, pp. 861–866, 2011.

[10] S. Steudel, K. Myny, S. Schols, P. Vicca, S. Smout, A. Tripathi, B. van der Putten, J.-L. van der Steen, M. van Neer, F. Schütze, O. R. Hild, E. van Veenendaal, P. van Lieshout, M. van Mil, J. Genoe, G. Gelinck, and P. Heremans, "Design and realization of a flexible QQVGA AMOLED display with organic TFTs," *Org. Electron.*, vol. 13, pp. 1729–1735, 2012.

[11] Plastic Logic. [Online]. Available: http://www.plasticlogic.com/applications

[12] T. Someya, T. Sekitani, S. Iba, Y. Kato, H. Kawaguchi, and T. Sakurai, "A large-area, flexible pressure sensor matrix with organic field-effect transistors for artificial skin applications," *Proc. Natl. Acad. Sci. U. S. A.*, vol. 101, pp. 9966–9970, 2004.

[13] T. Someya, Y. Kato, I. Shingo, Y. Noguchi, T. Sekitani, H. Kawaguchi, and T. Sakurai, "Integration of organic FETs with organic photodiodes for a large area, flexible, and lightweight sheet image scanners," *IEEE Trans. Electron Devices*, vol. 52, pp. 2502–2511, 2005.

[14] I. Nausieda, K. Ryu, I. Kymissis, A. I. Akinwande, V. Bulovic, and C. G. Sodini, "An organic active-matrix imager," *IEEE Trans. Electron Devices*, vol. 55, pp. 527–532, 2008.

[15] H. Yu-Jen, J. Zhang, and I. Kymissis, "A locally amplified strain sensor based on a piezoelectric polymer and organic field-effect transistors," *IEEE Trans. Electron Devices*, vol. 58, pp. 910–917, 2011.

[16] B. Kippelen and J.-L. Bredas, "Organic photovoltaics," *Energy Environ. Sci.*, vol. 2, pp. 251–261, 2009.

[17] Konarka Technologies. [Online]. Available: http://www.konarka.com

[18] R. M. Owens and G. G. Malliaras, "Organic electronics at the interface with biology," *MRS Bull.*, vol. 35, pp. 449–456, 2010.

[19] K. Svennersten, K. C. Larsson, M. Berggren, and A. Richter-Dahlfors, "Organic bioelectronics in nanomedicine," *Biochim. Biophys. Acta-Gen. Subj.*, vol. 1810, pp. 276–285, 2011.

[20] AIM-SPICE. [Online]. Available: http://www.aimspice.com

[21] S. M. Sze and K. K. Ng, *Physics of Semiconductor Devices*, 3rd ed. New York: Wiley, 2007.

[22] J.-P. Colinge and C. A. Colinge, *Physics of Semiconductor Devices*. Boston, MA: Kluwer, 2002.

[23] R. S. Muller and T. I. Kamins, *Device Electronics for Integrated Circuits*, 3rd ed. New York: Wiley, 2003.

[24] I. Kymissis, *Organic Field Effect Transistors: Theory, Fabrication and Characterization*. New York, NY: Springer, 2009.

[25] T. Sekitani and T. Someya, "Stretchable, large-area organic electronics," *Adv. Mater.*, vol. 22, pp. 2228–2246, 2010.

[26] G. H. Gelinck, H. E. A. Huitema, E. van Veenendaal, E. Cantatore, L. Schrijnemakers, J. B. P. H. van der Putten, T. C. T. Geuns, M. Beenhakkers, J. B. Giesbers, B.-H. Huisman, E. J. Meijer, E. M. Benito, F. J. Touwslager, A. W. Marsman, B. J. E. van Rens, and D. M. de Leeuw, "Flexible active-matrix displays and shift registers based on solution-processed organic transistors," *Nature Mater.*, vol. 3, pp. 106–110, 2004.

[27] D. K. Hwang, C. Fuentes-Hernandez, J. B. Kim, W. J. P. Jr, and B. Kippelen, "Flexible and stable solution-processed organic field-effect transistors," *Org. Electron.*, vol. 12, pp. 1108–1113, 2011.

[28] T. Sekitani and T. Someya, "Ambient electronics," *Jpn. J. Appl. Phys.*, vol. 51, p. 100001, 2012.

[29] C. Reese and Z. Bao, "Organic single crystals: tools for the exploration of charge transport phenomena in organic materials," *J. Mater. Chem.*, vol. 16, pp. 329–333, 2006.

[30] V. Podzorov, "Organic single crystals: Addressing the fundamentals of organic electronics," *MRS Bull.*, vol. 38, pp. 15–24, 2013.

[31] H. Sirringhaus, T. Kawase, R. H. Friend, T. Shimoda, M. Inbasekaran, W. Wu, and E. P. Woo, "High-resolution inkjet printing of all-polymer transistor circuits," *Science*, vol. 290, pp. 2123–2126, 2000.

[32] I. McCulloch, M. Heeney, C. Bailey, K. Genevicius, I. MacDonald, M. Shkunov, D. Sparrowe, S. Tierney, R. Wagner, W. Zhang, M. L. Chabinyc, R. J. Kline, M. D. McGehee, and M. F. Toney, "Liquid-crystalline semiconducting polymers with high charge-carrier mobility," *Nature Mater.*, vol. 5, pp. 328–333, 2006.

[33] A. C. Arias, J. D. MacKenzie, I. McCulloch, J. Rivnay, and A. Salleo, "Materials and applications for large area electronics: Solution-based approaches," *Chem. Rev.*, vol. 110, pp. 3–24, 2010.

[34] S. K. Park, T. N. Jackson, J. E. Anthony, and D. A. Mourey, "High mobility solution processed 6,13-bis(triisopropyl-silylethynyl) pentacene organic thin film transistors," *Appl. Phys. Lett.*, vol. 91, p. 063514, 2007.

[35] D. J. Gundlach, J. E. Royer, S. K. Park, S. Subramanian, O. D. Jurchescu, B. H. Hamadani, A. J. Moad, R. J. Kline, L. C. Teague, O. Kirillov, C. A. Richter, J. G. Kushmerick, L. J. Richter, S. R. Parkin, T. N. Jackson, and J. E. Anthony, "Contact-induced crystallinity for high-performance soluble acene-based transistors and circuits," *Nature Mater.*, vol. 7, pp. 216–221, 2008.

[36] J. E. Anthony, "The larger acenes: Versatile organic semiconductors," *Angew. Chem.-Int. Edit.*, vol. 47, pp. 452–483, 2008.

[37] C. R. Newman, C. D. Frisbie, D. A. da Silva Filho, J.-L. Brédas, P. C. Ewbank, , and K. R. Mann, "Introduction to organic thin film transistors and design of n-channel organic semiconductors," *Chem. Mater.*, vol. 16, pp. 4436–4451, 2004.

[38] L.-L. Chua, J. Zaumseil, J.-F. Chang, E. C. W. Ou, P. K. H. Ho, H. Sirringhaus, and R. H. Friend, "General observation of n-type field-effect behaviour in organic semiconductors," *Nature*, vol. 434, pp. 194–199, 2005.

[39] A. Facchetti, "Semiconductors for organic transistors," *Mater. Today*, vol. 10, pp. 28–37, 2007.

[40] J. E. Anthony, A. Facchetti, M. Heeney, S. R. Marder, and X. Zhan, "n-type organic semiconductors in organic electronics," *Adv. Mater.*, vol. 22, pp. 3876–3892, 2010.

[41] H. Yan, Z. Chen, Y. Zheng, C. Newman, J. R. Quinn, F. Dotz, M. Kastler, and A. Facchetti, "A high-mobility electron-transporting polymer for printed transistors," *Nature*, vol. 457, pp. 679–686, 2009.

[42] J. D. Livingston, *Electronic Properties of Engineering Materials*. New York: Wiley, 1999.

[43] W. Warta, R. Stehle, and N. Karl, "Ultrapure, high mobility organic photoconductors," *Appl. Phys. A*, vol. 36, pp. 163–170, 1985.

[44] O. Ostroverkhova, D. G. Cooke, S. Shcherbyna, R. F. Egerton, F. A. Hegmann, R. R. Tykwinski, and J. E. Anthony, "Bandlike transport in pentacene and functionalized pentacene thin films revealed by subpicosecond transient photoconductivity measurements," *Phys. Rev. B*, vol. 71, p. 035204, 2005.

[45] T. Sakanoue and H. Sirringhaus, "Band-like temperature dependence of mobility in a solution-processed organic semiconductor," *Nature Mater.*, vol. 9, pp. 736–740, 2010.

[46] C. Liu, T. Minari, X. Lu, A. Kumatani, K. Takimiya, and K. Tsukagoshi, "Solution-processable organic single crystals with bandlike transport in field-effect transistors," *Adv. Mater.*, vol. 23, pp. 523–526, 2011.

[47] N. A. Minder, S. Ono, Z. Chen, A. Facchetti, and A. F. Morpurgo, "Band-like electron transport in organic transistors and implication of the molecular structure for performance optimization," *Adv. Mater.*, vol. 24, pp. 503–508, 2012.

[48] G. Horowitz, "Organic field-effect transistors," *Adv. Mater.*, vol. 10, pp. 365–377, 1998.

[49] M. Shur, M. Hack, and J. G. Shaw, "A new analytic model for amorphous silicon thin-film transistors," *J. Appl. Phys.*, vol. 66, pp. 3371–3380, 1989.

[50] M. S. Shur, M. D. Jacunski, H. C. Slade, and M. Hack, "Analytical models for amorphous-silicon and polysilicon thin-film transistors for high-definition-display technology," *J. Soc. Inf. Disp.*, vol. 3, pp. 223–236, 1995.

[51] G. Horowitz, R. Hajlaoui, and P. Delannoy, "Temperature dependence of the field-effect mobility of sexithiophene. determination of the density of traps," *J. Phys. III France*, vol. 5, pp. 355–371, 1995.

[52] P. Mark and W. Helfrich, "Space-charge-limited currents in organic crystals," *J. Appl. Phys.*, vol. 33, pp. 205–215, 1962.

[53] G. Horowitz, M. E. Hajlaoui, and R. Hajlaoui, "Temperature and gate voltage dependence of hole mobility in polycrystalline oligothiophene thin film transistors," *J. Appl. Phys.*, vol. 87, pp. 4456–4463, 2000.

[54] H. Bässler, "Charge transport in disordered organic photoconductors: A Monte Carlo simulation study," *Phys. Stat. Solidi B*, vol. 175, pp. 15–56, 1993.

[55] A. Miller and E. Abrahams, "Impurity conduction at low concentrations," *Phys. Rev.*, vol. 120, pp. 745–755, 1960.

[56] D. Monroe, "Hopping in exponential band tails," *Phys. Rev. Lett.*, vol. 54, pp. 146–149, 1985.

[57] A. Kahn, N. Koch, and W. Gao, "Electronic structure and electrical properties of interfaces between metals and π-conjugated molecular films," *J. Polym. Sci. B, Polym. Phys.*, vol. 41, pp. 2529–2548, 2003.

[58] J. Hwang, A. Wan, and A. Kahn, "Energetics of metal-organic interfaces: New experiments and assessment of the field," *Mater. Sci. Eng. R*, vol. 64, pp. 1–31, 2009.

[59] H. Ishii and K. Seki, "Energy level alignment at organic/metal interfaces studied by UV photoemission: Breakdown of traditional assumption of a common vacuum level at the interface," *IEEE Trans. Electron Devices*, vol. 44, pp. 1295–1301, 1997.

[60] H. Ishii, K. Sugiyama, E. Ito, and K. Seki, "Energy level alignment and interfacial electronic structures at organic/metal and organic/organic interfaces," *Adv. Mater.*, vol. 11, pp. 605–625, 1999.

[61] L. Miozzo, A. Yassar, and G. Horowitz, "Surface engineering for high performance organic electronic devices: the chemical approach," *J. Mater. Chem.*, vol. 20, pp. 2513–2538, 2010.

[62] N. Koch and A. Vollmer, "Electrode-molecular semiconductor contacts: Work-function-dependent hole injection barriers versus Fermi-level pinning," *Appl. Phys. Lett.*, vol. 89, p. 162107, 2006.

[63] S. Braun, W. R. Salaneck, and M. Fahlman, "Energy-level alignment at organic/metal and organic/organic interfaces," *Adv. Mater.*, vol. 21, pp. 1450–1472, 2009.

[64] C. K. Alexander and M. N. O. Sadiku, *Fundamentals of Electric Circuits*, 2nd ed. New York: McGraw-Hill, 2004.

[65] J. R. Macdonald, "Impedance spectroscopy," *Ann. Biomed. Eng.*, vol. 20, pp. 289–305, 1992.

[66] J. Drechsel, M. Pfeiffer, X. Zhou, A. Nollau, and K. Leo, "Organic MIP-diodes by p-doping of amorphous wide-gap semiconductors: CV and impedance spectroscopy," *Synth. Met.*, vol. 127, pp. 201–205, 2002.

[67] M. Glatthaar, N. Mingirulli, B. Zimmermann, T. Ziegler, R. Kern, M. Niggemann, A. Hinsch, and A. Gombert, "Impedance spectroscopy on organic bulk-heterojunction solar cells," *Phys. Status Solidi A-Appl. Mater.*, vol. 202, pp. R125–R127, 2005.

[68] G. Garcia-Belmonte, A. Munar, E. M. Barea, J. Bisquert, I. Ugarte, and R. Pacios, "Charge carrier mobility and lifetime of organic bulk heterojunctions analyzed by impedance spectroscopy," *Org. Electron.*, vol. 9, pp. 847–851, 2008.

[69] T. Okachi, T. Nagase, T. Kobayashi, and H. Naito, "Determination of charge-carrier mobility in organic light-emitting diodes by impedance spectroscopy in presence of localized states," *Jpn. J. Appl. Phys.*, vol. 47, pp. 8965–8972, 2008.

[70] G. Garcia-Belmonte, P. P. Boix, J. Bisquert, M. Sessolo, and H. J. Bolink, "Simultaneous determination of carrier lifetime and electron density-of-states in P3HT:PCBM organic solar cells under illumination by impedance spectroscopy," *Sol. Energy Mater. Sol. Cells*, vol. 94, pp. 366–375, 2010.

[71] BioLogic. [Online]. Available: http://www.bio-logic.info/ potentiostat/eclab.html

[72] V. S. Reddy, S. Das, S. K. Ray, and A. Dhar, "Studies on conduction mechanisms of pentacene based diodes using impedance spectroscopy," *J. Phys. D: Appl. Phys.*, vol. 40, pp. 7687–7693, 2007.

[73] C.-C. Chen, B.-C. Huang, M.-S. Lin, Y.-J. Lu, T.-Y. Cho, C.-H. Chang, K.-C. Tien, S.-H. Liu, T.-H. Ke, and C.-C. Wu, "Impedance spectroscopy and equivalent circuits of conductively doped organic hole-transport materials," *Org. Electron.*, vol. 11, pp. 1901–1908, 2010.

[74] R. Woltjer, L. Tiemeijer, and D. Klaassen, "An industrial view on compact modeling," in *Proc. European Solid-State Device Research Conference (ESSDRC'06)*, Montreux, Switzerland, 2006, pp. 41–48.

[75] K. Lee, M. Shur, T. A. Fjeldly, and T. Ytterdal, *Semiconductor Device Modeling for VLSI.* New Jersey: Prentice Hall, 1993.

[76] T. A. Fjeldly, T. Ytterdal, and M. Shur, *Introduction to Device Modeling and Circuit Simulation*, 1st ed. New York: Wiley, 1998.

[77] Silvaco ATLAS. [Online]. Available: http://www.silvaco.com/products/device_simulation/atlas.html

[78] C.-H. Shim, F. Maruoka, and R. Hattori, "Structural analysis on organic thin-film transistor with device simulation," *IEEE Trans. Electron Devices*, vol. 57, pp. 195–200, 2010.

[79] L. Feng, X. Xu, and X. Guo, "Structure-dependent contact barrier effects in bottom-contact organic thin-film transistors," *IEEE Trans. Electron Devices*, vol. 59, pp. 3382–3388, 2012.

[80] S. Steudel, K. Myny, V. Arkhipov, C. Deibel, S. D. Vusser, J. Genoe, and P. Heremans, "50 MHz rectifier based on an organic diode," *Nat. Mater.*, vol. 4, pp. 597–600, 2005.

[81] S. Steudel, S. D. Vusser, K. Myny, M. Lenes, J. Genoe, and P. Heremans, "Comparison of organic diode structures regarding high-frequency rectification behavior in radio-frequency identification tags," *J. Appl. Phys.*, vol. 99, p. 114519, 2006.

[82] A. Haldi, A. Sharma, J. W. J. Potscavage, and B. Kippelen, "Equivalent circuit model for organic single-layer diodes," *J. Appl. Phys.*, vol. 104, p. 064503, 2008.

[83] D. M. Taylor and H. L. Gomes, "Electrical characterization of the rectifying contact between aluminium and electrodeposited poly(3-methylthiophene)," *J. Phys. D: Appl. Phys.*, vol. 28, pp. 2554–2568, 1995.

[84] P. Stallinga, H. L. Gomes, M. Murgia, and K. Müllen, "Interface state mapping in a Schottky barrier of the organic semiconductor terrylene," *Org. Electron.*, vol. 3, pp. 43–51, 2002.

[85] A. Takshi, A. Dimopoulos, and J. D. Madden, "Depletion width measurement in an organic Schottky contact using a metal-semiconductor field-effect transistor," *Appl. Phys. Lett.*, vol. 91, p. 083513, 2007.

[86] T. Kirchartz, W. Gong, S. A. Hawks, T. Agostinelli, R. C. I. MacKenzie, Y. Yang, and J. Nelson, "Sensitivity of the Mott-Schottky analysis in organic solar cells," *J. Phys. Chem. C*, vol. 116, pp. 7672–7680, 2012.

[87] D. Braga, M. Campione, A. Borghesi, and G. Horowitz, "Organic metal-semiconductor field-effect transistor (OMESFET) fabricated on a rubrene single crystal," *Adv. Mater.*, vol. 22, pp. 424–428, 2010.

[88] M. Pfeiffer, K. Leo, X. Zhou, J. S. Huang, M. Hofmann, A. Werner, and J. Blochwitz-Nimoth, "Doped organic semiconductors: Physics and application in light emitting diodes," *Org. Electron.*, vol. 4, pp. 89–103, 2003.

[89] W. Gao and A. Kahn, "Electrical doping: the impact on interfaces of π-conjugated molecular films," *J. Phys. Condens. Matter*, vol. 15, pp. S2757–S2770, 2003.

[90] O. D. Jurchescu, J. Baas, and T. T. M. Palstra, "Electronic transport properties of pentacene single crystals upon exposure to air," *Appl. Phys. Lett.*, vol. 87, p. 052102, 2005.

[91] A. Takshi, A. Dimopoulos, and J. D. Madden, "Simulation of a low-voltage organic transistor compatible with printing methods," *IEEE Trans. Electron Devices*, vol. 55, pp. 276–282, 2008.

[92] G. Liang, T. Cui, and K. Varahramyan, "Fabrication and electrical characteristics of polymer-based Schottky diode," *Solid-State Electron.*, vol. 47, pp. 691–694, 2003.

[93] O. G. Reid, K. Munechika, and D. S. Ginger, "Space charge limited current measurements on conjugated polymer films using conductive atomic force microscopy," *Nano Lett.*, vol. 8, pp. 1602–1609, 2008.

[94] A. Facchetti, M. H. Yoon, and T. J. Marks, "Gate dielectrics for organic field-effect transistors: New opportunities for organic electronics," *Adv. Mater.*, vol. 17, pp. 1705–1725, 2005.

[95] J. Melai, C. Salm, S. Smits, J. Visschers, and J. Schmitz, "The electrical conduction and dielectric strength of SU-8," *J. Micromech. Microeng.*, vol. 19, p. 065012, 2009.

[96] R. Ruiz, D. Choudhary, B. Nickel, T. Toccoli, K.-C. Chang, A. C. Mayer, P. Clancy, J. M. Blakely, R. L. Headrick, S. Iannotta, and G. G. Malliaras, "Pentacene thin film growth," *Chem. Mater.*, vol. 16, pp. 4497–4508, 2004.

[97] W. Brütting, S. Berleb, and A. G. Mückl, "Device physics of organic light-emitting diodes based on molecular materials," *Org. Electron.*, vol. 2, pp. 1–36, 2001.

[98] N. F. Mott and R. W. Gurney, *Electronic Processes in Ionic Crystals*, 1st ed. London: Oxford Univ. Press, 1940.

[99] K. C. Kao and W. Hwang, *Electrical Transport in Solids: With Particular Reference to Organic Semiconductors*, 1st ed. London: Pergamon, 1981.

[100] S. M. Skinner, "Diffusion, static charges, and the conduction of electricity in nonmetallic solids by a single charge carrier. I. Electric charges in plastics and insulating materials," *J. Appl. Phys.*, vol. 26, pp. 498–508, 1955.

[101] ——, "Diffusion, static charges, and the conduction of electricity in nonmetallic solids by a single charge carrier. II. Solution of the rectifier equations for insulating layers," *J. Appl. Phys.*, vol. 26, pp. 509–518, 1955.

[102] G. T. Wright, "Mechanisms of space-charge-limited current in solids," *Solid-State Electron.*, vol. 2, pp. 165–189, 1961.

[103] G. Dennler, M. C. Scharber, and C. J. Brabec, "Polymer-fullerene bulk-heterojunction solar cells," *Adv. Mater.*, vol. 21, pp. 1323–1338, 2009.

[104] V. Kumar, S. C. Jain, A. K. Kapoor, J. Poortmans, and R. Mertens, "Trap density in conducting organic semiconductors determined from temperature dependence of J - V characteristics," *J. Appl. Phys.*, vol. 94, pp. 1283–1285, 2003.

[105] W. L. Kalb, K. Mattenberger, and B. Batlogg, "Oxygen-related traps in pentacene thin films: Energetic position and implications for transistor performance," *Phys. Rev. B*, vol. 78, p. 035334, 2008.

[106] W. L. Kalb, S. Haas, C. Krellner, T. Mathis, and B. Batlogg, "Trap density of states in small-molecule organic semiconductors: A quantitative comparison of thin-film transistors with single crystals," *Phys. Rev. B*, vol. 81, p. 155315, 2010.

[107] J. H. Cho, D. H. Kim, Y. Jang, W. H. Lee, K. Ihm, J.-H. Han, S. Chung, and K. Cho, "Effects of metal penetration into organic semiconductors on the electrical properties of organic thin film transistors," *Appl. Phys. Lett.*, vol. 89, p. 132101, 2006.

[108] A. Wan, J. Hwang, F. Amy, and A. Kahn, "Impact of electrode contamination on the α-NPD/Au hole injection barrier," *Org. Electron.*, vol. 6, pp. 47–54, 2005.

[109] V. D. Mihailetchi, H. X. Xie, B. de Boer, L. J. A. Koster, and P. W. M. Blom, "Charge transport and photocurrent generation in poly(3-hexylthiophene):methanofullerene bulk-heterojunction solar cells," *Adv. Funct. Mater.*, vol. 16, pp. 699–708, 2006.

[110] J. Y. Kim, K. Lee, N. E. Coates, D. Moses, T.-Q. Nguyen, M. Dante, and A. J. Heeger, "Efficient tandem polymer solar cells fabricated by all-solution processing," *Science*, vol. 317, pp. 222–225, 2007.

[111] M. R. Antognazza, D. Musitelli, S. Perissinotto, and G. Lanzani, "Spectrally selected photodiodes for colorimetric application," *Org. Electron.*, vol. 11, pp. 357–362, 2010.

[112] S. Ogawa, T. Naijo, Y. Kimura, H. Ishii, and M. Niwano, "Photoinduced doping effect of pentacene field effect transistor in oxygen atmosphere studied by displacement current measurement," *Appl. Phys. Lett.*, vol. 86, p. 252104, 2005.

[113] J. R. Macdonald, "Note on the parameterization of the constant-phase admittance element," *Solid State Ionics*, vol. 13, pp. 147–149, 1984.

[114] J. Drechsel, B. Männig, D. Gebeyehu, M. Pfeiffer, K. Leo, and H. Hoppe, "MIP-type organic solar cells incorporating phthalocyanine/fullerene mixed layers and doped wide-gap transport layers," *Org. Electron.*, vol. 5, pp. 175–186, 2004.

[115] O. Fernández, D. M. Taylor, J. A. Drysdale, and D. M. Ellis, "Photogenerated minority carrier trapping and inversion layer formation in polymer field-effect structures," *IEEE Trns. Dielectr. Electr. Insul.*, vol. 13, pp. 1093–1100, 2006.

[116] D. M. Taylor, J. A. Drysdale, I. Torres, and O. Fernández, "Electron trapping and inversion layer formation in photoexcited metal-insulator-poly(3-hexylthiophene) capacitors," *Appl. Phys. Lett.*, vol. 89, p. 183512, 2006.

[117] C. H. Kim, M. H. Choi, S. H. Lee, J. Jang, and S. Kirchmeyer, "Dependence of persistent photocurrent on gate bias in inkjet printed organic thin-film transistor," *Appl. Phys. Lett.*, vol. 96, p. 123301, 2010.

[118] P. Lutsyk, K. Janus, M. Mikolajczyk, J. Sworakowski, B. Boratynski, and M. Tlaczala, "Long-lived persistent currents in poly(3-octylthiophene) thin film transistors," *Org. Electron.*, vol. 11, pp. 490–497, 2010.

[119] M. Polke, J. Stuke, and E. Vinaricky, "Raumladungsbegrenzte ströme in hexagonalen Se-kristallen," *Phys. Stat. Sol.*, vol. 3, pp. 1885–1891, 1963.

[120] J. A. Geurst, "Theory of space-charge-limited currents in thin semiconductor layers," *Phys. Stat. Sol.*, vol. 15, pp. 107–118, 1966.

[121] R. Zuleeg and P. Knoll, "Space-charge-limited currents in heteroepitaxial films of silicon grown on sapphire," *Appl. Phys. Lett.*, vol. 11, pp. 183–185, 1967.

[122] O. D. Jurchescu and T. T. M. Palstra, "Crossover from one- to two-dimensional space-charge-limited conduction in pentacene single crystals," *Appl. Phys. Lett.*, vol. 88, p. 122101, 2006.

[123] C. Hunziker, X. Zhan, P. A. Losio, H. Figi, O. P. Kwon, S. Barlow, P. Günter, and S. R. Marder, "Highly ordered thin films of a bis(dithienothiophene) derivative," *J. Mater. Chem.*, vol. 17, pp. 4972–4979, 2007.

[124] D. Braga, N. Battaglini, A. Yassar, G. Horowitz, M. Campione, A. Sassella, and A. Borghesi, "Bulk electrical properties of rubrene single crystals: Measurements and analysis," *Phys. Rev. B*, vol. 77, p. 115205, 2008.

[125] B. Fraboni, A. Fraleoni-Morgera, and A. Cavallini, "Three-dimensional anisotropic density of states distribution and intrinsic-like mobility in organic single crystals," *Org. Electron.*, vol. 11, pp. 10–15, 2010.

[126] S. Olthof, S. Mehraeen, S. K. Mohapatra, S. Barlow, V. Coropceanu, J.-L. Brédas, S. R. Marder, and A. Kahn, "Ultralow doping in organic semiconductors: Evidence of trap filling," *Phys. Rev. Lett.*, vol. 109, p. 176601, 2012.

[127] C. Tanase, E. J. Meijer, P. W. M. Blom, and D. M. de Leeuw, "Unification of the hole transport in polymeric field-effect transistors and light-emitting diodes," *Phys. Rev. Lett.*, vol. 91, p. 216601, 2003.

[128] C. Tanase, P. W. M. Blom, D. M. de Leeuw, and E. J. Meijer, "Charge carrier density dependence of the hole mobility in poly(p-phenylene vinylene)," *Phys. Status Solidi A-Appl. Mater.*, vol. 201, pp. 1236–1245, 2004.

[129] S. Steudel, S. D. Vusser, S. D. Jonge, D. Janssen, S. Verlaak, J. Genoe, and P. Heremans, "Influence of the dielectric roughness on the performance of pentacene transistors," *Appl. Phys. Lett.*, vol. 85, pp. 4400–4402, 2004.

[130] M. Mottaghi and G. Horowitz, "Field-induced mobility degradation in pentacene thin-film transistors," *Org. Electron.*, vol. 7, pp. 528–536, 2006.

[131] T. Kaji, T. Takenobu, A. F. Morpurgo, and Y. Iwasa, "Organic single-crystal schottky gate transistors," *Adv. Mater.*, vol. 21, pp. 3689–3693, 2009.

[132] D. Braga and G. Horowitz, "High-performance organic field-effect transistors," *Adv. Mater.*, vol. 21, pp. 1473–1486, 2009.

[133] S. A. DiBenedetto, A. Facchetti, M. A. Ratner, and T. J. Marks, "Molecular self-assembled monolayers and multilayers for organic and unconventional inorganic thin-film transistor applications," *Adv. Mater.*, vol. 21, pp. 1407–1433, 2009.

[134] R. A. Street and A. Salleo, "Contact effects in polymer transistors," *Appl. Phys. Lett.*, vol. 81, pp. 2887–2889, 2002.

[135] T. J. Richards and H. Sirringhaus, "Analysis of the contact resistance in staggered, top-gate organic field-effect transistors," *J. Appl. Phys.*, vol. 102, p. 094510, 2007.

[136] I. Kymissis, C. D. Dimitrakopoulos, and S. Purushothaman, "High-performance bottom electrode organic thin-film transistors," *IEEE Trans. Electron Devices*, vol. 48, pp. 1060–1064, 2001.

[137] Y. Xu, T. Minari, K. Tsukagoshi, J. A. Chroboczek, and G. Ghibaudo, "Direct evaluation of low-field mobility and access resistance in pentacene field-effect transistors," *J. Appl. Phys.*, vol. 107, p. 114507, 2010.

[138] K. P. Puntambekar, P. V. Pesavento, and C. D. Frisbie, "Surface potential profiling and contact resistance measurements on operating pentacene thin-film transistors by kelvin probe force microscopy," *Appl. Phys. Lett.*, vol. 83, pp. 5539–5541, 2003.

[139] C. Bock, D. V. Pham, U. Kunze, D. Käfer, G. Witte, and C. Wöll, "Improved morphology and charge carrier injection in pentacene field-effect transistors with thiol-treated electrodes," *J. Appl. Phys.*, vol. 100, p. 114517, 2006.

[140] P. V. Pesavento, R. J. Chesterfield, C. R. Newman, and C. D. Frisbie, "Gated four-probe measurements on pentacene thin-film transistors: Contact resistance as a function of gate voltage and temperature," *J. Appl. Phys.*, vol. 96, pp. 7312–7324, 2004.

[141] L. Bürgi, H. Sirringhaus, and R. H. Friend, "Noncontact potentiometry of polymer field-effect transistors," *Appl. Phys. Lett.*, vol. 80, pp. 2913–2915, 2002.

[142] G. Horowitz, "Tunneling current in polycrystalline organic thin-film transistors," *Adv. Funct. Mater.*, vol. 13, pp. 53–60, 2003.

[143] D. Braga and G. Horowitz, "Subthreshold regime in rubrene single-crystal organic transistors," *Appl. Phys. A-Mater. Sci. Process.*, vol. 95, pp. 193–201, 2009.

[144] G. Fortunato and P. Migliorato, "Model for the above-threshold characteristics and threshold voltage in polycrystalline silicon transistors," *J. Appl. Phys.*, vol. 68, pp. 2463–2467, 1990.

[145] C.-S. Chiang, S. Martin, J. Kanicki, Y. Ugai, T. Yukawa, and S. Takeuchi, "Top-gate staggered amorphous silicon thin-film transistors: Series resistance and nitride thickness effects," *Jpn. J. Appl. Phys.*, vol. 37, pp. 5914–5920, 1998.

[146] S. D. Wang, Y. Yan, and K. Tsukagoshi, "Understanding contact behavior in organic thin film transistors," *Appl. Phys. Lett.*, vol. 97, p. 063307, 2010.

[147] C.-W. Sohn, T.-U. Rim, G.-B. Choi, and Y.-H. Jeong, "Analysis of contact effects in inverted-staggered organic thin-film transistors based on anisotropic conduction," *IEEE Trans. Electron Devices*, vol. 57, pp. 986–994, 2010.

[148] V. Vinciguerra, M. L. Rosa, D. Nicolosi, G. Sicurella, and L. Occhipinti, "Modeling the gate bias dependence of contact resistance in staggered polycrystalline organic thin film transistors," *Org. Electron.*, vol. 10, pp. 1074–1081, 2009.

[149] H. Klauk, G. Schmid, W. Radlik, W. Weber, L. Zhou, C. D. Sheraw, J. A. Nichols, and T. N. Jackson, "Contact resistance in organic thin film transistors," *Solid-State Electron.*, vol. 47, pp. 297–301, 2003.

[150] D. J. Gundlach, L. Zhou, J. A. Nichols, T. N. Jackson, P. V. Necliudov, and M. S. Shur, "An experimental study of contact effects in organic thin film transistors," *J. Appl. Phys.*, vol. 100, p. 024509, 2006.

[151] G. B. Blanchet, C. R. Fincher, M. Lefenfeld, and J. A. Rogers, "Contact resistance in organic thin film transistors," *Appl. Phys. Lett.*, vol. 84, pp. 296–298, 2004.

[152] S. H. Kim, S. H. Lee, and J. Jang, "High-performance n-channel organic thin-film transistor for CMOS circuits using electron-donating self-assembled layer," *IEEE Electron Device Lett.*, vol. 31, pp. 1044–1046, 2010.

[153] C. Goldmann, S. Haas, C. Krellner, K. P. Pernstich, D. J. Gundlach, and B. Batlogg, "Hole mobility in organic single crystals measured by a "flip-crystal" field-effect technique," *J. Appl. Phys.*, vol. 96, pp. 2080–2086, 2004.

[154] S. Luan and G. W. Neudeck, "An experimental study of the source/drain parasitic resistance effects in amorphous silicon thin film transistors," *J. Appl. Phys.*, vol. 72, pp. 766–772, 1992.

[155] J. Zaumseil, K. W. Baldwin, and J. A. Rogers, "Contact resistance in organic transistors that use source and drain electrodes formed by soft contact lamination," *J. Appl. Phys.*, vol. 93, pp. 6117–6124, 2003.

[156] D. Boudinet, G. L. Blevennec, C. Serbutoviez, J.-M. Verilhac, H. Yan, and G. Horowitz, "Contact resistance and threshold voltage extraction in n-channel organic thin film transistors on plastic substrates," *J. Appl. Phys.*, vol. 105, p. 084510, 2009.

[157] G. Horowitz, P. Lang, M. Mottaghi, and H. Aubin, "Extracting parameters from the current–voltage characteristics of organic field-effect transistors," *Adv. Funct. Mater.*, vol. 14, pp. 1069–1074, 2004.

[158] S. Verlaak, V. Arkhipov, and P. Heremans, "Modeling of transport in polycrystalline organic semiconductor films," *Appl. Phys. Lett.*, vol. 82, pp. 745–747, 2003.

[159] A. Bolognesi, M. Berliocchi, M. Manenti, A. D. Carlo, P. Lugli, K. Lmimouni, and C. Dufour, "Effects of grain boundaries, field-dependent mobility, and interface trap states on the electrical characteristics of pentacene TFT," *IEEE Trans. Electron Devices*, vol. 51, pp. 1997–2003, 2004.

[160] W. L. Kalb and B. Batlogg, "Calculating the trap density of states in organic field-effect transistors from experiment: A comparison of different methods," *Phys. Rev. B*, vol. 81, p. 035327, 2010.

[161] J. Takeya, M. Yamagishi, Y. Tominari, R. Hirahara, Y. Nakazawa, T. Nishikawa, T. Kawase, T. Shimoda, and S. Ogawa, "Very high-mobility organic single-crystal transistors with in-crystal conduction channels," *Appl. Phys. Lett.*, vol. 90, p. 102120, 2007.

[162] J. A. Merlo, C. R. Newman, C. P. Gerlach, T. W. Kelley, D. V. Muyres, S. E. Fritz, M. F. Toney, and C. D. Frisbie, "p-channel organic semiconductors based on hybrid acene-thiophene molecules for thin-film transistor applications," *J. Amer. Chem. Soc.*, vol. 127, pp. 3997–4009, 2005.

[163] A. Cerdeira, M. Estrada, R. García, A. Ortiz-Conde, and F. J. García Sánchez, "New procedure for the extraction of basic a-Si:H TFT model parameters in the linear and saturation regions," *Solid-State Electron.*, vol. 45, pp. 1077–1080, 2001.

[164] M. Estrada, A. Cerdeira, A. Ortiz-Conde, F. J. García Sánchez, and B. Iñiguez, "Extraction method for polycrystalline TFT above and below threshold model parameters," *Solid-State Electron.*, vol. 46, pp. 2295–2300, 2002.

[165] A. Cerdeira, M. Estrada, B. Iñiguez, J. Pallares, and L. F. Marsal, "Modeling and parameter extraction procedure for nanocrystalline TFTs," *Solid-State Electron.*, vol. 48, pp. 103–109, 2004.

[166] B. Iñiguez, R. Picos, D. Veksler, A. Koudymov, M. S. Shur, T. Ytterdal, and W. Jackson, "Universal compact model for long- and short-channel thin-film transistors," *Solid-State Electron.*, vol. 52, pp. 400–405, 2008.

[167] O. Marinov, M. J. Deen, U. Zschieschang, and H. Klauk, "Organic thin-film transistors: Part I-compact DC modeling," *IEEE Trans. Electron. Devices*, vol. 56, pp. 2952–2961, 2009.

[168] W. F. Pasveer, J. Cottaar, C. Tanase, R. Coehoorn, P. A. Bobbert, P. W. M. Blom, D. M. de Leeuw, and M. A. J. Michels, "Unified description of charge-carrier mobilities in disordered semiconducting polymers," *Phys. Rev. Lett.*, vol. 94, p. 206601, 2005.

[169] V. O. Turin, A. V. Sedov, G. I. Zebrev, B. Iñiguez, and M. S. Shur, "Intrinsic compact MOSFET model with correct account of positive differential conductance after saturation," in *Proc. SPIE International Conference on Micro- and Nano-Electronics'09*, vol. 7521, 2009, p. 75211H.

[170] M. Estrada, I. Mejía, A. Cerdeira, J. Pallares, L. F. Marsal, and B. Iñiguez, "Mobility model for compact device modeling of OTFTs made with different materials," *Solid-State Electron.*, vol. 52, pp. 787–794, 2008.

[171] M. Estrada, A. Cerdeira, I. Mejia, M. Avila, R. Picos, L. F. Marsal, J. Pallares, and B. Iñiguez, "Modeling the behavior of charge carrier mobility with temperature in thin-film polymeric transistors," *Microelectron. Eng.*, vol. 87, pp. 2565–2570, 2010.

[172] M. Estrada, A. Cerdeira, J. Puigdollers, L. Reséndiz, J. Pallares, L. F. Marsal, C. Voz, and B. Iñiguez, "Accurate modeling and parameter extraction method for organic TFTs," *Solid-State Electron.*, vol. 49, pp. 1009–1016, 2005.

[173] A. Rolland, J. Richard, J. P. Kleider, and D. Mencaraglia, "Electrical properties of amorphous silicon transistors and MIS-devices: Comparative study of top nitride and bottom nitride configurations," *J. Electrochem. Soc.*, vol. 140, pp. 3679–3683, 1993.

[174] D. B. A. Rep, A. F. Morpurgo, and T. M. Klapwijk, "Doping-dependent charge injection into regioregular poly(3-hexylthiophene)," *Org. Electron.*, vol. 4, pp. 201–207, 2005.

[175] S. Scheinert, G. Paasch, M. Schrodner, H. K. Roth, S. Sensfuss, and T. Doll, "Subthreshold characteristics of field effect transistors based on poly(3-dodecylthiophene) and an organic insulator," *J. Appl. Phys.*, vol. 92, pp. 330–337, 2002.

[176] R. Coehoorn, W. F. Pasveer, P. A. Bobbert, and M. A. J. Michels, "Charge-carrier concentration dependence of the hopping mobility in organic materials with Gaussian disorder," *Phys. Rev. B*, vol. 72, p. 155206, 2005.

< Résumé >

En dépit de progrès impressionnants dans les performances des dispositifs électroniques organiques, il n'existe toujours pas de modèle théorique complet pour décrire leur mode opératoire. Cette thèse se propose d'établir une description théorique opérationnelle pour ces dispositifs, avec en ligne de mire leur modélisation physique et compacte. Des exemples typiques de structure de diodes et de transistors organiques avec différentes architectures ont été étudiés, avec une attention constante pour présenter les effets du transport et de l'injection des porteurs de charge sur les caractéristiques observables des dispositifs. Une attention particulière est donnée à l'intégration de ces modèles dans des outils de simulation de circuit, mettant ainsi en relation le dispositif isolé et son intégration dans un circuit. Les différentes approches comprennent la modélisation de circuit par spectroscopie d'impédance, le développement analytique d'équations physiques, la simulation numérique bi-dimensionnelle par éléments finis et leur validation expérimentale. Les résultats apportent une compréhension significative des effets des pièges et de la barrière d'injection sur les caractéristiques courant-tension. Nous proposons des modèles compacts entièrement analytiques pour les diodes redresseuses et les transistors à effet de champ dont la fiabilité numérique et expérimentale est prouvée.

Mots-clés : Electronique organique, physique des dispositifs électroniques, modélisation analytique, diodes, transistors à effet de champ

< Abstract >

Despite impressive progresses in organic electronic devices, a full theoretical understanding of the device operation is still lacking. The thesis is dedicated to establishing applicable theoretical descriptions of organic electronic devices, and in particular physics-based compact models. Prototypical organic diodes and transistors with various architectures are investigated, with a consistent effort to view and present the effect of charge carrier transport and injection on the observable device phenomena. A particular effort is given to integrate these models in circuit simulators, thus connecting the device-level and system-level outlooks. The approaches used comprise equivalent circuit modeling by impedance spectroscopy, analytical development of physics equations, numerical finite-element-based 2-D simulations, and experimental validations. The results provide significant understanding on the effect of traps and injection barriers on the current-voltage characteristics. Original, fully analytical compact models for rectification diodes and organic field-effect transistors are proposed with reliable numerical and experimental proofs.

Keywords : Organic electronics, device physics, analytical modeling, diodes, field-effect transistors